# Laserwire Diagnostics: From Electrons to Negative Hydrogen Ions

Konstantin Olegovich Kruchinin
Royal Holloway, University of London


Thesis submitted in partial fulfilment of the requirements for the degree of Doctor of Philosophy at the Royal Holloway, University of London

July, 2015

# Declaration

I confirm that the work presented in this thesis is my own. Where information has been derived from other sources, I confirm that this has been indicated in the document.

Konstantin Kruchinin

# Abstract

Transverse particle beam diagnostics is crucial for stable and reliable operation of the future accelerators. In some cases, conventional invasive methods for measuring the beam parameters cannot be applied. In these cases, new non-invasive methods are required. The state-of-the art in non-invasive transverse diagnostic is based on laserwire technology where by scanning the focused laser beam across the beam of particles and measuring the flux of the secondary particles produced in laserwire interaction one can determine the particle beam parameters.

This thesis describes the implementation of the laserwire technology in two different cases. The first one is the development of the laserwire beam profile monitor at the Accelerator Test Facility 2 (ATF2) in KEK, Japan for measuring the transverse profiles of very small electron beam which is required for future electron-positron colliders such as Compact Linear Collider and International Linear Collider. Resent results, showing achievement of sub-micrometre resolution are presented. In conjunction to laserwire, a supplementary beam profile monitor based on optical transition radiation was developed and implemented. The recent results of measuring the electron beam profile and emittance are presented.

The second one is the demonstration of low power, fibre coupled laserwire emittance scanner for measuring the transverse phase-space parameters of the high intensity beam of negative hydrogen ions at LINAC4 in CERN, Switzerland. The new LINAC4 will accelerate $H^-$ ions to 160 MeV and ultimately replace the existing 50 MeV LINAC2 in the injector chain for the Large Hadron Collider upgrade. Recent results obtained at 3 MeV commissioning stage are presented.

Finally the thesis discusses the future plans and prospects including improvements of the laserwire system for future electron linear colliders and development of the new combined optical transition/diffraction radiation station at ATF2 for measuring the electron beam emittance and profile with 100 nm resolution. Future plans toward the final design of the laserwire station for 160 MeV $H^-$ beam at LINAC4 and 12 MeV beam at the Front End Test Stand (FETS) in Rutherford Appleton Laboratory are discussed.

# Acknowledgements

First, I would like to express my gratitude and appreciation to my supervisor at RHUL Dr. Pavel Karataev who supported and encouraged me throughout my study and research. I am thankful for his guidance, invaluably constructive criticism and friendly advices during the project work without which this thesis would be impossible.

I would like to extend my gratitude to Dr. Stewart Boogert, Dr. Laurie Nevay and Dr. Alex Aryshev for their invaluable help and support on the early stage of my research. I am sincerely grateful to them for sharing their knowledge and opening up the world of laserwire and OTR beam diagnostics and experimental accelerator physics in general.

I am expressing my gratitude to the laserwire collaboration at RHUL, CERN LINAC4 and FETS: S.M. Gibson, G. Boorman, A. Bosco, T. Hofmann, F. Roncarolo, U. Raich, J. Pozimsky and C. Gabor for their support and assistance.

I would like to thank the ATF2 and LINAC4 staff for their help in machine tuning and for providing us with the opportunity to perform our measurements.

I would like to thank Prof. Junji Urakawa for providing me financial support during my work at the ATF2 in KEK.

I would also like to acknowledge the oPAC scientific network and especially C.P. Welsch for an extensive training program and providing me with the funds necessary for the completion of my research.

At last but not least I want to thank my parents for constant support throughout the period of my study and my friend Ivan Khozyainov for very useful discussions and comments regarding this thesis.

*To my dear wife – Tatiana and daughter – Eva*

# Contents

# List of Figures

# List of Tables

# Acronyms

**ADC** Analogue to digital converter.

**APD** Avalanche photo-diode.

**ATF** Accelerator test facility.

**ATF2** Accelerator test facility 2.

**CAMAC** Computer automated measurement and control.

**CBPM** Cavity beam position monitor.

**CCD** Charge-coupled device.

**CCDTL** Cell coupled drift tube linac.

**CLIC** Compact Linear Collider.

**CVD** Chemical vapor deposition.

**CW** Continuous wave.

**DAQ** Data acquisition system.

**DTL** Drift tube linac.

**EDM** Extensible display manager.

**EPICS** Experimental physics and industrial control system.

**FETS** Front end test stand.

**FWHM** Full width at half maximum.

**ILC** International Linear Collider.

**IP** Interaction point.

**LEBT** Low energy beam transport.

**LMA** Large mode area.

**LWIP** Laserwire interaction point.

**MEBT** Medium energy beam transport.

**MOPA** Master oscillator power amplifier.

**ODR** Optical diffraction radiation.

**ORNL** Oak Ridge National Laboratory.

**OTR** Optical transition radiation.

**PIMS** Pi mode structure.

**PMT** Photomultiplier.

**PSF** Point spread function.

**RFQ** Radio frequency quadrupole.

**RMS** Root mean square.

**SNS** Spallation Neutron Source.

**TTL** Transistor–transistor logic.

# Chapter 1

# Introduction

*Begin at the beginning, the King said gravely, and go on till you come to the end: then stop.*

– Lewis Carroll

PARTICLE accelerators have been used as the major tool for probing the laws of nature since the beginning of the last century. At the beginning, accelerators were used primarily for fundamental research in particle physics. However, with rapid development of technology, accelerators nowadays are used in many industry applications such as non-destructive material testing, ion implantation and isotope production. In medicine accelerators are used for cancer therapy, tomography and as a new sources of X-rays.

Fundamental properties of elementary particles are studied by colliding two high energy beams together in an accelerator. In such machines, two circulating in opposite direction particle beams are accelerated to a high energy and then collide at the interaction point. During the interaction a number of secondary particles can be produced. The sum of the energies of these particles is equal to the double of the energy of the colliding beams. Therefore, by accelerating beams to a higher energies, particles with higher mass can be produced and studied. A good example of such machine is Large Hadron Collider (LHC) [1] - the largest accelerator in the world, built in Geneva, Switzerland which can accelerate proton beams to the nominal energy of about 7 TeV (14 TeV at the collision).

To accelerate particles to a greater energy a higher magnetic field is required to keep particles on a circular orbit of certain radius or the radius of the machine has to be increased for certain magnetic field. Because the strength of magnetic field produced by modern magnets is limited (approximately 15 T for magnets based on superconducting technologies) and increasing the size of the machine will lead to enormous increase in the machine cost, this fact remains the main limitation for achieving very high energies in modern accelerators.

Another limitation factor is related to the fact that the radially accelerating charged particle emits radiation called synchrotron radiation. Synchrotron radiation, for the first time, was predicted by Ivanenko and Pomeranchuk in 1944 [2] and then discovered ex-

perimentally in 1947 [3]. The power of emitted radiation for a single particle is given by the following formula:

$$P = \frac{q^2 c}{6\pi\varepsilon_0 \rho^2} \left(\frac{E}{E_0}\right)^4, \tag{1.1}$$

here $q$ is the charge of a particle, $c$ is the speed of light, $\varepsilon_0$ is the electric constant, $\rho$ is the bending radius, $E$ is the energy of the particle and $E_0$ is the energy of the particle in the rest frame. As one can see, the power of emitted radiation raises very rapidly (as fourth power) with increasing the energy of the accelerating particles. Such dependence leads to the fact that at some point, where the energy transferred to the particle by the accelerator and the energy emitted as synchrotron radiation are equal, further acceleration is impossible. Also, note that the power of the emitted synchrotron radiation inversely proportional to the fourth power of the mass of the particle. This means that this limitation strongly affects only light particles (e.g. electrons or positrons) but less noticeable for heavy particles such as protons and ions. Because of the properties, synchrotron radiation is widely used in many areas of science and industry and circular electron accelerators are used as a light sources.

The latter limitation can be overcome by accelerating electrons and positrons in linear accelerator. In this case, high energy electron-positron linear colliders can be very useful to study some particular processes at high energy (for example production of Higgs boson and studying some properties of Higgs field). As an example, International Linear Collider (ILC) [4] and Compact Linear Collider (CLIC) [5] has been recently proposed as a major tools to study Higgs boson and other new particles associated with it.

The ILC is a 31 km long machine consisting of two linear accelerators (linacs), in which acceleration is accomplished by using niobium superconducting cavities, where each linac accelerates electrons or positrons in opposite directions up to 250 GeV (500 GeV centre of mass energy) with an option to upgrade to 1 TeV.

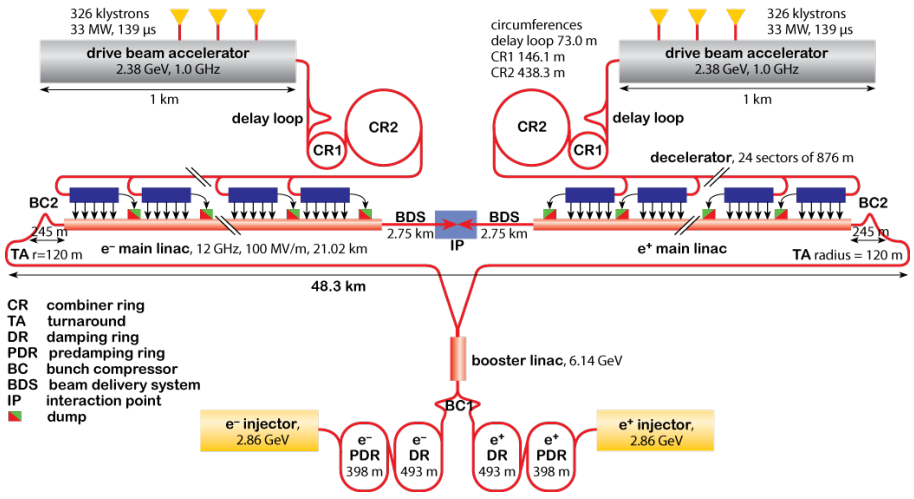


Figure 1.1. Schematic layout of the CLIC accelerator complex (picture from [5]).

CLIC, on the other hand, based on room temperature accelerating structures and aims

to accelerate electrons and positrons to a centre of mass collision energy of 3 TeV. The schematic layout of the CLIC accelerator complex is shown in Fig. 1.1. The main parameters of the CLIC accelerator for 500 GeV and 3 TeV beams are presented in Table 1.1. The main feature of the CLIC acceleration scheme is that the RF field needed for powering the accelerating structures of the linac is generated from a second "Drive Beam". Such scheme allows to generate a very short pulses ($\sim$ 150 ns) of RF field with a very high acceleration gradient (100 MV/m) that can not be generated by currently available power sources (klystrons).

Table 1.1. CLIC main parameters for 500 GeV and 3 TeV (data from [5]).

| **Parameter** | **Symbol** | **500 GeV** | **3 TeV** | **Units** |
|---|---|---|---|---|
| Total luminosity | $\mathfrak{L}$ | 2.3 | 5.9 | $\times 10^{34}$ cm$^{-2}$ s$^{-1}$ |
| Total site length | $L$ | 13 | 48.4 | km |
| Main linac RF frequency | $f_{RF}$ | 12 | 12 | GHz |
| Beam power | $P_{beam}$ | 4.9 | 14 | MW |
| Bunch charge | $Q_{bunch}$ | 6.8 | 3.72 | $\times 10^9$ $e^+/e^-$ |
| Bunch separation | $\Delta f_b$ | 0.5 | 0.5 | ns |
| Bunch length | $\sigma_z$ | 72 | 44 | $\mu$m |
| Beam pulse duration | $t_{beam}$ | 177 | 156 | ns |
| Repetition rate | $f_{rep}$ | 50 | 50 | Hz |
| Horizontal emittance | $\gamma\varepsilon_x$ | 2.4 | 0.66 | $\mu$m |
| Vertical emittance | $\gamma\varepsilon_y$ | 25 | 20 | nm |
| IP horizontal beam size | $\sigma_x$ | 202 | 40 | nm |
| IP vertical beam size | $\sigma_y$ | 2.3 | 1 | nm |

An important property of any general collider is its luminosity:

$$\mathfrak{L} \propto \frac{N_1 N_2}{4\pi\sigma_x\sigma_y} f H. \tag{1.2}$$

Here $N_1$ and $N_2$ are the number of particles in the interacting bunches, $f$ is the bunch frequency, $\sigma_x$ and $\sigma_y$ are the vertical and horizontal transverse beam sizes at the collision point respectively and $H$ is the enhancement factor for the mutual attraction or repulsion between the colliding bunches caused by their charge. Luminosity, multiplied to the cross section of some process, shows how frequent this process will be happening in the collider. As one can see from Eq. 1.2, the luminosity of the collision is greater when the transversal sizes of colliding beams are smaller. It should be noted that the luminosity is higher for the flat beams (beams with high aspect ratio) than for a round beams. Both ILC and CLIC aim to produce an extremely low size (less than a micrometre) beam at the interaction region. In order to control such a small beam, special diagnostic tools are required.

For stable operation of the accelerator the size and other properties of the particle beam have to be precisely determined. The size of the particle beam in the accelerator depends on the properties of the focusing and bending elements of the machine (which can be designed and calculated) and also depends on some internal properties of the beam itself which have to be measured. For some machines where the beam size is very small (micrometre or sub-micrometre) or for machines with high beam currents the task of the beam size measurement can become very challenging. Therefore, development of new methods and techniques for beam size measurements is required for modern accelerators.

## 1.1 Transverse motion of a charged particle in accelerators

Let us consider a charged particle with the charge $q$ and mass $m$ moving around a circular orbit in electromagnetic field described by the electric field vector **E** and magnetic field vector **B**. The motion of such particle is described by the following equation [6]:

$$\frac{\mathrm{d}\mathbf{p}}{\mathrm{d}t} = q\left(\mathbf{E} + \mathbf{v} \times \mathbf{B}\right), \tag{1.3}$$

here $\mathbf{p} = \gamma m \mathbf{v}$ is the relativistic momentum of the particle, $\mathbf{v} = \dfrac{\mathrm{d}\mathbf{r}}{\mathrm{d}t}$ is the velocity and $\gamma = E/mc^2 = 1/\sqrt{1-\beta^2}$ (where $\beta = v/c$ is the relative velocity of the particle) is the relative energy (relativistic Lorentz factor) of the particle. Traditionally, dynamics of the particles in the accelerator is described in circular coordinate system. The diagram of such coordinate system is presented in Fig. 1.2. Position of the particle in this coordinate system is defined by the arc length $s$ measured along the circular orbit of radius $\rho$ from a reference initial point and horizontal $x$ and vertical $z$ displacements from the ideal position.

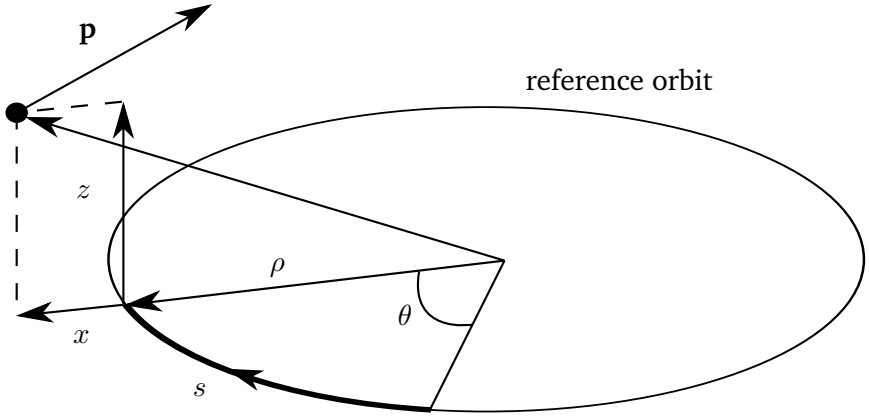


Figure 1.2. Circular coordinate system for particle motion.

Particles in the accelerator are guided and focused by a magnetic field. In this case the electric field **E** in Eq. 1.3 can be neglected. The components of an arbitrary, spatially dependent magnetic field $B$ in transverse plane can be represented as:

$$B(x) = B_0 + \frac{\mathrm{d}B_z}{\mathrm{d}x}x + \frac{1}{2}\frac{\mathrm{d}^2 B_z}{\mathrm{d}x^2}x^2 + \ldots \tag{1.4}$$

Magnetic field of a certain configuration is generated by magnets with a number of pole pairs corresponding to the term number in the expansion Eq. 1.4. The pattern of bending and focusing magnets is repeated around the accelerator and usually referred as lattice of the machine. Dipole magnets producing uniform magnetic field in transverse plane (first term in Eq. 1.4) are used to bend the trajectory of particles and keep them on a circular path. In case of the dipole magnet, Eq. 1.3 can be resolved with the following substitution:

$$\frac{\mathrm{d}p}{\mathrm{d}t} = p\frac{\mathrm{d}\theta}{\mathrm{d}t} = \frac{p}{\rho}\frac{\mathrm{d}s}{\mathrm{d}t}, \tag{1.5}$$

in conjunction with the expression for the magnitude of the Lorentz force in case when the particle moving in the plane perpendicular to the magnetic field:

$$q\left|\mathbf{v}\times\mathbf{B}\right| = qB\frac{\mathrm{d}s}{\mathrm{d}t}. \tag{1.6}$$

The solution can be written in the following form:

$$B\rho = \frac{p}{q}. \tag{1.7}$$

Quantity $B\rho$ is called the magnetic rigidity. As one can see from Eq. 1.7, to accelerate particles to a higher energy higher magnetic field is required to keep particles on the circular path of certain radius $\rho$. The strength of a typical dipole magnet is limited to approximately 1.6 T for room temperature magnets and to approximately 15 T for superconducting magnets. With such constraints, the only way to increase the energy of the particles is to increase the radius of the orbit and, hence, the size of the machine.

In order to focus the beam of particles and prevent them from spreading out quadrupole magnets are used. The quadrupole magnet consists of four poles symmetrically distributed around the center of the magnet bore. Poles of the quadrupole magnet arranged in such a way that the magnetic field is equal to zero at the center of the magnet and linearly rises (in accordance to the second term in Eq. 1.4) with the distance from the center. When a charged particle with an offset from the center of the quadrupole enters the magnet, in one direction, it experiences the restoring force towards the center of the magnet that is proportional to the distance from the center of the magnet. In the other direction, quadrupole magnet acts in opposite way. By arranging pairs of focusing and defocusing quadrupoles throughout the accelerator, the beam of particles can be effectively focused.

Transverse motion of a particle around the circular orbit (sometimes referred as betatron motion) is described by Hill's equations:

$$z'' + k(s)z = 0, \tag{1.8}$$

$$x'' + \left(\frac{1}{\rho^2} - k(s)\right)x = 0. \tag{1.9}$$

Eq. 1.8 describes the motion of particles in the vertical plane and Eq. 1.9 in the horizontal. Periodic coefficient $k(s)$ describes the distribution of focusing strengths around the ring.

The strength of a single quadrupole depends on its gradient $\frac{\mathrm{d}B_z}{\mathrm{d}x}$ and usually presented in the following form:

$$k = \frac{1}{B\rho}\frac{\mathrm{d}B_z}{\mathrm{d}x}. \tag{1.10}$$

If $k$ is positive, the quadrupole is vertically focusing and horizontally defocusing. For negative $k$ the situation is opposite.

The solution of the Hill's equation can be found by assuming that the focusing functions $k(s)$ are periodic ($k(s) = k(s + L)$, where $L$ is the length of the periodic structure in the accelerator) and can be presented in the following way:

$$x = \sqrt{\beta(s)\varepsilon}\cos\left(\phi(s) + \phi_0\right). \tag{1.11}$$

$$x' = \sqrt{\frac{\varepsilon}{\beta(s)}}\left(\frac{\beta'(s)}{2}\cos(\phi(s) + \phi_0) - \sin(\phi(s) + \phi_0)\right) \tag{1.12}$$

Here $\varepsilon$ and $\phi_0$ are constants that can be determined from initial conditions, $\phi(s)$ is the phase advance and $\beta(s)$ is the amplitude function describing the variation of the amplitude with the focusing strength. Note that the amplitude function $\beta$ is the property of the chosen lattice, not the beam of particles.

The solution of the Hill's equation for non periodic lattices can also be found assuming that the magnet strength parameters are constant within each individual magnet ($k(s) = const$). These solutions can be applied to any arbitrary beam transport line where the focusing parameter changes in a step along the beam line. To find the solutions at any point of the lattice, provided that the solution for the preceding element in the lattice is known (for example, periodic solutions in the damping ring can be used as initial conditions for calculation in the transfer line), one can use the following matrix formalism:

$$\begin{pmatrix} x_2 \\ x_2' \end{pmatrix} = \mathbf{M}_{21}\begin{pmatrix} x_1 \\ x_1' \end{pmatrix}, \tag{1.13}$$

here $\mathbf{M}_{21}$ is the $2 \times 2$ matrix (also known as transfer matrix) that in general has the following form:

$$\mathbf{M} = \begin{pmatrix} \cos\psi + \alpha\sin\psi & \sin\psi \\ -\gamma\sin\psi & \cos\psi - \alpha\sin\psi \end{pmatrix}. \tag{1.14}$$

Parameters $\alpha = -\frac{\beta'}{2}$, $\beta$ and $\gamma = \frac{1+\alpha^2}{\beta}$ are called Twiss parameters, $\psi$ is the phase advance per period of the lattice. It should be noted that Twiss parameters $\beta$ and $\gamma$ have no relation to the relative speed and relativistic Lorentz factor defined earlier.

By substituting Eq. 1.11 into Eq. 1.12 and resolving it with respect to $\varepsilon$ one can obtain the following equation:

$$\varepsilon = \gamma x^2 + 2\alpha x x' + \beta x'^2 \tag{1.15}$$

This equation (also known as Courant - Snyder invariant) describes the ellipse in the phase-space ($x$, $x'$) with major and minor axes equal to $\sqrt{\varepsilon\beta}$ and $\sqrt{\varepsilon/\beta}$ respectively. The area of the phase-space enclosed by the ellipse is equal to $\pi\varepsilon$. The quantity $\varepsilon$ is called emittance of the particle beam. According to Liouville's theorem the area within the transverse phase-space ellipse is invariant. This fact defines the importance of the emittance. The relation between phase-space ellipse and Twiss parameters is shown in Fig. 1.3.

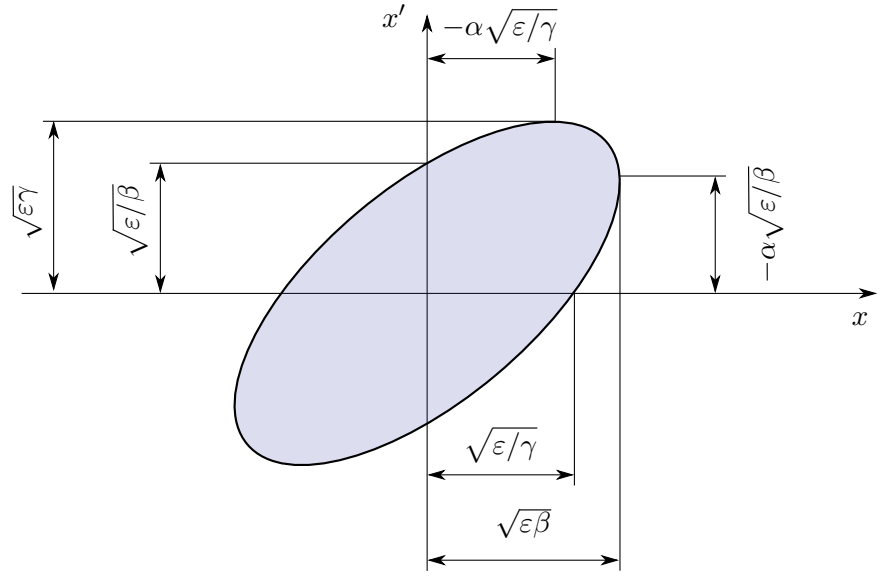


Figure 1.3. The phase-space diagram showing relation between phase-space ellipse and Twiss parameters.

As one can notice, the transverse size of the beam can be defined as $\sigma = \sqrt{\varepsilon\beta}$. Such definition of the beam size is true only for mono-energetic beams or for a dispersion free region. However, in real accelerators, particles always have an energy (momentum) spread $\Delta E/E$ ($\Delta p/p$) that alternates the trajectory of particles when they pass through the elements of the lattice. This phenomena is called the dispersion and contributes to the beam size as following:

$$\sigma = \sqrt{\varepsilon\beta(s) + D(s)^2 \left(\frac{\Delta p}{p}\right)^2}. \tag{1.16}$$

Here $D(s)$ is the dispersion function which depends on the particular beam line lattice and can be calculated.

Derivations presented in this section mostly follow the description given in [7]. Additional and more detailed explanation of the beam dynamics can be found in [8–10].

## 1.2 Overview of techniques for measuring the size and emittance of particle beams

### 1.2.1 Methods of profile measurements

There are a few methods for measurement of the beam size in accelerators. One of the common technique is to place scintillation screen on the way of the beam [11]. When particles interacts with the screen it produces sparks of visible light that can be detected. As a scintillator material, a thin layer of phosphor on a metallic base is commonly used. By placing the screen at an angle to the particle beam, the image of the beam produced in the interaction can then be intensified and transported by the optical system to a detection device (e.g. a CCD camera). The main factor limiting the resolution of such devices is the size of the scintillator grains which is typically around 20 - 30 $\mu$m. Normally, scintilator screens are used for measuring the profile of a very low intensity beams because thin layer of scintillator can become damaged very quickly.

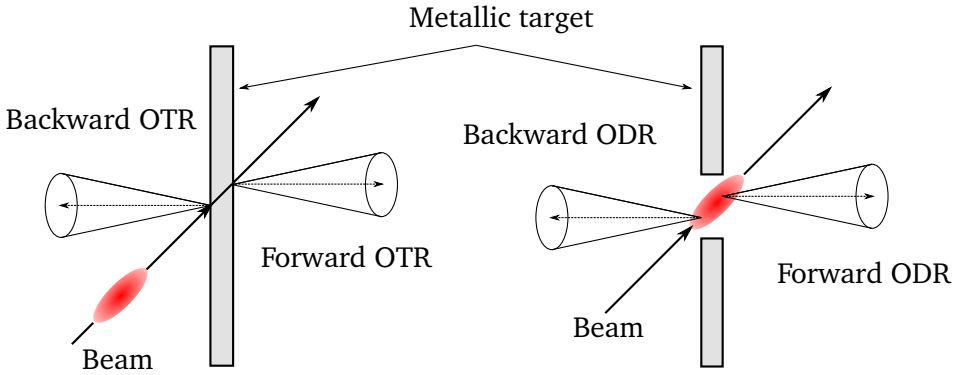


Figure 1.4. Schematic diagram showing the concept of transition radiation (left) and diffraction radiation (right) generation.

Another method is to use a thin metallic wire, usually made of tungsten, to scan across the beam [12]. When particles of the beam interact with the wire a stream of secondary particles and bremsstrahlung is produced. The intensity of the radiation is proportional to the density of the particles in the beam. By placing a detector downstream the wire scanner and measuring the bremsstrahlung flux or flux of secondary particles at each position of the wire, the beam profile can be mapped. Some times, to measure the beam profile in two dimensions, a grid of wires is used. In this case one can measure the electric current induced on each wire by the secondary emission of electrons. The signal in the wire is proportional to the number of particles in the interacting beam. The resolution of wire scanners is defined by the wire diameter which is usually tens of micrometers [13]. A major disadvantage of the wire scanner systems is that the wire can be easily destroyed by the beam. Therefore, wire scanners, like screens, are used to measure the profile of the low intensity beams.

Relatively new technique for measuring the beam profile is based on optical transition

radiation (OTR) [14]. Transition radiation appears when charged particles passes through the target (usually metallic). Schematic of the OTR generation is presented in Fig. 1.4. The light, emitted during the interaction is then captured by the CCD camera and profile of the beam can be retrieved. The resolution of conventional beam profile monitors based on optical transition radiation is limited to a few micrometers, however it can be reduced by using the technique described in section 2.3 of chapter 2 of this thesis.

All the methods described above are invasive. It means that the measuring device directly interacts with the beam of particles. The main disadvantage of these methods is that the beam is destroyed during the measurement and, in some cases, the measuring device itself can be destroyed. Therefore, a new, non-invasive method is required which will be able to measure very small or high intensity beams with high resolution.

There is a possibility to measure transverse beam size using optical diffraction radiation (ODR) [15, 16] which has the same nature as OTR. Diffraction radiation arises when charged particle or bunch of charged particles passes near an optical inhomogeneity, for example an electron moving near a metallic screen or through the slit or aperture in the metallic screen (see Fig. 1.4). Despite the very promising results this technique is still under development.

Nowadays, the state-of-the art in transverse beam diagnostic is based on so-called laserwire technology. By scanning the focused laser beam across the beam of particles and measuring the yield of secondary particles produced in laserwire interaction, the profile of the beam can be deconvolved. The advantage of this method over the conventional ones is that it is almost non-invasive and can be used continuously during the operation of the machine. Only a small portion of the initial beam interacts with the laser while most of the beam passing through without distortion. Another advantage of this method is that the resolution of the system is limited only by the wavelength of the laser beam. The resolution can even be reduced to tens of nanometres by using the method where the beam size is measured by scanning an interference pattern of two lasers across the beam [17]. This method was recognised as a primary diagnostics for future linear colliders [4, 5] and is being developed as a diagnostics monitor for high power $H^-$ drivers for proton accelerators.

### 1.2.2 Methods of emittance measurements

In order to measure the emittance of the particle beam one need to determine its spatial and angular distributions. One of the commonly used techniques is called “pepper-pot” [18]. The concept of this method is the following (see Fig. 1.5): the beam is intercepted by a “pepper-pot” plate which contains a regular array of identical holes with known positions with respect to the center of the beam. The “pepper-pot” plate cuts the incident beam into small portions – beamlets which then propagated to the profile monitor. Measuring the total intensity of each beamlet as a function of the corresponding hole positions one can define the spatial profile of the beam. The angular distribution of the beam at the position of each hole can be obtained by measuring the profiles of corresponding

beamlets.

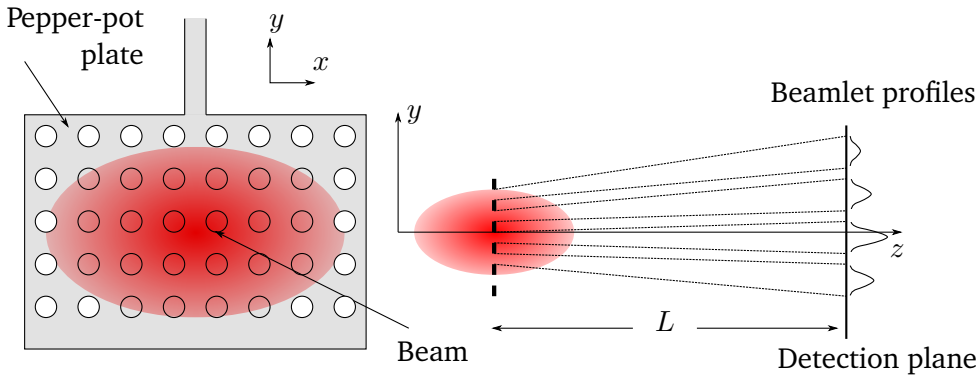


Figure 1.5. Concept of the "pepper-pot" method of the transverse emittance measurement.

The advantage of this method is that the 2D transversal phase-space distribution of the beam can be directly measured and the emittance can be extracted in a single shot. The precision of the method is limited by the holes size and spacing.

Another common method of the emittance measurement is a slit scanner. The basic principle of the slit scanner operation is shown in Fig. 1.6. When the slit is scanned across the beam it selects a narrow portion of the incident beam. The selected beamlet then propagated to the detector where its intensity distribution can be measured. By measuring the intensity distribution of the beamlets at different slit positions one can directly measure the phase-space distribution and, consequently, calculate the emittance of the beam.

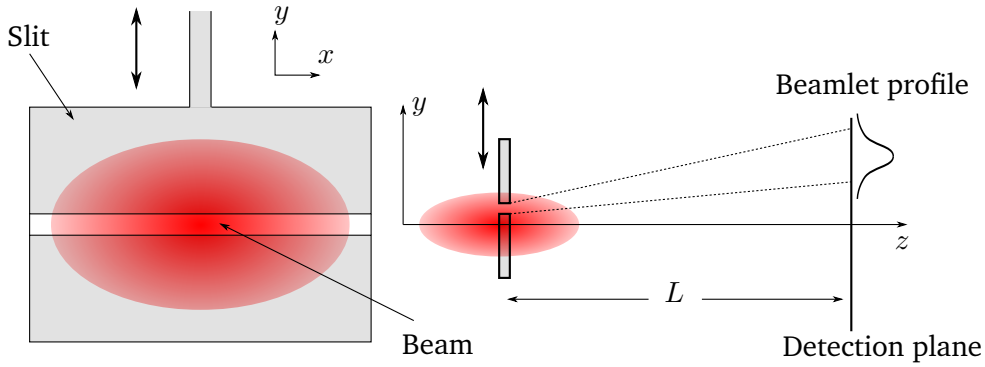


Figure 1.6. Concept of the slit scanner emittance measurement.

In order to calculate both vertical and horizontal transverse emittance two orthogonally positioned slits are usually used. The resolution of the slit scanner is mainly defined by the size of the slit.

The slit scanner and "pepper-pot" methods imply interaction of the beam with the target material. Therefore, to avoid the damage of the target they are usually used to measure the emittance of low intensity beams.

The beam emittance can also be measured from the beam profiles taken under various transport conditions downstream of the given point. This can be achieved by measuring

the beam width at several locations along the beam line separated only by drift spaces. Another way to vary the transfer matrix elements is by varying the strength of a quadrupole magnet located upstream of the interaction point (IP) [19]. The figure 1.7 demonstrates the concept of the emittance measurement using quadrupole magnet.

The beam matrix at the interaction point can be calculated using a standard formula [10]:

$$\Sigma(s_2) = \mathrm{R}\Sigma(s_1)\mathrm{R}^T. \tag{1.17}$$

Here $\Sigma(s_1)$ and $\Sigma(s_2)$ are the beam matrices at the quadrupole and at the interaction point respectively. The total transfer matrix R can be calculated as $\mathrm{R} = \mathrm{R}_L\mathrm{R}_Q$, where

$$\mathrm{R}_Q = \begin{pmatrix} \cos(Kl_q) & \frac{1}{K}\sin(Kl_q) \\ -K\sin(Kl_q) & \cos(Kl_q) \end{pmatrix} \tag{1.18}$$

is the transfer matrix of the focusing quadrupole and $\mathrm{R}_L$ is the transfer matrix between the quadrupole and the interaction point. In the case when it is only a drift space between the quadrupole and IP, the $\mathrm{R}_L$ can be represented as:

$$\mathrm{R}_L = \begin{pmatrix} 1 & L \\ 0 & 1 \end{pmatrix}. \tag{1.19}$$

Here $K$ is the quadrupole strength, $l_q$ is the length of the quadrupole and $L$ is the distance between the quadrupole and IP.

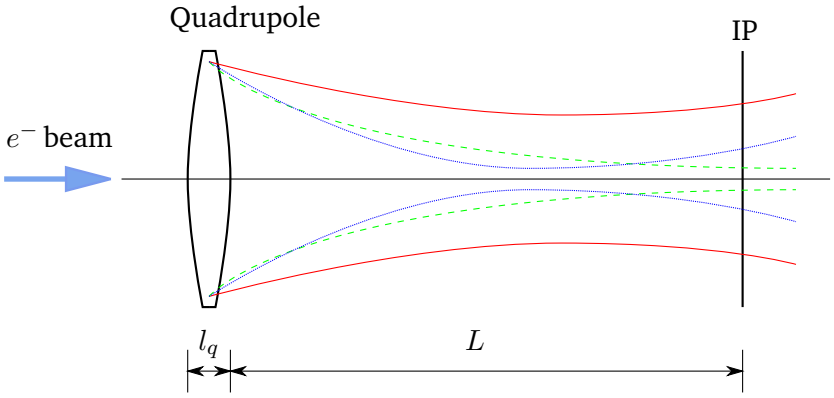


Figure 1.7. Illustration of the concept of the emittance measurement using quadrupole magnet.

To demonstrate the principle, let us assume that the length of the quadrupole is short compared to its focal length (thin lens approximation). In this case total transfer matrix can be simplified to:

$$\mathrm{R} = \begin{pmatrix} 1+KL & L \\ K & 1 \end{pmatrix} \tag{1.20}$$

Expanding the matrix product in Eq. 1.17 taking into account Eq. 1.20 and equating the (1,1) elements on both sides, the square of the vertical or horizontal beam size can be represented as:

$$\Sigma_{11}(s_2) = \sigma_{x,y}^2 = \Sigma_{11}(s_1)L^2K^2 + 2L\left(\Sigma_{11}(s_1) + L\Sigma_{12}(s_1)^2\right)K + \\ + \Sigma_{11}(s_1) + 2L\Sigma_{12}(s_1) + L^2\Sigma_{22}(s_1). \quad (1.21)$$

As one can see the beam size at the interaction point has a quadratic dependence on the field parameter $K$. Thereby, to implement described above technique one need to measure the beam size at the interaction point for different values the quadrupole strength. Then, applying the parabolic fit function:

$$\sigma_{x,y}^2(K) = A(K-B)^2 + C \quad (1.22)$$

to the obtained data, one can reconstruct elements of the beam matrix $\sigma$ by equating coefficients of Eq. 1.22 and Eq. 1.21:

$$\Sigma_{11} = A/L^2 \quad (1.23)$$

$$\Sigma_{12} = -\frac{A}{L^2}\left(B + \frac{1}{L}\right) \quad (1.24)$$

$$\Sigma_{22} = \frac{1}{L^2}\left((AB^2 + C) + 2AB\frac{1}{L} + A\left(\frac{1}{L}\right)^2\right) \quad (1.25)$$

The beam emittance is defined as the square root of the beam matrix and can be calculated from free fit parameters:

$$\varepsilon_{x,y} = \sqrt{\det\Sigma(x,y)} = \sqrt{\Sigma_{11}\Sigma_{22} - \Sigma_{12}^2} = \sqrt{AC}/L^2 \quad (1.26)$$

In the case of a thick lens, the transform matrix is:

$$\mathrm{R} = \begin{pmatrix} m_{11} & m_{12} \\ m_{21} & m_{22} \end{pmatrix} = \begin{pmatrix} \cos(Kl_q) - LK\sin(Kl_q) & \frac{1}{K}\sin(Kl_q) + L\cos(Kl_q) \\ -\cos(Kl_q) - K\sin(Kl_q) & \cos(Kl_q) \end{pmatrix} \quad (1.27)$$

Substituting Eq. 1.27 into Eq. 1.17 and doing analogous calculations as for the thin lens one can get to the following expression:

$$\Sigma_{11}(s_2) = \sigma_{x,y}^2 = \Sigma_{11}(s_1)\left(m_{11}^2 + 2m_{11}m_{12}\frac{\Sigma_{12}(s_1)}{\Sigma_{11}(s_2)} + m_{12}^2\frac{\Sigma_{12}^2(s_1)}{\Sigma_{11}^2(s_2)}\right) + \\ + m_{12}^2\frac{\varepsilon_{x,y}}{\Sigma_{11}(s_2)}. \quad (1.28)$$

Defining new parameters $A \equiv \Sigma_{11}(s_2)$, $B \equiv \dfrac{\Sigma_{12}(s_2)}{\Sigma_{11}(s_2)}$, $C \equiv \dfrac{\varepsilon_{x,y}}{\Sigma_{11}(s_2)}$ and substituting them into Eq. 1.28 leads to the following formula:

$$\sigma_{x,y}^2 = A\left[m_{11}(Kl_q) + Bm_{12}(Kl_q)\right]^2 + Cm_{12}^2(Kl_q). \tag{1.29}$$

As one can see the beam size at the interaction point is a quadratic function of the quadrupole strength. Applying Eq. 1.29 as a fit function to the quadrupole scan one can obtain free fit parameters $A$, $B$ and $C$. The geometric emittance is then calculated using:

$$\varepsilon_{x,y} = \sqrt{AC}. \tag{1.30}$$

## 1.3 Thesis overview

The implementation of the laserwire technique to the measurement of the extremely low emittance transverse electron beam sizes is described in Chapter 2. The first section of the chapter describes the concept of the laserwire for measuring transverse electron beam size. The section 2.2 gives an overview and represents recent results obtained from laserwire experiment at ATF2 in KEK, Japan. Section 2.3 is devoted to description of the sub-micrometre beam size monitor based on OTR used as an auxiliary device to check the laserwire measurements. Main results presented in the chapter are gathered in the section 2.4.

The main topic of the Chapter 3 is the development and implementation of the laserwire technology for measuring the profile and emittance of the beam produced in machines which accelerate negative hydrogen ions. The Chapter begins with the description of the main principles of the laserwire system for $H^-$ ions. Section 3.1 is devoted to the description of the laserwire emittance scanner recently installed and tested at LINAC4 in CERN. The main results of the measurements performed during the winter 2013/2014 operation of the machine at 3 MeV commissioning stage is presented in section 3.1.4.

Chapter 4 describes the future plans for the experiments described in this thesis. Future plans for the micron scale laserwire and sub-micron beam profile measurements using OTR/ODR at the ATF2 is described in sections 4.1 and 4.2 respectively. Section 4.3 emphasizes the key points of the final design for the laserwire emittance meter at LINAC4 in CERN. The chapter ends with the description of the simulation code that has been developed to simulate the laserwire interaction for $H^-$ beams. Results of the simulation for FETS laserwire project obtained with this code are presented in section 4.4. Finally, main results of this thesis are summarized in Chapter 5.

# Chapter 2

# Laserwire for electron machines

*Everything should be made as simple as possible, but not simpler.*

– Albert Einstein

## 2.1 Principles of the laserwire system for electrons

THE idea of the laserwire beam profile measurement is very similar to the concept of a traditional wire scanner. But instead of the metallic wire a high power laser focused in the interaction region down to a micrometre dimensions is used to scan across the electron beam at 90°. During the laser-beam interaction an intense inverse Compton scattered photons are generated. After the interaction, Compton scattered photons propagate along with the electron beam. By measuring the Compton photon yield versus laser position one can directly measure the transverse beam profile.

The number of scattered photons per collision can be calculated using the following formula [20, 21]:

$$N_\gamma = \sigma_C L, \tag{2.1}$$

where $\sigma_C$ is the cross-section of the Compton scattering and $L$ is the luminosity of the laser-electron collision. The luminosity of the collision is given by:

$$L = N_e N_L \int\int\int\int \mathrm{d}x\,\mathrm{d}y\,\mathrm{d}z\,\mathrm{d}t\,\rho_e(x,y,z,t)\rho_L(x,y,z,t). \tag{2.2}$$

Here $N_e$ and $N_L$ are the number of electrons and photons respectively and $\rho_e(x,y,z)$ and $\rho_L(x,y,z)$ are the 3D density distribution functions of the electron bunch and the laser pulse respectively.

Assuming the electron beam with the energy $E_e$ and the laser with wavelength $\lambda_0$ the cross-section of the Compton scattering is given by Klein-Nishina formula [22]:

$$\sigma_C(w) = \sigma_T f(w), \tag{2.3}$$

where $w = \dfrac{\gamma hc}{\lambda_0 m_e c^2}$ is the normalised energy of the laser photons in the electron rest frame and the cross-section of the Thompson scattering, $\sigma_T$, is defined as:

$$\sigma_T = \frac{8\pi}{3}\left(\frac{q^2}{4\pi\varepsilon_0 m_e c^2}\right)^2. \tag{2.4}$$

Here $q$ and $m_e$ are the charge and mass of a particle respectively, $\varepsilon_0$ is the vacuum permittivity. In the case of electron the cross-section of the Thompson scattering is 6.6528 $\times$ $10^{-29}$ m$^2$. The energy and frequency dependent part $f(w)$ in 2.3 is given by:

$$f(w) = \frac{3}{4}\left(\frac{1+w}{w^3}\left(\frac{2w(1+w)}{1+2w} - \log(1+2w)\right) + \frac{\log(1+2w)}{2w} - \frac{1+3w}{(1+2w)^2}\right). \tag{2.5}$$

Figure 2.1 represents the cross-section of the Compton scattering as a function of the electron energy for different wavelengths commonly used in high power lasers. As one can see the Compton cross-section decreases as the energy of the electrons increases.

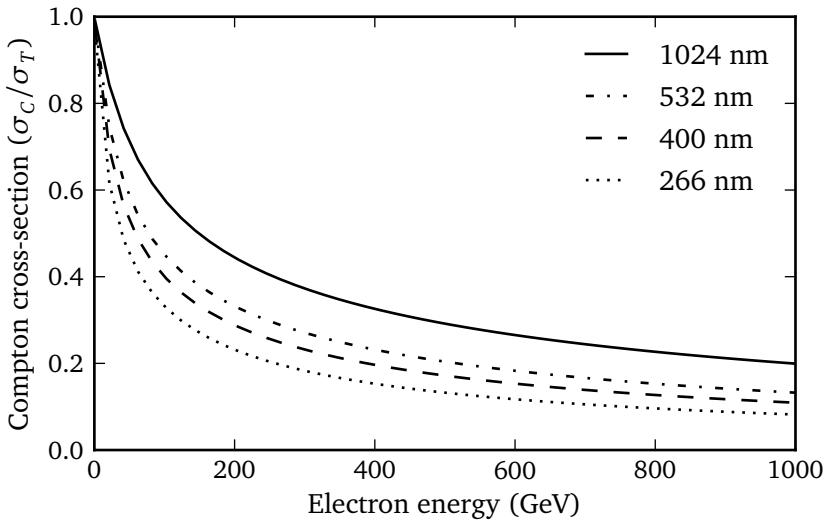


Figure 2.1. The cross-section of the Compton scattering as a function of electron energy for different wavelengths.

The energy spectrum of the scattered photons can be obtained from 2.3 and is given by:

$$\frac{1}{\sigma_T}\frac{\partial\sigma_C}{\partial\xi} = \frac{3}{8w}\left(\frac{1}{1-\xi} + 1 - \xi + \left(\frac{\xi}{w(1-\xi)}\right)^2 - \frac{2\xi}{w(1-\xi)}\right). \tag{2.6}$$

Here $\xi = \dfrac{E_\gamma}{E_e} = \dfrac{h\nu}{E_e}$ is the normalized energy of the scattered photons. The maximum photon energy can be derived from 2.6 and is given by:

$$E_\gamma^{max} = E_e\left(\frac{2w}{1+2w}\right). \tag{2.7}$$

Figure 2.2 shows the spectrum of the Compton scattered photons for different laser wavelengths. The spectrum is broad with the sharp maximum at the maximum energy of the scattered photons. For a moderate electron energies (about 1 GeV) the energy of the scattered photons is a small fraction of the incoming electron energy. Because incoming electrons experience only a small degradation in their energy they will continue to be transported and inverse-scattered photons can be detected.

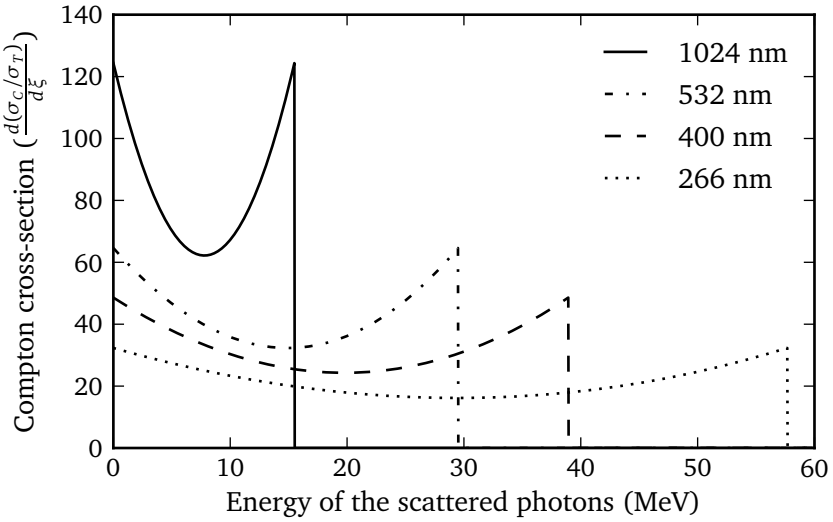


Figure 2.2. Spectrum of the Compton scattered photons from a 1.3 GeV electron beam.

The laserwire scan consists of the measurement of the Compton-scattered photon rate for different laser transverse positions. Therefore, it can be represented as the convolution of the transverse density function of the laser and electron beams along the axis of scan. The schematic of the laserwire interaction is shown in Fig. 2.3. Assuming that the laser and the electron beams have 3D Gaussian density functions, the convolution also has a Gaussian form. However, it should be taken into account that the transverse laser beam size is not constant along the axis of propagation. The length scale of this is described by the Rayleigh range which is the distance along the propagation direction from the laser focus to the place where the transverse area of the laser beam is doubled [23]. If the Rayleigh range is much bigger than the electron beam size the laser beam size can be assumed to be constant across the electron beam (like a wire in conventional wire scanner) and the electron beam profile can be easily deconvolved from the scan independently of the horizontal size of the electron beam. In the case when the Rayleigh range is comparable to or shorter than the electron beam size the divergent tails of the laser beam interact with the electron beam even when the laser significantly displaced transversely from the center of the electron beam. In this case to deconvolve the electron beam size from the scan the time-varying laserwire profile must be taken into account.

To derive the form of the scan one can use the Eq. 2.1. Because the cross-section of the Compton scattering is constant for given geometry of the collision, electron beam energy and laser wavelength, the rate of the scattered photons $N_\gamma$ is defined only by the

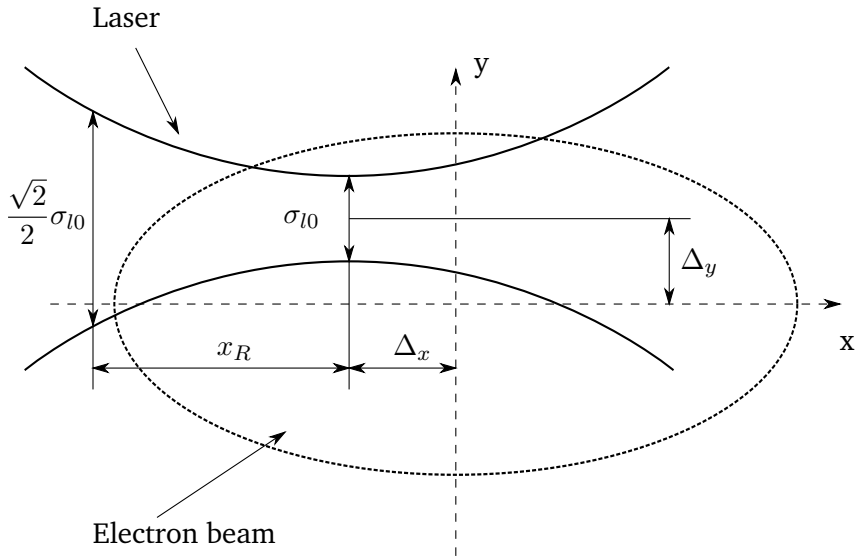


Figure 2.3. Schematic of the laserwire interaction with the key dimensions.

luminosity of the laserwire interaction (Eq. 2.2). The luminosity of the collision can be represented as the function of $\Delta_x$ and $\Delta_y$, the horizontal and vertical displacement of the laser focus from the center of the electron beam. Let us assume that the laser pulse length is much longer than the electron bunch length (so the laser distribution can be treated as a static target) and that both laser and electron beams have Gaussian density functions:

$$\rho_L(x,y,z) = \frac{1}{2\pi}\frac{1}{\sigma_{Ly}(x-\Delta_x)\,\sigma_{Lz}(x-\Delta_x)}\times \\ \times \exp\left(-\frac{(y-\Delta_y)^2}{2\sigma_{Ly}^2(x-\Delta_x)} - \frac{z^2}{2\sigma_{Lz}^2(x-\Delta_x)}\right), \quad (2.8)$$

$$\rho_e(x,y,z,t) = \frac{1}{(2\pi)^{3/2}}\frac{1}{\sigma_{ex}\sigma_{ey}\sigma_{ez}}\exp\left(-\frac{x^2}{2\sigma_{ex}^2} - \frac{y^2}{2\sigma_{ey}^2} - \frac{(z-\beta ct)^2}{2\sigma_{ez}^2}\right). \quad (2.9)$$

Here $\sigma_{Ly}(x-\Delta_x)$ and $\sigma_{Lz}(x-\Delta_x)$ are the vertical and horizontal laser beam sizes. By substituting Eq. 2.8 and Eq. 2.9 into the overlap integral Eq. 2.2 one can perform integration over three of the dimensions resulting in the following formula:

$$N_\gamma(\Delta_x,\Delta_y) = \frac{P_l N_e \lambda \sigma_C}{\beta hc^2}\frac{1}{2\pi\sigma_{ex}}\int_{-\infty}^{\infty}\frac{1}{\sqrt{\sigma_{ey}^2+\sigma_{Ly}(x-\Delta_x)^2}}\times \\ \times \exp\left(-\frac{x^2}{2\sigma_{ex}^2} - \frac{\Delta_y^2}{2\left(\sigma_{ey}^2+\sigma_{Ly}(x-\Delta_x)^2\right)}\right)\mathrm{d}x. \quad (2.10)$$

Here $P_l$ is the peak laser power, $\sigma_{ex}$ and $\sigma_{ey}$ are the horizontal and vertical electron beam sizes respectively. The propagation of a focused multimode laser beam is given by:

$$\sigma_{Ly}\left(x-\Delta_x\right)=\sigma_{l0}\sqrt{1+\left(\frac{x-\Delta_x}{x_R}\right)^2}, \tag{2.11}$$

where $\sigma_{l0}$ is the size of the laser at its focus. The Rayleigh range $x_R$ can be defined as:

$$x_R=\frac{4\pi\sigma_{l0}^2}{\lambda M^2}. \tag{2.12}$$

Here $M^2$ is a beam quality factor describing the spatial quality of the actual laser beam with respect to the ideal Gaussian beam at the same wavelength and can be measured [24].

In the case when $x_R \gg \sigma_{ex}$ and the laser focus is aligned to the electron beam center ($\Delta_x = 0$) Eq. 2.10 can be simplified to:

$$N_\gamma(\Delta_y)=\frac{P_l N_e \lambda \sigma_C}{\beta h c^2}\frac{1}{(2\pi)^{3/2}\sqrt{\sigma_{ey}^2+\sigma_{Ly}^2}}\exp\left(-\frac{\Delta_y^2}{2\left(\sigma_{ey}^2+\sigma_{Ly}^2\right)}\right) \tag{2.13}$$

As one can see, Eq. 2.13 has the form of Gaussian. In this case the electron beam size $\sigma_{ey}$ can be deconvolved from the vertical laserwire scan with knowing only the $\sigma_{l0}$ independently of the horizontal beam size $\sigma_{ex}$. In the case when $x_R \leq \sigma_{ex}$ Eq. 2.10 must be used with the measured longitudinal laser profile and horizontal electron beam size $\sigma_{ex}$.

## 2.2 Laserwire beam profile monitor at ATF2

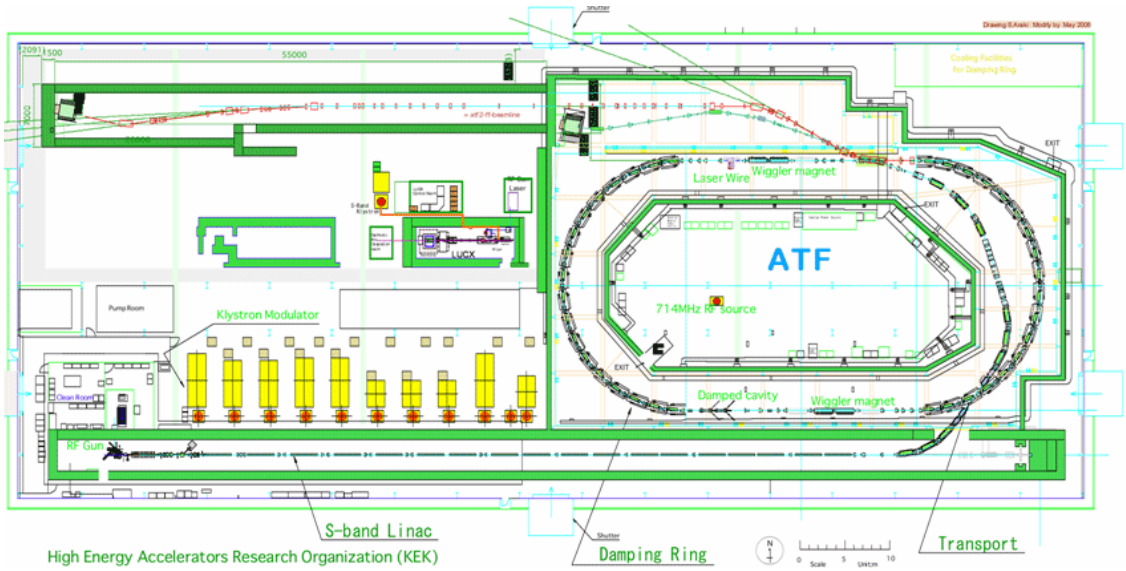


Figure 2.4. Schematic layout of the ATF2 (picture from [28]).

In order to demonstrate a micrometre beam size a laserwire system has been developed at the Accelerator Test Facility 2 at the Japanese National High Energy Physics Research

Organisation (KEK) in Tsukuba, Japan. In 2008 the ATF was upgraded by extending the extraction line in order to create the prototype final focus system required for future linear colliders. The aim of the ATF2 is to demonstrate the focused vertical beam size of $\sim$ 37 nm [25]. The minimum vertical beam size of $\sim$ 65 nm has been demonstrated during beam operations in 2012 and 2013 [26].

The ATF2 consists of 1.3 GeV S-band linac followed by damping ring where the electron beam emittance is cooled by synchrotron radiation [27]. After remaining in the damping ring the beam is extracted into the extraction line where it can be diagnosed and transported to the final focus. Schematic layout of the entire machine is presented in Fig. 2.4. A summary of the electron beam parameters is given in Table 2.1.

Table 2.1. ATF2 parameters.

| **Parameter** | **Symbol** | **Value** | **Units** |
|---|---|---|---|
| Beam energy | $E$ | 1.3 | GeV |
| Horizontal emittance | $\gamma\varepsilon_x$ | $4\times10^{-6}$ | m rad |
| Vertical emittance | $\gamma\varepsilon_y$ | $4\times10^{-8}$ | m rad |
| Bunch repetition rate | $f_{bunch}$ | 3.12 | Hz |
| Bunch length | $\sigma_{ez}$ | $\sim$ 30 | ps |
| Electrons per bunch | $N_e$ | 0.5-1.0$\times10^{9}$ | $e^-$ |
| Fractional momentum spread | $\Delta p/p$ | 0.001 | – |

The first laserwire system at the ATF was commissioned in 2010 and demonstrated the smallest electron beam size of 4.8$\pm$0.3 $\mu$m [29]. In Summer 2011 the laserwire station was relocated [30, 31] to the beginning of the ATF2 final focus section where strong, closely spaced matching quadrupoles allow a vertical electron beam size $<$ 1 $\mu$m to be achieved.

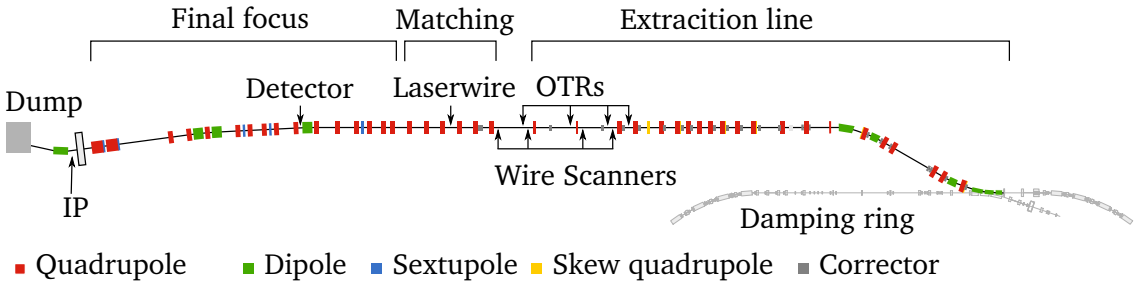


Figure 2.5. Schematic of the ATF2 extraction line showing the location of the laserwire system as well as the detector located immediately after the first dipole magnet after the LWIP.

The extraction line of the ATF2 contains various diagnostic tools to control and measure the electron beam. Aside from micron-scale laserwire it includes multi OTR screens,

wire scanners and high resolution OTR beam profile monitor for measuring the transverse profile and emittance of the electron beam. Schematic of the matching section showing the location of the laserwire station and the detector is shown in Fig. 2.5.

### 2.2.1 Electron beam optics

During laserwire operations, especially developed electron beam optics was used to minimize the vertical beam size at the LWIP. Figure 2.6 represents both sets of electron beam optics for the extraction line, matching section and beginning of the final focus. With the normal ATF2 settings the vertical waist exists $\sim$ 20 cm downstream from the LWIP at the location of the MFB2FF cavity beam position monitor (CBPM) [32]. The laserwire optics were designed to shift the waist to the LWIP and reduce vertical beam size even further. With the normal ATF2 optics, the horizontal amplitude function $\beta_x$ expands in the final focus section to $\beta_x > 40$ km (see Fig. 2.6), which intentionally collimates the beam using the beam pipe. As a result, this produces a large background for the laserwire detector, so for laserwire operations $\beta_x$ was significantly reduced. As expected, reducing $\beta_x$ increases $\beta_y$, but this does not generate comparable background levels as the vertical emittance much lower than the horizontal one. Amplitude functions $\beta_x$ and $\beta_y$ around the laserwire location, where the shifted vertical waist is clear, are shown in Fig. 2.7.

Using laserwire beam optics at the LWIP with $\beta_x = 8.822$ m and $\beta_y = 15.625$ mm, which combined with the nominal emittance values, gives a predicted electron beam size of 0.495 $\mu$m in vertical and 117 $\mu$m in horizontal direction. Additionally, apart from amplitude functions $\beta_{x,y}$, the electron beam size $\sigma_e$ also depends on the dispersion at the LWIP. This dependence usually represents by Eq. 1.16. Nominal horizontal and vertical

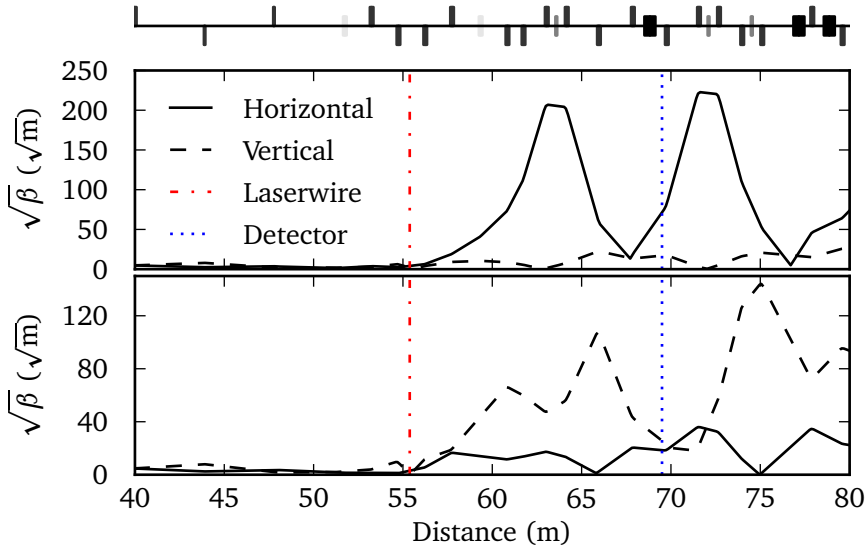


Figure 2.6. Electron beam amplitude functions at the end of the extraction line, matching section and beginning of the final focus for normal ATF2 operation (top) and for laserwire operation (bottom).

dispersion at the LWIP are supposed to be zero, however there is possible a finite amount due to residual dispersion from beam misalignment in the extraction line quadrupoles or residual $x$ - $y$ coupling. Dispersion and coupling are measured and corrected using the Flight Simulator software [33], which measures the electron beam trajectory using the high resolution CBPM system as a function of electron beam energy. The energy is modulated by adjusting the damping ring RF frequency, and the calculated coupling and dispersion is corrected using four upstream skew quadrupoles in combination.

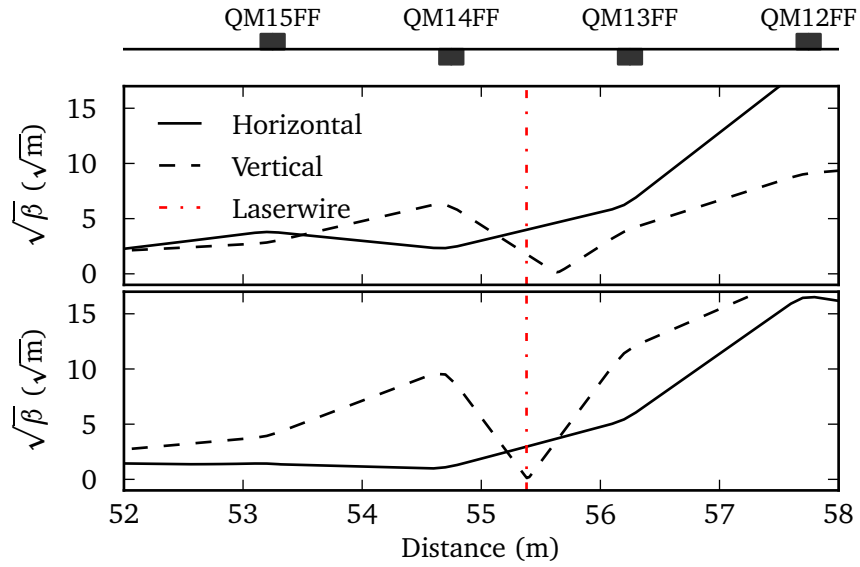


Figure 2.7. Electron beam amplitude functions about the laserwire interaction point for normal ATF2 operation (top) and for laserwire operation (bottom). QM12FF – QM15FF are the quadrupoles around LWIP.

### 2.2.2 Experimental setup

The experimental setup consists of a high power laser system mounted on the optical table which is located in the interlocked laser laboratory above the accelerator enclosure, so the laser can be operated in radiation safe and temperature controlled environment. The laser beam is transported to the accelerator environment in free space through the 10 cm hole in both the table and concrete shielding blocks using periscope of mirrors. The mirrors are mounted in two optical tables beside the beam line which contain all necessary optics to perform alignment of the laser beam and deliver it to the interaction point.

After the laser is transported to the interaction point it is directed into a custom made vacuum chamber with high damage threshold vacuum window on either side to allow the laser beam enter and exit. The vacuum chamber can be moved $\pm 3$ mm in both horizontal and vertical axes. To focus the laser beam a laserwire lens is mounted on to especially designed kinematic lens mount which provides precise control of the lens separation from the vacuum window as well as its angle. The laserwire lens with a focal length $f$ = 56.6 mm consists of two radiation hard fuse silica elements that are designed to correct geometric aberrations. The laserwire scan is performed by moving the vacuum chamber

with the attached lens and therefore the laser focus across the electron beam in vertical or horizontal direction. Optical position encoders provide 50 nm accuracy on the chamber position measurements. The coordinate axes of the interaction point are presented in Fig. 2.8.

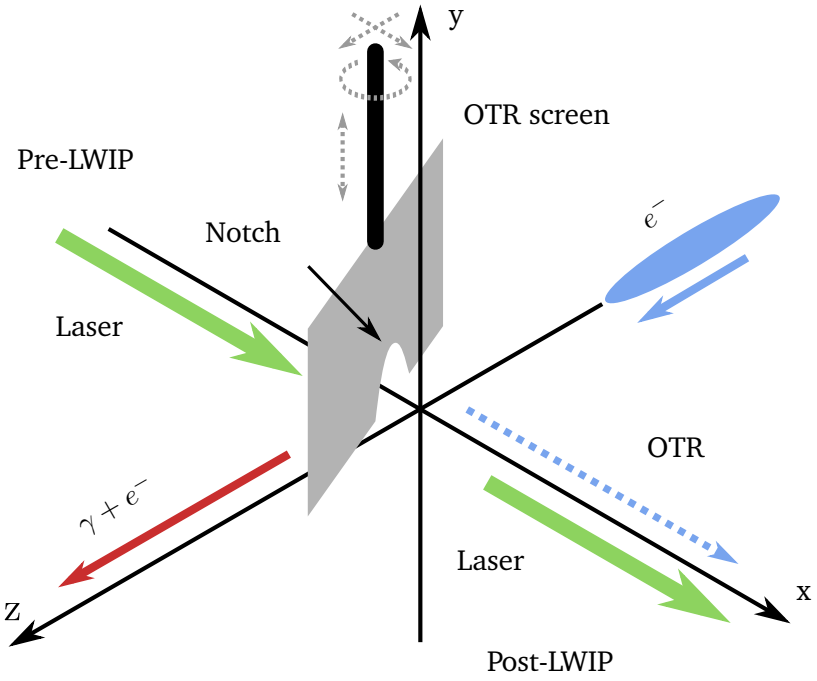


Figure 2.8. Schematic of the beam geometry at the laserwire interaction point.

The schematic and the photograph of the laserwire interaction region are shown in Fig. 2.9 and Fig. 2.10 respectively. A metal screen for OTR sub-micrometer beam size monitor (see Section 2.3) and laserwire alignment is mounted on a 4D vacuum manipulator that access the vacuum chamber from the top. The position of the screen in $x$ and $z$ direction can be adjusted by manual micrometers. The angle of the OTR screen with respect to the electron beam direction and its vertical position in $y$ axis is controlled by motorized actuators.

After the interaction point (Post-LWIP) the laser beam exits the vacuum chamber through the vacuum window and is propagated to the energy meter by two mirrors. A plano-convex lens is used to re-collimate the laser beam and brings it inside to the active area of the energy meter. A small amount of laser light transmitted through the first mirror is detected by an avalanche photodide (APD). The APD collects both the OTR and the laser light and is used for the temporal alignment of the laser and electron beams. The alignment procedure will be explained in details in section 2.2.4. Because laserwire and OTR experiments share the same vacuum chamber and to avoid the damaging of the OTR optics by gigawatt laser pulses two separate switchable optical paths are used. Mirrors for each optical path are mounted on a small optical breadboard placed on top of the translation stage which allows to switch the optics for different experiments during the operation.

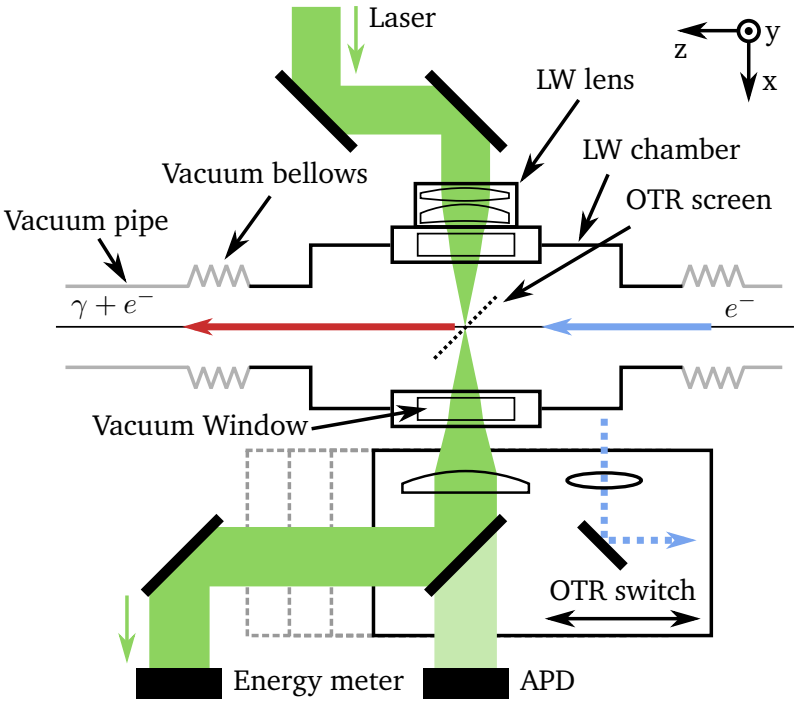


Figure 2.9. Schematic of the laserwire interaction point in plain view.

After collision, high energy, Compton scattered photons propagate along the direction of the electron beam. To detect these photons the laserwire detector is placed approximately 10 m downstream immediately after the BH5X dipole magnet in the ATF2 lattice, which is the first bend after the LWIP. The box-shaped vacuum pipe inside the dipole has an aluminium window 26 mm in diameter and 200 $\mu$m in thickness at the end. That window allows to withdraw the beam of Compton scattered photons and then detect it by the laserwire detector.

The detector consists of a $40 \times 40 \times 6$ mm$^3$ lead plate followed by $40 \times 40 \times 50$ mm$^3$ block of SP-15 Aerogel (density 60 kgm$^{-3}$ and refractive index 1.015). The lead plate acts as a converter: when high energy Compton scattered photons from the LWIP passing through the lead it generates a high momentum electron-positron pairs. The Aerogel acts as a radiator for the electron-positron pairs generating Cherenkov radiation as they pass through. The Cherenkov light is guided in a light tight pipe, internally coated with aluminumized mylar, to a shielded "Hamamatsu" R877 photomultiplier (PMT) tube [34] out of the accelerator plane. The voltage generated by the PMT is then digitized using 14 bit analogue to digital converter (ADC) which is integrated into the CAMAC crate, so the signal from the detector can be accessed from the main data acquisition system (DAQ).

The detector can also catch the synchrotron radiation background coming from the dipole located upstream. However, it is negligible because the synchrotron radiation energy at the peak of its spectrum is $\sim$ 0.3 keV, which is not enough to produce electron-positron pairs in the lead plate.

To record data and control different parts of the experimental setup, data acquisition system based on Experimental Physics and Industrial Control System (EPICS) database

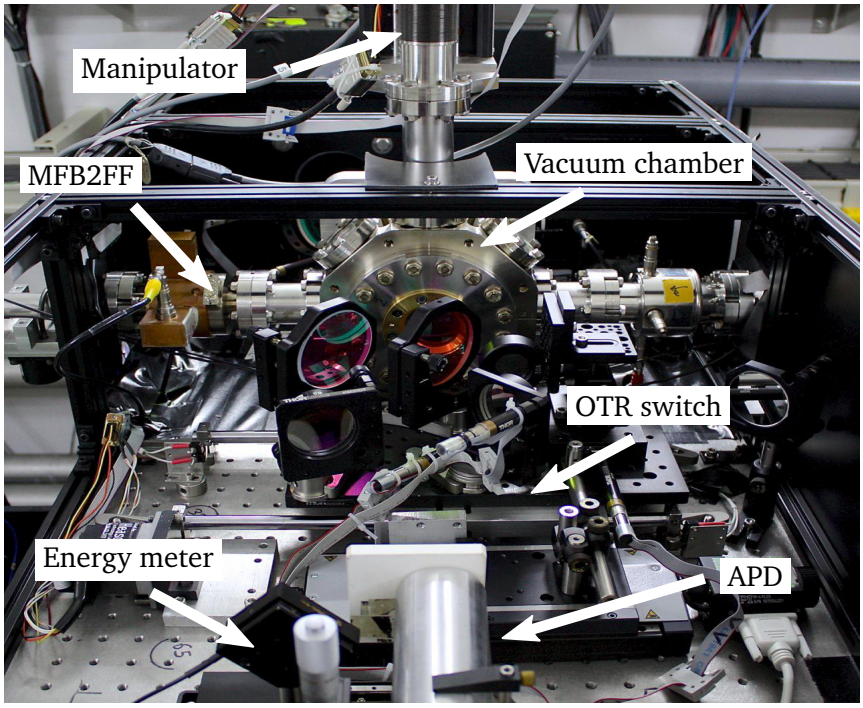


Figure 2.10. Photograph of the laserwire setup in the ATF2 beam line.

software [35] has been developed. EPICS provides an easily extendable common interface for all devices involved in the experiment as well as graphical user interface using Extensible Display Manager (EDM). To control, store and analyse experimental data a Python [36, 37] based software were used. Individual devices were controlled through LabView [38] or C software directly, which monitor command variables in the EPICS database and publish data and measurements to other variables. Data were recorded from all devices for each machine cycle at 3.12 Hz as well as data from other ATF2 instrumentation.

### 2.2.3 Laser system

The laser system consists of a seeded, Q-switched neodymium-doped yttrium aluminium garnet (Nd:YAG) amplifier that provides laser pulses with a duration of $\sigma_\tau = 70.8 \pm 0.6$ ps at 3.12 Hz, the repetition rate of the ATF2. The output energy of the laser is $\sim 150$ mJ with a wavelength of 532 nm. The schematic of the laser system is shown in Fig. 2.11.

The seed laser is 357 MHz mode locked Time-Bandwidth Neodymium-Doped Vanadate (Nd:VAN) oscillator that generates pulses with maximum output energy of 500 mJ and wavelength of 1064 nm. One of the oscillator's mirror is equipped with a piezo actuator (temporal jitter $< 2$ ps), so the laser oscillator can be stabilized and locked to an external signal generator. The signal generator is manually adjusted to match the ATF2 master oscillator frequency at the start of each operation period, because the ATF2 frequency is varied slightly according to the annual expansion cycle of the damping ring. To provide a stable phase relationship between the electron bunches and the laser a 10 MHz reference

signal is relayed between the ATF2 master oscillator and the laserwire signal generator.

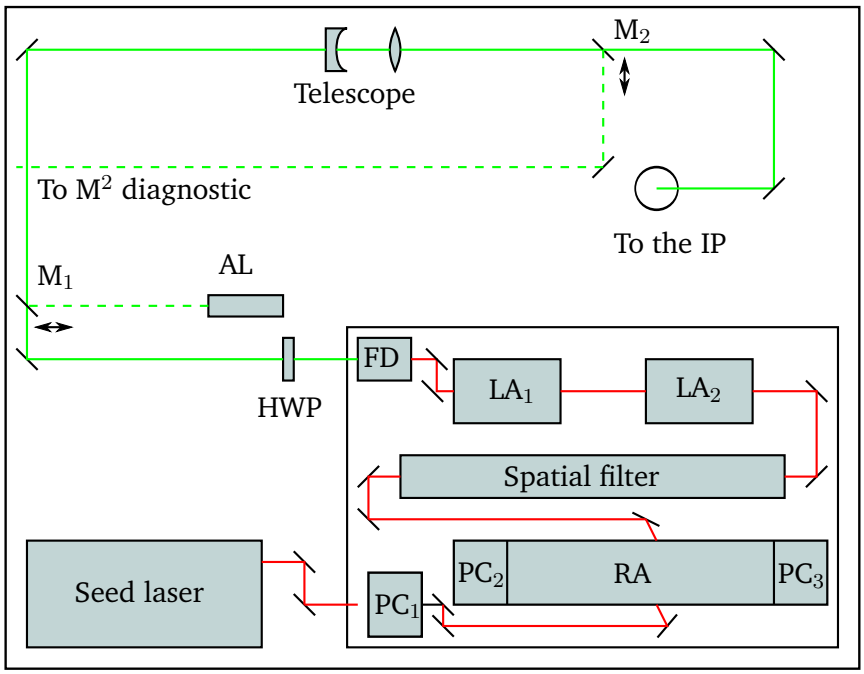


Figure 2.11. Schematic of the main components of the laser system. $PC_1$, $PC_2$ and $PC_3$ is the first, second and third EOMs, RA is the regenerative amplifier, $LA_1$ and $LA_2$ is the linear amplifiers, FD is the frequency doubling crystal, HWP is the half-wave plate and AL is the alignment laser.

After the seed laser the beam is directed to the main laser system. Two electro-optic modulators (EOM) are used to isolate a single laser pulse from the oscillator which is then amplified in a regenerative amplifier where the laser pulse is passing through the laser gain medium many times reaching high level of amplification. A third EOM is used to extract the laser pulse from the regenerative amplifier when it is reached the maximum possible energy. After regenerative amplifier the laser pulse passes through the spatial filter and then transported to two single-pass linear amplifiers that contain flash-lamp pumped Nd:YAG laser gain media which provides additional level of amplification. The trigger for the flash lamps in the linear amplifiers and trigger for the regenerative amplifier can be controlled manually and independently. By changing the delay of the flash lamp in the linear amplifier one can vary the output energy of the laser system (for example, increasing the delay, so the flash lamp fires later, the laser pulse experienced the lower gain).

After linear amplifiers the laser pulse passes through a non-linear potassium titanyl phosphate crystal that doubles the frequency, hence halves the minimum achievable focused spot size of the laser beam [39].

Various “CVI” mirrors [40] with 3 inch diameter coated for a high reflectivity ($>$ 99.6 %) at 532 nm, as well as a high damage threshold are used to guide the laser beam after the main laser system into the accelerator environment. In order to achieve a higher

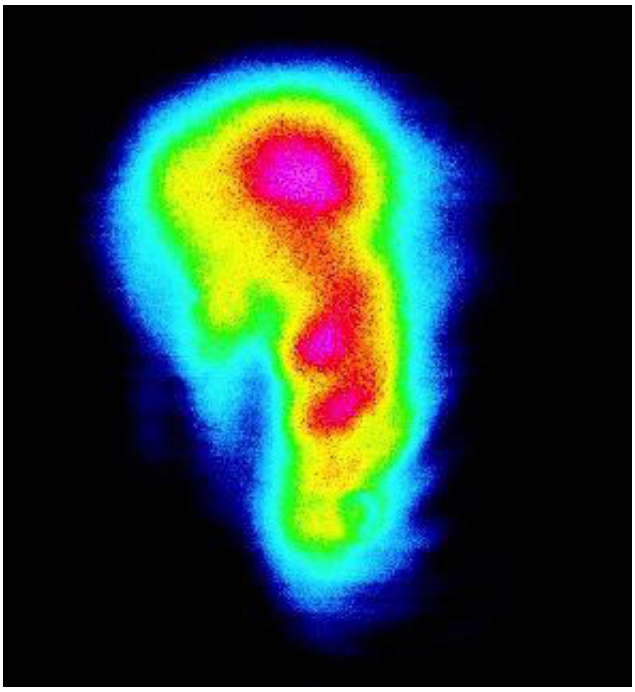

Figure 2.12. Input laser profile measured at the end of the laser diagnostic line.

reflectivity from each mirror the output linear polarization of the laser beam is rotated using a half-wave plate inserted at the exit port of the main laser system. To adjust the input laser beam size a demagnifying Galilean telescope consisting of a plano-concave lens followed by plano-convex lens is used. The telescope is placed after the main laser system far from the IP so the telescope could be used to manipulate the input beam size without strongly affecting the laser divergence and therefore the $x$ location of the focus at the LWIP. One of the lens of the telescope is placed on the linear translation actuator so the divergence and therefore the input laser beam size at the laserwire lens can be precisely controlled by adjusting the spacing of the lenses.

Two insertion mirrors ($M_1$ and $M_2$ in Fig. 2.11) mounted on linear translation stages are used either to insert a low power alignment laser into the main laser beam path or redirect the main laser beam to a diagnostic line. The diagnostic line consists of a series of semi-transparent mirrors that provide exactly the same optical path length as to the laserwire lens beside the LWIP ($\sim$ 8.4 m).

**Laser characterisation**

In order to deconvolve the laserwire scans, precise knowledge of the laser beam quality is required. This can be done by measuring the $M^2$ parameter of the laser and the input laser beam profile at the laserwire lens. Because the laser profile is affected by different optical components of the laser system, the slight adjustment in alignment is often necessary to maintain the required laser output power. Therefore, the reproducibility of the $M^2$ measurement is important. To measure the $M^2$ and the profile of the laser beam the diagnostic line was used in the laser hut without requiring an access to the acceler-

ator tunnel. To record the intensity profile of the laser a "WinCamD" CCD camera [41] was placed at the end of the diagnostic line. A lens with focal length of $f = 1.677$ m (at 532 nm) was used to create a variation of the laser spot sizes along the laser beam. Various reflective beam splitters were used to reduce the intensity of the laser to within the dynamic range of the CCD. The CCD camera was mounted on a linear translation stage so the laser beam profiles can be recorded at different positions along the direction of the laser beam propagation. Laser intensity profiles at various positions throughout the focus were recorded using "DataRay" software provided with the CCD camera. An example of the input laser beam profile is shown in Fig. 2.12. It is obvious that the laser beam profile is not Gaussian. To extract the $M^2$, measured laser beam sizes as a function of the camera position were fitted to the $M^2$ model (Eq. 2.11 with $\Delta_x = 0$). The $4\sigma$ width along the intrinsic laser beam axes as a function of CCD position along with the $M^2$ fit are shown in Fig. 2.13.

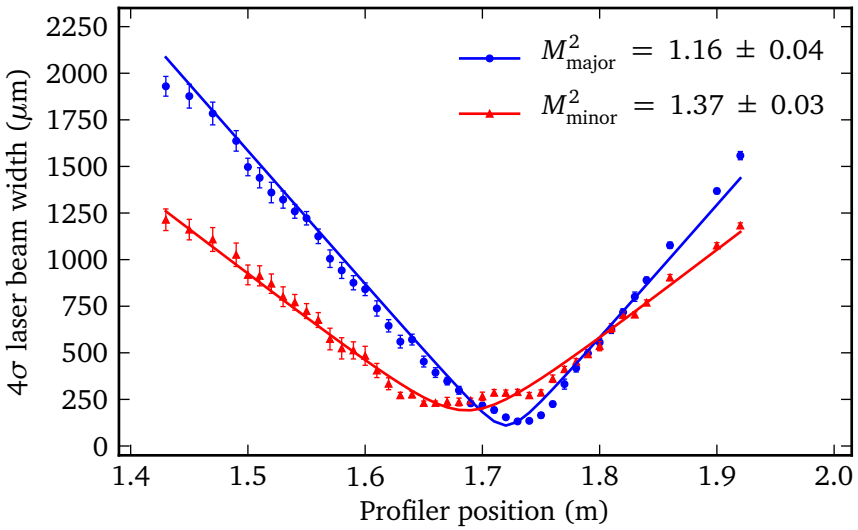


Figure 2.13. Measured $4\sigma$ width of the laser beam through the focus created with a $f = 1.677$ m lens.

This shows that the laser is astigmatic with different focused spot sizes at different locations with different divergences. The intrinsic axes of the laser were found to be rotated to the (extrinsic) lab axes by -17.4°.

The laser propagation was measured each week after maintenance was carried out on the laser system. The relevant measurement was used in the analysis of the laserwire data.

The laser pointing stability was measured at the end of the diagnostic line by recording 600 laser beam profiles. For each profile the centroid was calculated. The standard deviation of the centroids in the horizontal and vertical was measured to be 125.7 and 132.7 $\mu$m, respectively, at the laserwire lens. This spatial variation can be scaled by the beam size at the ratio of the input laser beam size to that at the LWIP to give a laser position variation of $\sim$ 40 nm in both dimensions. This spatial variation therefore systematically increases the measured electron beam size by $\sim$ 0.08% and, hence, can be neglected.

### 2.2.4 Alignment

Before performing the data taking, the laser and electron beams must be spatially and temporally overlapped in order to achieve collisions between them. The OTR screen was used as an alignment tool in both cases.

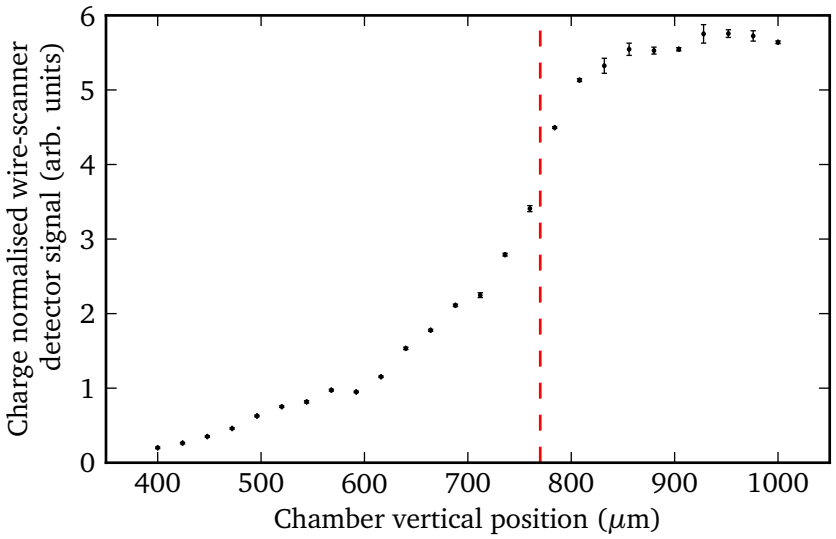


Figure 2.14. Measured bremsstrahlung radiation as a function of vertical chamber position with the OTR screen at the laser focus position. The red dashed line shows the chosen alignment position.

Firstly, before operations, the laser beam must be precisely aligned to the center of the laserwire lens as well as perpendicular to the vacuum window in order to achieve minimum possible laser spot size at the focus. As the first step, the low power alignment laser was guided through the optical path from the source to the vacuum window. Two mirrors before the LWIP were used to adjust the position of the laser such that its back reflection from the vacuum window overlapped with the incoming laser beam. After that, a mirror was placed in the kinematic laserwire lens mount and the angle of the mount adjusted until the reflected laser beam also overlapped the incoming laser beam. At the end the alignment was verified with the main laser beam at low power. After this procedure the mirror was removed and the laserwire lens was placed into the mount.

During the access before operations, strongly attenuated laser beam (so it does not cause the damage of the OTR screen) was sent to the LWIP. The OTR screen then was moved vertically to find the point where it intercept the laser focus. The moment of interception can be observed in the post-LWIP optics. In order to center the OTR screen at the laser focus along the axis of laser propagation ($x$ axis in Fig. 2.8), position of the OTR screen in $x$ direction was manually adjusted in such a way that the vertical distance required to intercept the laser beam was minimal. After that, during experimental shifts, the OTR screen was set to the reference position and the vacuum chamber with the OTR screen as a whole was scanned vertically until the electron beam was intercepted. When the OTR

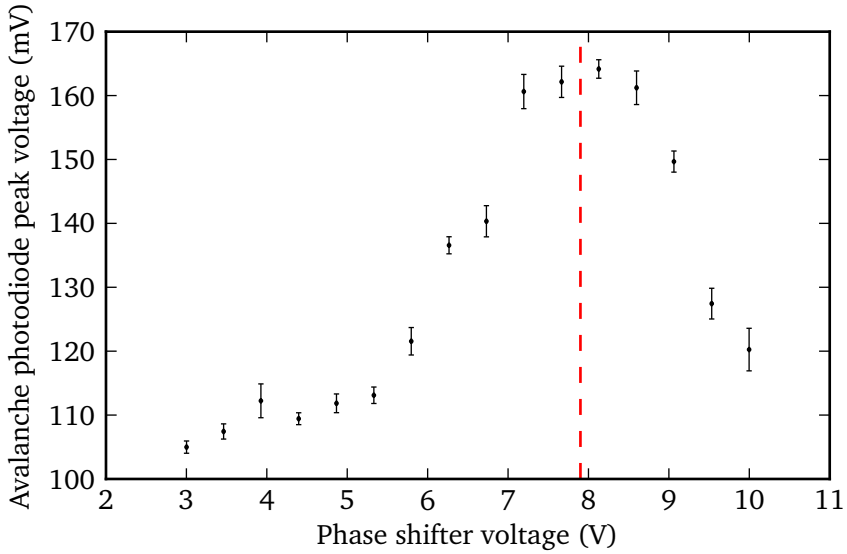


Figure 2.16. Peak APD signal as a function of phase shifter voltage. The red dashed line shows the chosen phase setting.

screen intercepts the electron beam bremsstrahlung radiation is produced. This radiation can be detected by the wire scanner detector located behind the laserwire detector. The chamber was aligned to the point where half the maximum bremsstrahlung radiation was produced. An example of the vertical alignment scan is presented in Fig. 2.14.

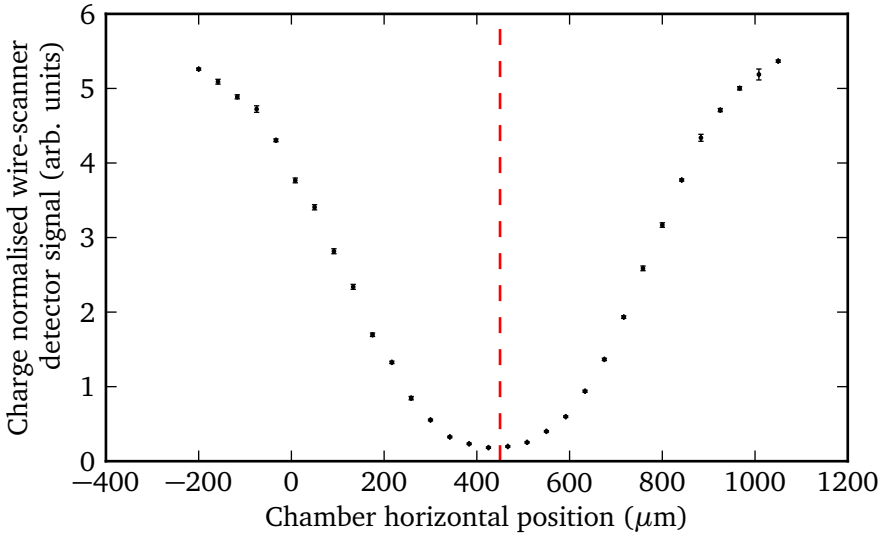


Figure 2.15. Measured bremsstrahlung radiation as a function of horizontal chamber position with the OTR screen at the laser focus position. The red dashed line shows the chosen alignment position.

To align the laser focus horizontally the same OTR screen was used. During the operation in 2011 the OTR screen was accidentally damaged by focused high power laser beam that created a semicircular hole at the bottom of the screen approximately 500 $\mu$m in diameter. This notch allowed the horizontal alignment of the chamber. The OTR screen

was raised approximately 200 $\mu$m above the electron beam which was found during the vertical alignment. Then the chamber was scanned in the horizontal $x$ axis. When the electron beam passes through the notch in the screen the intensity of bremsstrahlung radiation monitored by the wire scanner detector is dropped. The horizontal position of the vacuum chamber corresponding to the minimum of the radiation indicates the alignment of the electron beam to the laser focus. An example of the horizontal alignment scan is presented in Fig. 2.15.

For temporal alignment the OTR screen was moved above the laser focus reference position so the laser beam can pass through the LWIP to the APD. The vacuum chamber then was lowered so the electron beam can hit the screen and produce OTR which can also be detected by the APD. The APD signal was observed on a 1 GHz bandwidth, 5 gigasamples per second oscilloscope. Because of the bandwidth limitations of the APD, cables and the oscilloscope, both the laser and OTR signals are represented by approximately 1 ns pulses on the oscilloscope. To perform the alignment the laser light was attenuated to match the OTR signal level and the laser timing system was adjusted until the APD signal is doubled. This method allowed alignment within 40 ps which was sufficient to produce detectable collision.

Initially, the laser timing was roughly adjusted in integer clock cycles to align the laser and OTR signals as close as possible. Then the voltage-controlled phase shifter was used to adjust the phase between the electron beam and the laser pulses for precise alignment. The maximum voltage of the APD signal on the oscilloscope was then recorded as a function of the phase-shifter voltage. An example of the phase-shifter voltage scan is presented in Fig. 2.16. Position of the maximum of the obtained curve was used as the voltage that provides the best time overlap.

### 2.2.5 Signal linearity

In order to understand the detector linearity the electron bunch charge and laser pulse energy were varied independently and the Compton signal was recorded accordingly. The bunch charge was varied by changing the photocathode laser pulse energy. The bunch charge delivered to the extraction line varies very non linearly with the photocathode laser pulse energy, but settings were chosen to give approximately equidistant steps. Fig. 2.17 shows the Compton signal as a function of the electron bunch charge variation with no laser at the LWIP, as well as medium and maximum laser output power levels. As one can see, the picture shows linear dependence with charge in all cases. The charge variation was not continued to the highest bunch charge with the highest output laser pulse energy in order to avoid detector saturation during the measurement.

Afterwards, another set of scans was performed by varying the output laser pulse energy while keeping the bunch charge fixed. The resultant curves for different bunch charges are presented in Fig. 2.18. In that case, despite showing an approximately linear dependence of the signal with the laser pulse energy as expected, a greater degree of variation was observed. This non linearity is most likely due to the variation of the laser

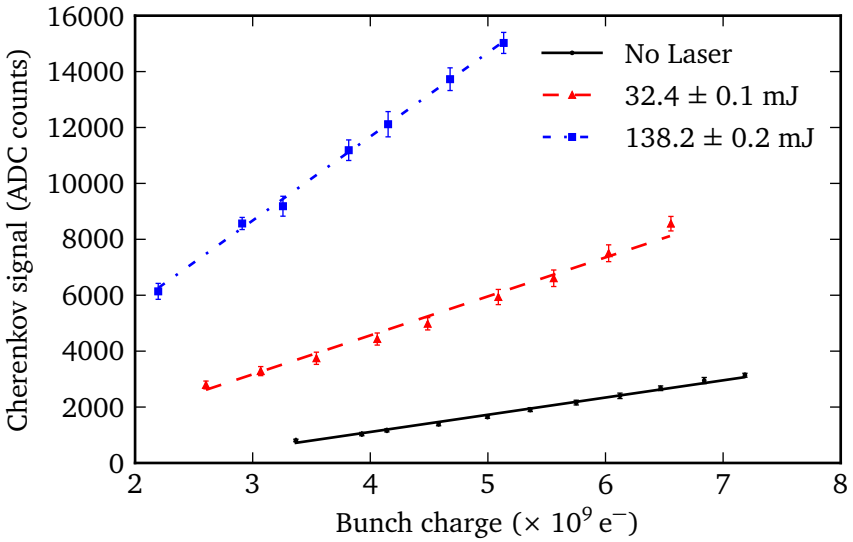


Figure 2.17. Variation of the Cherenkov signal with electron bunch charge for various laser levels.

profile with the laser pulse energy. The laser characterisation was performed at the laser pulse energy that would be used for operation.

From this linearity scans it is clear that the detector gives a linear response over the small range of variation of bunch charge and laser pulse energy during a complete laser-wire scan.

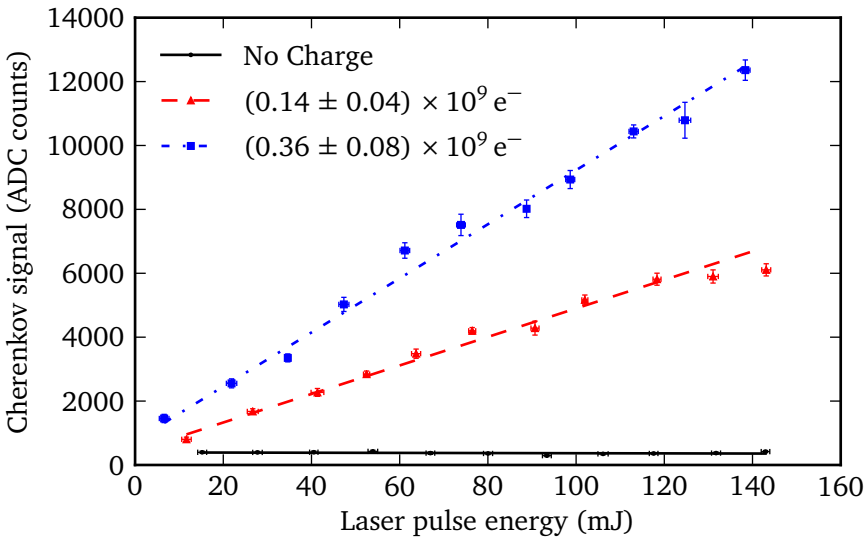


Figure 2.18. Variation of the Cherenkov signal with laser pulse energy for various electron bunch charges.

### 2.2.6 Results of the laserwire beam profile and emittance measurements at ATF2

After establishing a detectable collisions, the alignment between the laser and electron beams was optimized to produce maximum number of Compton scattered photons. This was achieved by scanning laserwire vertically, then in phase and then horizontally. The sequence of scans was repeated until no further improvement was observed.

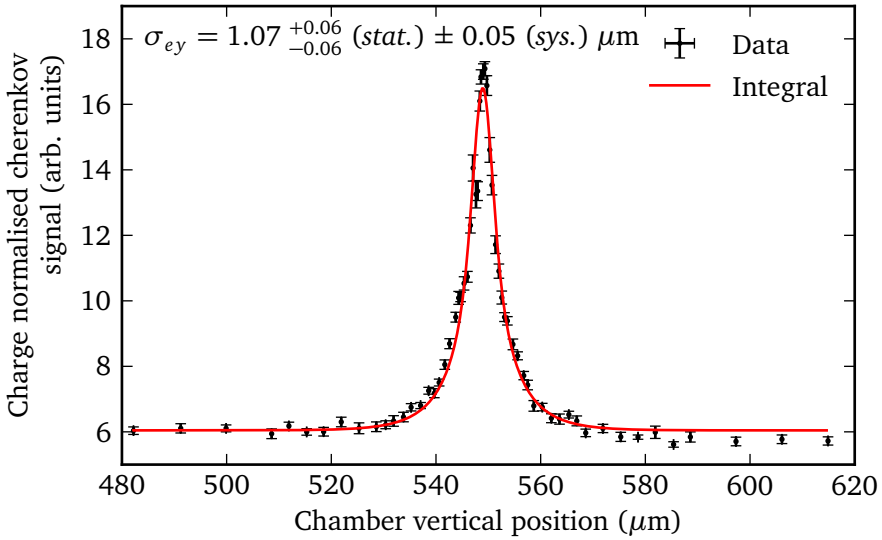


Figure 2.19. Vertical laserwire scan with nonlinear step size and the smallest measured electron beam size.

During the operations it was immediately realised that the vertical laserwire scans have non Gaussian shape with a narrow peak and broad tails observable up to 30 $\mu$m away from the peak. To accurately sample such shape in the minimum time, scans with variable step sizes were used (nonlinear scan). Initially, vertical scan with a low number of samples and linear step sizes was used to roughly determine the center of the scan. Furthermore, to deconvolve the vertical beam size from the scan Eq. 2.10 must be used. This requires knowledge of the horizontal electron beam size. To both optimize the alignment and measure the horizontal electron beam size, the laser focus was scanned horizontally across the electron beam within 3 mm range. After this, the vacuum chamber was positioned at the center of the horizontal scan and a detailed nonlinear vertical scan was performed.

The electron beam optics were manipulated to minimize the electron beam size at the LWIP. The vertical and horizontal laserwire scans are shown in Fig. 2.19 and Fig. 2.20 respectively. These scans were analysed together and represent the smallest vertical electron beam profile measured. These were recorded with an electron bunch population of 0.51 $\pm$ 0.05 $\times$ $10^{10}$ $e^{-}$.

The measured vertical electron beam size was 1.07 $\pm$ 0.06 (stat.) $\pm$ 0.05 (sys.) $\mu$m and the horizontal beam size was 119.0 $\pm$ 2.4 (stat.) $\pm$ 0.01 (sys.) $\mu$m [31]. The analysis was performed using Minuit minimization software using a weighted least square method that

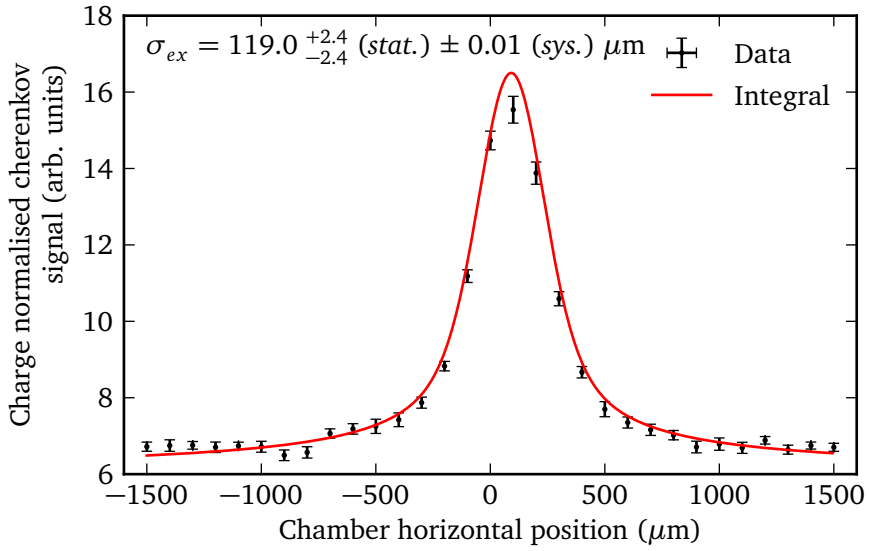


Figure 2.20. Horizontal laserwire scan for the smallest vertical scan.

allowed for asymmetrical uncertainties using the Minos algorithm [42]. The systematic uncertainties were calculated as a standard deviation of the fit parameters from randomly sampling the laser parameters from the $M^2$ model analysis with their associated uncertainties. The calculated laserwire signal from the fit as a function of vertical and horizontal chamber positions is shown in Fig. 2.21.

The laserwire was used to profile the electron beam throughout a quadrupole scan of the vertically focusing quadrupole (QM14FF) immediately before LWIP. The magnet current was varied from -80 A to -104 A in 3 A steps. At each point, a short range, low sample number vertical scan was performed to center the laser beam in vertical direction. After this, a detailed horizontal scan was performed followed by a nonlinear vertical scan. The horizontal and vertical scans were fitted together in order to extract horizontal $\sigma_{ex}$ and vertical $\sigma_{ey}$ electron beam sizes. Horizontal and vertical beam sizes as a function of QM14FF quadrupole current are presented in Fig. 2.22.

The quadrupole scan corresponding to the variation of the vertical electron beam size shows a clear hyperbolic focus as expected with a maximum measured size of 7.30 ± 0.16 (stat.) ± 0.17 (sys.) $\mu$m and a smallest size of 1.43 ± 0.05 (stat.) ± 0.04 (sys.) $\mu$m. The horizontal electron beam sizes demonstrate a nearly liner progression as expected. Such behaviour of the horizontal beam size during the scan is explained by the special design of the lattice. The beam entering the QM14FF quadrupole is astigmatic with a very broad focus in the horizontal plane (see Fig. 2.7). By varying the strengths of this quadrupole the vertical beam size changes sharply when the variation of the horizontal beam size is not noticeable. The horizontal scan shows a greater degree of variation from expected linear shape. This is due to variation in the electron beam energy over the time of the scans. The set of three laserwire scans required to make a measurement of the electron beam size takes approximately 20 minutes and the whole quadrupole scan is about 3.5 hours. A low electron beam bunch charge (0.2 × $10^{10}$ $e^-$) was used during the scan in

order to provide the most stable condition over the duration of the measurement.

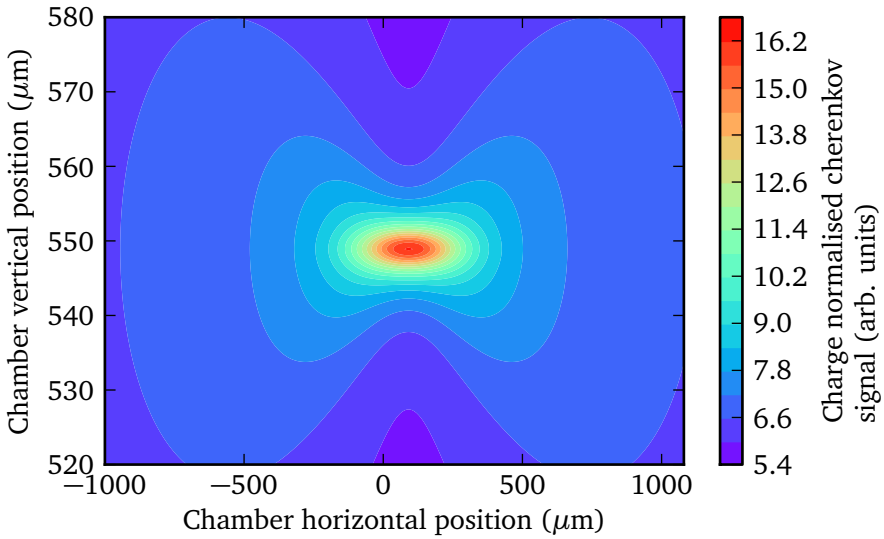


Figure 2.21. Calculated laserwire signal for a range of horizontal and vertical chamber positions from the simultaneous fit of the horizontal and vertical laserwire scans.

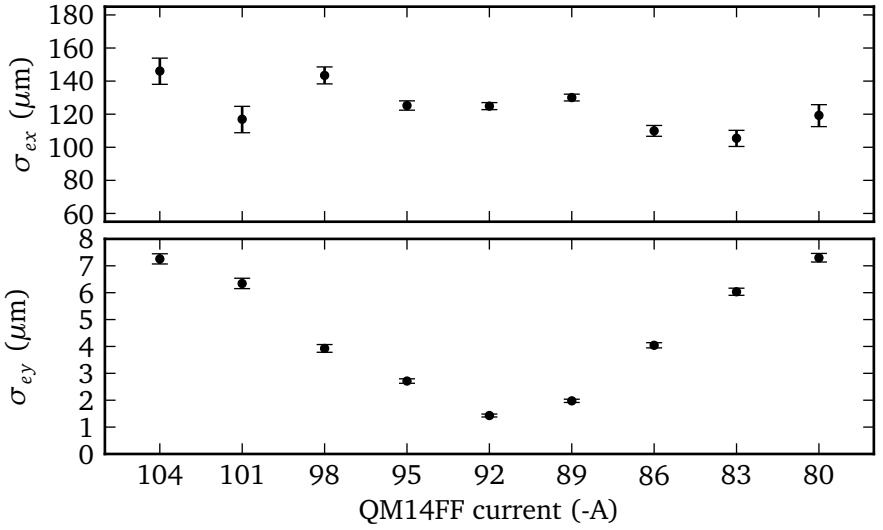


Figure 2.22. Horizontal (top) and vertical (bottom) electron beam sizes measured for various currents of QM14FF quadrupole.

As described in section 2.1 the quadrupole scan allows to reconstruct the emittance of the electron beam. Measured vertical electron beam size as function of QM14FF integrated quadrupole strength is presented in Fig. 2.23. Experimental data was fitted with second order polynomial using thick lens formalism (see Eq. 1.29). There is only a drift section between QM14FF quadrupole and the LWIP, so $L$ in Eq. 1.27 is the drift distance, 692 $\pm$ 1 mm. Using the values from the fit the measured geometrical emittance was calculated using 1.30 and found to be 82.56 $\pm$ 3.04 pm rad. This value is a relatively large emittance compared to the typical optimized vertical value of the ATF2, which in the damping ring

is 10 pm and 10 – 30 pm in the extraction line. The extraction line optics optimization procedure was not carried out in full for laserwire operation periods and higher emittance values are to be expected.

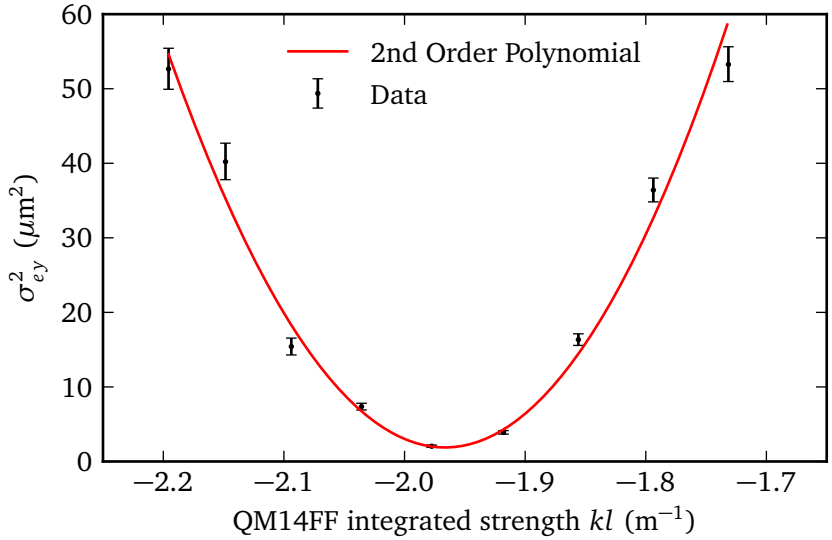


Figure 2.23. Measured electron beam size squared as a function of QM14FF strength.

## 2.3 OTR cross-check monitor

The laserwire beam profile monitor, described in the previous section is the state-of-the-art in transverse beam diagnostics providing micron scale resolution, non-invasive beam size measurements. However, at a current state it requires a team of people looking after a high power laser, detailed laser and optical system alignment, day-by-day operation and maintenance. Moreover, the use of high power laser significantly increases the cost of the laserwire system. Thereby, a simpler and relatively inexpensive method to measure micron-scale beam sizes is required both to confirm the laserwire performance and reliability and to be a supplementary monitor wherever it can be used. A beam profile monitor based on OTR is very promising. It is widely used to measure a few micrometre beam size which is just above the diffraction limit [43, 44]. This is one of the best monitors which is simple in use and gives a two-dimensional beam profile in a single shot. Although such a monitor destroys the beam or the beam can destroy the monitor itself, it still can be used to backup the laserwire for diagnostics of low current “pilot” beams.

Transition radiation arises when a relativistic, uniformly moving charged particle crosses a boundary between two media with different optical properties (for example a vacuum-metal interface). First, transition radiation was predicted and described theoretically by Ginzburg and Frank in 1946 [45]. Experimentally, transition radiation in the optical wavelength region was observed in 1959 [46]. Since then the transition radiation theory has been developed by many authors [47–49].

A so-called Point Spread Function (PSF) defines the resolution of the OTR monitors. In

classical optics the PSF is an image generated by a point source emitting a spherical wave which is projected by an optical system on a detector. Due to the diffraction effects the image from a point object is no longer a point, but rather an extended distribution with dimensions defined by the wavelength and the optical system angular aperture. In case of OTR the PSF has a different definition. The OTR PSF is an image from a source induced by a single electron on a target surface and projected by an imaging optical system on a detector. As a matter of fact the source generated by a single electron is not a point but a distribution defined by the shape and dimensions of the charged particle electric field. In [14] the first observation of the OTR PSF was presented and demonstrated that its vertical polarization component has a two-lobe distribution. It was also very clear that the visibility of the pattern strongly depends on the electron beam size. In [50] the first attempt to demonstrate the sensitivity of the OTR PSF to the beam size has been performed.

### 2.3.1 Theory

Consider a single particle with a charge $q$ and energy $\gamma$ moving uniformly and rectilinearly in a vacuum and intersecting a metal screen with a perfect conductivity resulting in transition radiation. Assuming an optical system with an aberration free lens with radius $d$ located at distance $a$ from the source (which in this case is the OTR screen) and $b$ from the image plane the vertical component of the OTR electric field at an image point $P(\rho = \sqrt{x^2 + y^2}, \phi)$ is given by [51]:

$$E_y(P,\omega) = -\frac{2\pi q}{v\lambda M}\sin\phi \int_0^{\theta_{lens}} \mathrm{d}t\, \frac{t^2}{t^2 + (\beta\gamma)^{-2}} \left(\sqrt{1-t^2}+1\right) J_1\left[\frac{2\pi\rho t}{\lambda M}\right]. \tag{2.14}$$

Here $M = b/a$ is the lens magnification factor, $\lambda$ is the wavelength of the radiation, $J_1$ is the Bessel function of the first kind and $\theta_{lens} = d/a$ is the acceptance of the lens. The intensity distribution in the image plane can be obtained using the common formula [6]:

$$S(\rho,\omega) = \frac{c}{4\pi^2}|E_y|^2 \tag{2.15}$$

The OTR field described by Eq 2.14 is derived for a single particle and thus Eq. 2.15 represents the PSF. For a bunch of particles the resulting image is a convolution of the PSF with the transverse distribution of the bunch.

The intensity distribution of the OTR calculated for the ATF2 parameters is presented in Fig. 2.24. In order to demonstrate how the diffraction effects influence the OTR PSF a projection of the intensity distribution in vertical direction has been calculated for different angular acceptances of the lens $\theta_{lens}$ and is shown in Fig 2.25. As one can notice, diffraction effects lead to the broadening of the PSF and hence to worse resolution. The theoretical study of the diffraction effects and how they affect the spatial resolution in OTR beam diagnostics has been developed in [51–53].

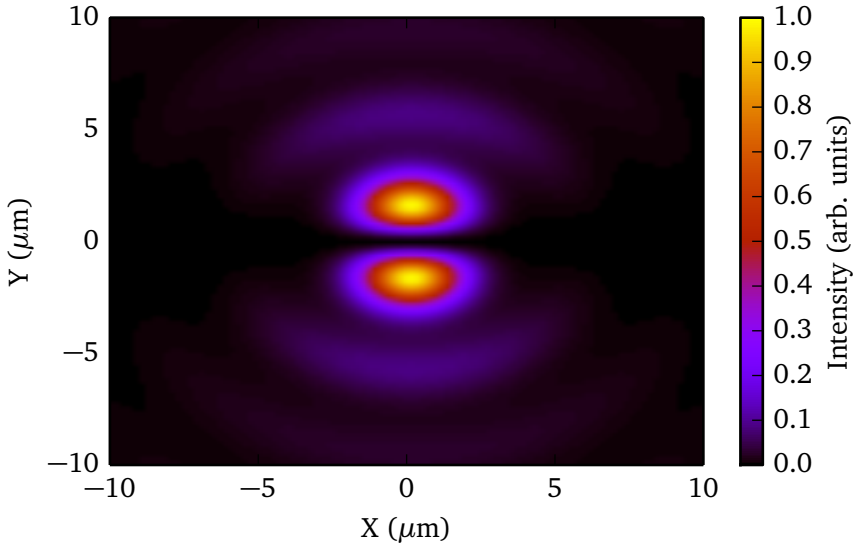


Figure 2.24. OTR distribution calculated using Eq. 2.15 for $\gamma = 2500$ and $\lambda = 550$ nm.

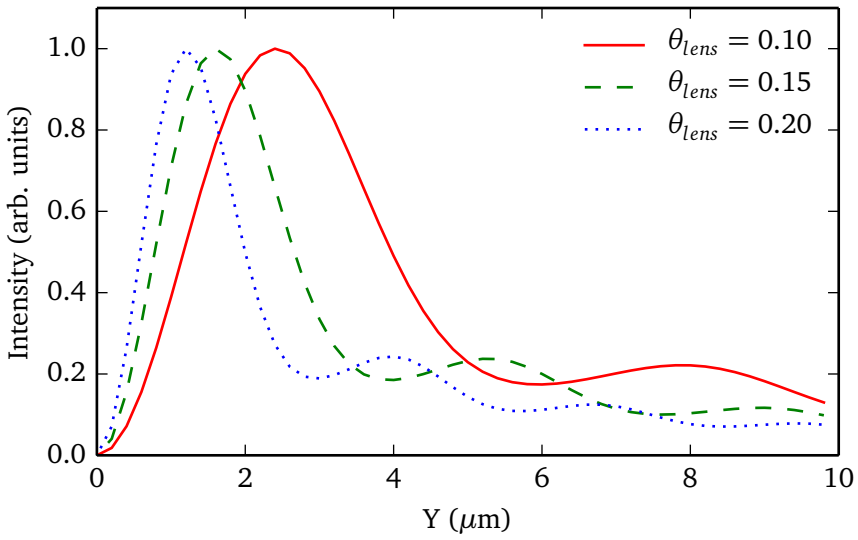


Figure 2.25. Vertical projection of the OTR intensity distribution for different values of the angular acceptance of the lens $\theta_{lens}$. Parameters: $\gamma = 2500$, $\lambda = 550$ nm.

Besides the diffraction, different aberration effects (chromatic and geometric) also limit the resolution of the OTR beam diagnostics. Theoretical study of the aberration effects is very difficult. Instead a simulation software such as ZEMAX [54] can be used for these purpose. The Physics Optics Propagation mode of ZEMAX allows to propagate the OTR field through realistic optical components using diffraction laws. ZEMAX offers a large database of commercially available optical components (lenses, mirrors, polarazers, etc.) which can be used to simulate any optical system and evaluate different errors occuring along the optical path. In order to understand the limitations and improve the resolution of the optical system for the OTR beam profile monitor a series of numerical simulations using ZEMAX have been performed [55–57]. Results of these simulations

have been compared with the experimental study of the aberration effects which will be described in section 2.3.8 of this chapter.

### 2.3.2 Experimental setup

Initially the OTR system was used in combination with laserwire system to cross check the laserwire results, provide the initial horizontal beam size required in order to deconvolve the beam size from the laserwire scan and for spatial and temporal alignment of the laserwire system. Since the beginning the general structure of the OTR experimental setup has remained unchanged [50, 58].

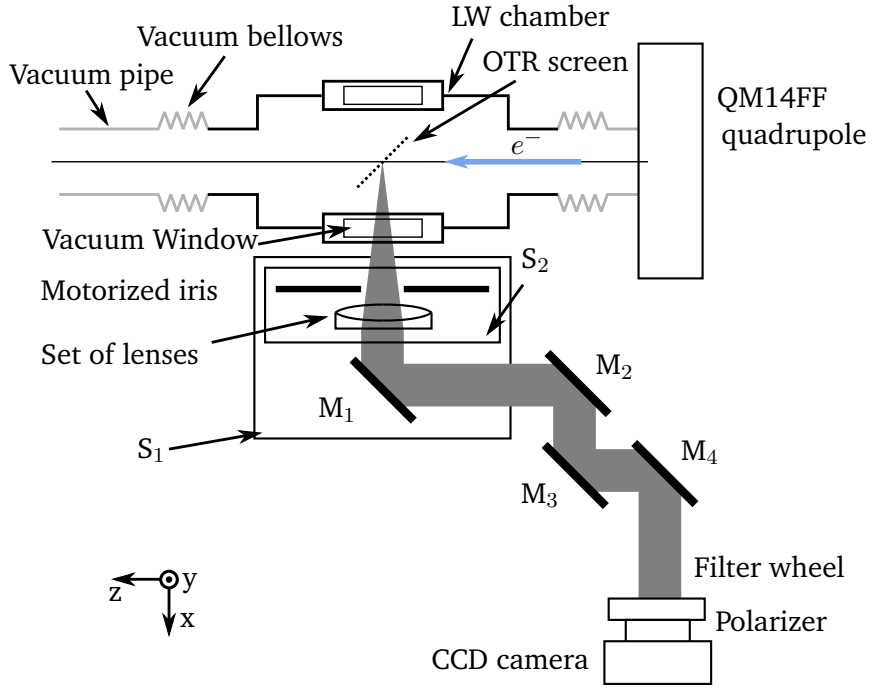


Figure 2.26. Schemaic of the OTR beam profile monitor setup.

In order to study the optical system and achieve better resolution, in 2013 new optical elements have been added to the experimental setup [59, 60]. A schematic and a photograph of the experimental setup is presented in Fig. 2.26 and 2.27 respectively.

To produce the OTR beam a 30×30×0.3 mm aluminized silicon target was used. The target was tilted at 45° with respect to the electron beam direction. Vertical position of the target was controlled by 4D vacuum manipulator installed at the top of the vacuum chamber. The OTR beam passes through the optical system which consists of a motorized iris, a lens holder with a set of lenses, a periscope of mirrors ($M_1$–$M_4$), a filter wheel with a set of optical filters, a polarizer and a CCD camera. The iris and the lens holder were mounted on the same board to keep them centred. The lens holder mounted on the board has a possibility of 3D adjustment of the lens position. Filter wheel with a set of optical filters followed by the polarizer was attached to the CCD camera and mounted on a remotely controlled rotation stage. The whole setup was mounted on a bread board and

placed in a light protective enclosure. The full specification of the main components is presented in Table 2.2.

Table 2.2. Specification of the main components of the experimental setup.

| **Component** | **Properties** |
|---|---|
| VW | Vacuum window: “CVI Laser Optics” W2-PW-2050-UV-532-0-27 |
| $M_1$ | motorized aluminum mirror, $\varnothing$ = 50 mm , mount: “Thorlabs” [61] PT1-Z8, motor: Z625B |
| $M_2$- $M_3$ | aluminum mirror, $\varnothing$ = 50 mm |
| $M_4$ | aluminum mirror, $\varnothing$ = 75 mm |
| $S_1$ | lens transverse stage: “PI” [62] PI-410.2S |
| $S_2$ | lens focus stage: “Thorlabs” PT1-Z8, motor Z625B lens vertical stage: “Sigma-Koki” [63] SGSP 60-10ZF |
| $S_3$ | rotation stage: “Suruga Seiki” [64] K402-160-5 |
| Lens | ”CVI Laser Optics” cemented achromat, $f$=120 mm, $\varnothing$=30 mm |
| Iris | “Standa” [65] 8MID98-4-90 |
| Filter wheel | “Thorlabs” FW102B |
| Polarizer | “Sigma-Koki” SPF-50C-32 |
| CCD camera | “SBIG” [66] model: SBIG-ST8300M based on Kodak KAF-8300 (monochrome) sensor with 5.4 $\mu$m pixel size, 3352$\times$2532 pixel array and $\sim$50% quantum efficiency |

To align the optical system a special alignment laser system was used. This system is located approximately 25 m upstream the LW chamber and consists of a laser stage equipped with continuous wave (CW) He – Ne (Helium - Neon) laser with 632.8 nm output wavelength, a spatial filter, a focusing lens and a vacuum mirror. The vacuum mirror is used to send the laser along the beam line to the ATF2 extraction line. Changing the distance between spatial filter and the focusing lens one can focus the laser beam at each point of the optical system. After tuning the laser and sending it to the beam pipe the OTR screen was placed at 45 degrees with respect to the beam line to reflect the laser out from the vacuum chamber and to align the entire optical system.

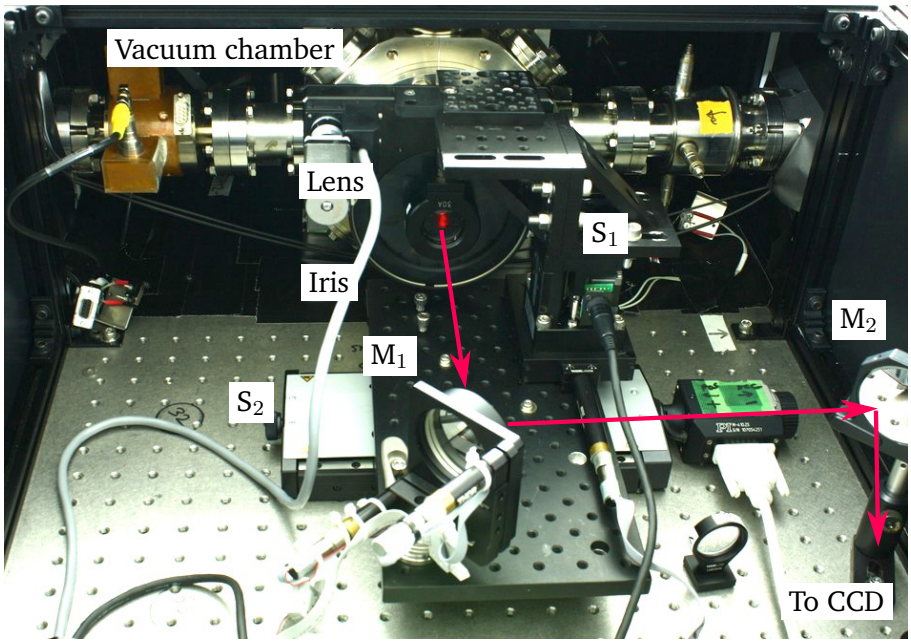


Figure 2.27. Photograph of the OTR beam profile monitor setup.

### 2.3.3 Calibration

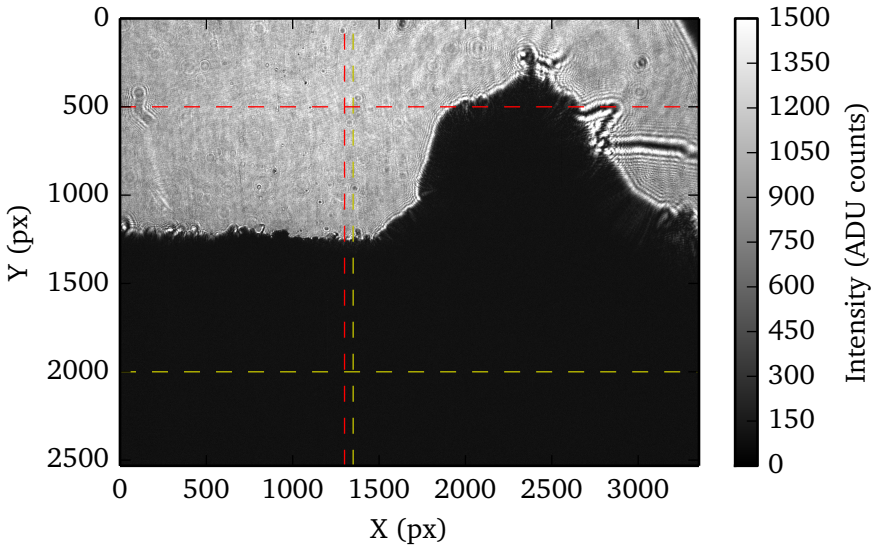


Figure 2.28. CCD image of the OTR screen.

Magnification factor is one of the essential parameters of the optical system and it is required in order to convert sizes on OTR image from pixels to microns as:

$$\frac{x_i^{\mu m}}{m} = \frac{x_i^{pixel} \times \text{binning} \times \text{pixel size}}{\text{magnification factor}} \tag{2.16}$$

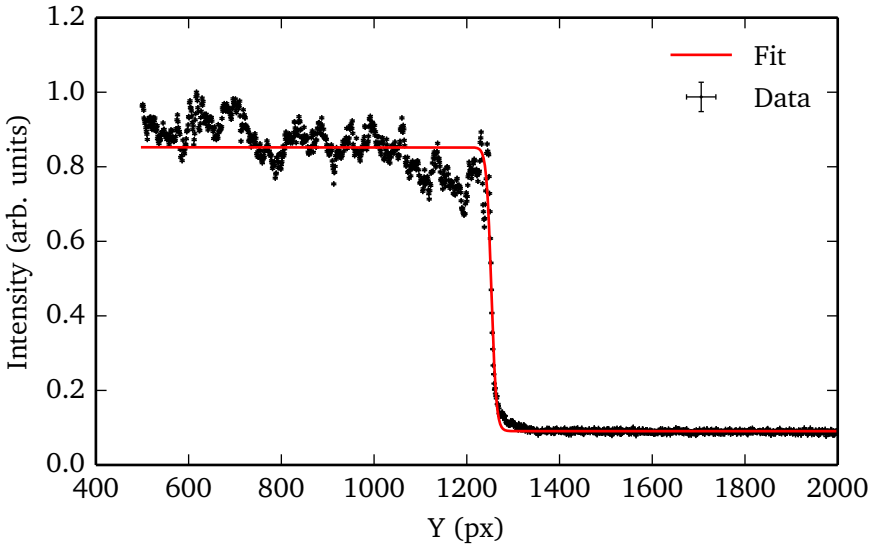


Figure 2.29. Vertical projection of the OTR screen edge.

In order to calibrate the optical system and measure the magnification factor the following procedure was used. The OTR screen was gradually moved out of the vacuum chamber. At each step the image of the OTR screen edge (due to reflected laser light) was recorded by the CCD camera. A position of the target was obtained from the manipulator motor controller encoder system with $\pm$ 5 $\mu$m precision. To obtain the position of the screen edge the image of the target was digitized and the vertical projection in a rectangular box (see Fig. 2.28) was fitted using:

$$f(x) = a_0 + \frac{a_1}{1 + \exp\left(\dfrac{x - a_2}{a_3}\right)}. \tag{2.17}$$

Here, $a_0$, $a_1$, $a_2$, $a_3$ are the free fit parameters. Parameter $a_2$ represents the screen edge

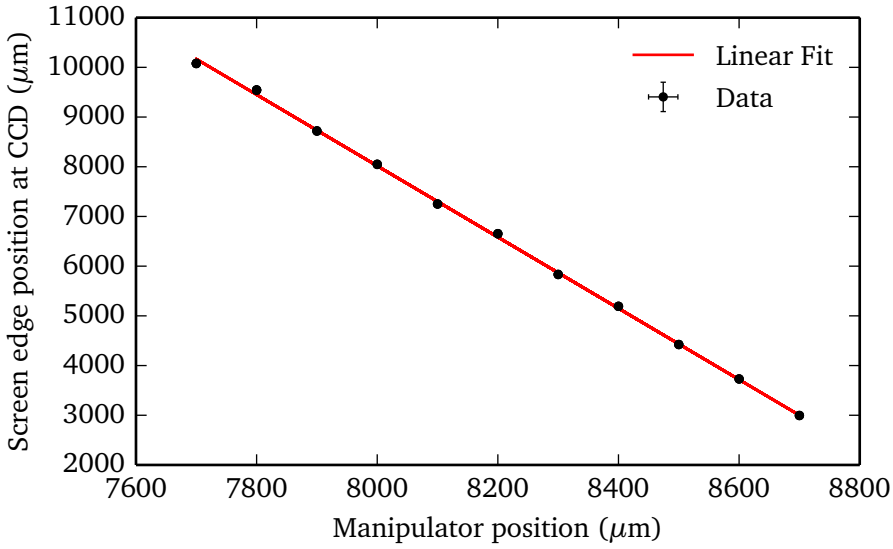


Figure 2.30. Calibration curve.

position. The vertical projection of the screen edge image with the fit function is presented in Fig. 2.29. The dependence of the screen edge position measured at the CCD camera versus manipulator position was used as a calibration curve. Then, the calibration curve was fitted using linear function (see Fig. 2.30). Gradient of the line is the magnification factor which was found to be 7.17.

### 2.3.4 Beam based alignment and tuning

Before each operational shift the following tuning procedure has been applied to the OTR beam profile monitor in order to maximize its resolution.

First, the CCD camera was set to the low resolution mode in order to decrease time required to acquire the image. The camera software was switched to the automatic mode which allows the on-line, shot-by-shot, monitoring of the acquired images. To increase the intensity of the OTR light coming to the CCD camera optical filters were removed from the optical line. After that, the angle of the mirror $M_1$ (see Fig. 2.26) in horizontal and vertical direction has been adjusted by means of two remotely controlled actuators attached to the mirror holder until the OTR spot was found.

Once the OTR spot was found and centred at the image, the longitudinal position of the focusing lens was adjusted to minimize the size of the OTR spot and maximize its visibility. To define the best lens position a so-called focusing scan was performed. The focusing lens was gradually moved and at each lens position the OTR image was recorded and vertical projection of the image was calculated. The width of the vertical projection (distance between peaks) as a function of the longitudinal lens position (an example of the focus scan is presented in Fig. 2.41) then was fitted using parabolic function. The minimum of the fit function corresponds to the best position of the lens. Initially, the vertical and horizontal position of the focusing lens was adjusted during the calibration procedure (see previous section) in such a way that the alignment laser has passed the lens at the very centre. During the operational shifts horizontal and vertical position of the lens was corrected until the equal light intensity between the lobes of the OTR distribution has been reached.

At last, the CCD camera was set back to the high resolution mode and optical filters were applied. After described above tuning operations the monitor was ready to perform beam size measurements.

### 2.3.5 Analysis

A typical CCD image of the OTR spot taken with linear polarizer and 550$\pm$20 nm optical filter is presented in Fig. 2.31.

To begin with, image noise and bad pixels are removed using a median filter [67] in which $n \times n$ pixel sub-frame is moved through the image, replacing central pixel with the mean of remaining pixels within the frame if it runs over a given threshold.

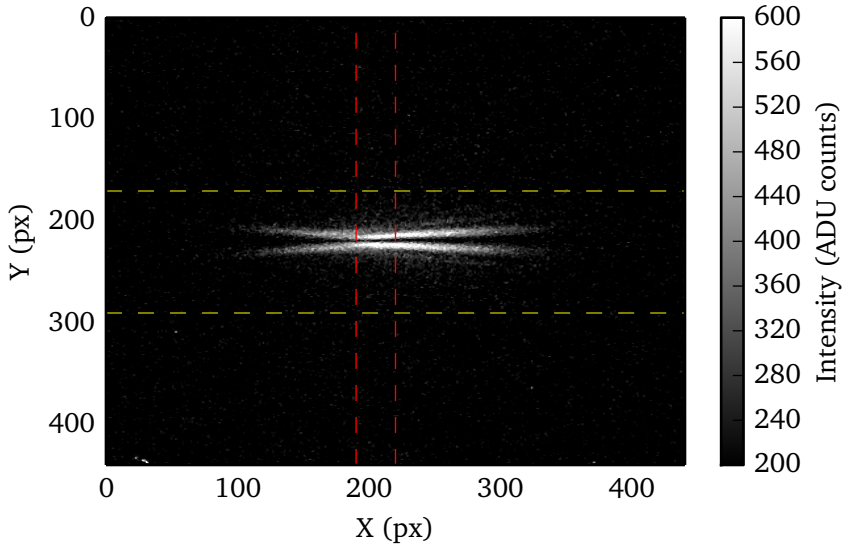


Figure 2.31. CCD image of the OTR spot taken with linear polarizer, 550±20 nm optical filter and focusing lens with $f$ =120 mm focal length.

The next step in image processing is pixel-by-pixel background subtraction with correct error propagation as:

$$STD^{sub}_{pixel} = \sqrt{\left(STD^{image}_{pixel}\right)^2 + \left(STD^{background}_{pixel}\right)^2}, \tag{2.18}$$

where the standard deviation for a pixel is defined as [68]:

$$STD_{pixel} = \sqrt{\text{gain} \times N}. \tag{2.19}$$

Here $N$ is the amplitude detected by a pixel and gain of a CCD camera represents the con-

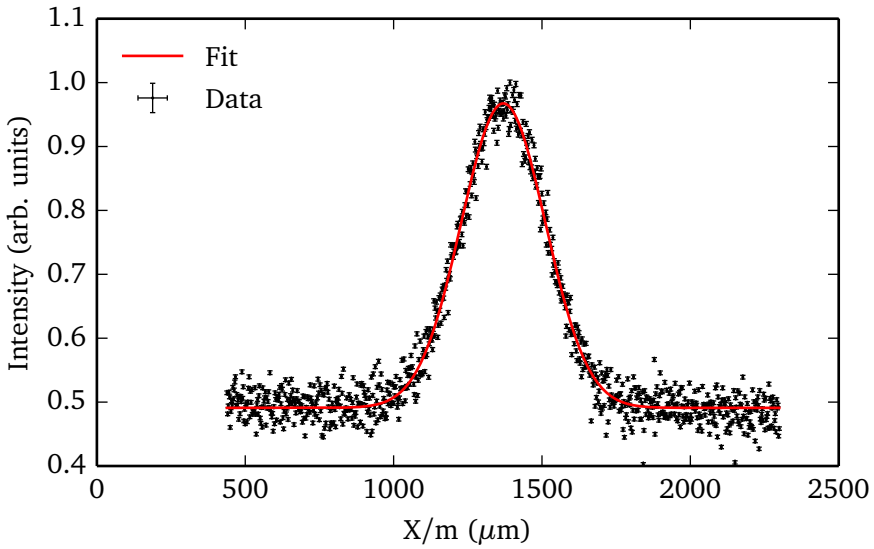


Figure 2.32. An example of the horizontal projection of the OTR image along with the associated fit function.

version factor from electrons ($e^-$) into digital counts, or Analogue-to-Digital Units (ADUs). Gain is expressed as the number of electrons which get converted into a digital number, or electrons per ADU (e-/ADU). Gain values are selected by the camera manufacturer to maximize the dynamic range available from any given sensor.

After that, an integration window is defined in which a portion of resulting image is used to produce horizontal or vertical projections summing rows or columns respectively.

Since the horizontal beam size is much bigger than the vertical one, the horizontal RMS beam size can be directly obtained from the symmetric Gaussian fit applied to the horizontal projection. An example including the uncertainties calculated using Eq. 2.18 is shown in Fig. 2.32. This horizontal projection was obtained by integration of the image in FIg. 2.31 within the borders indicated by dashed yellow lines. The PSF dimension in the horizontal direction is much smaller than the horizontal beam size. Therefore, the horizontal projection gives the horizontal electron beam profile. A Gaussian fit was used in Fig. 2.32 which resulted in a beam size of 142.189±0.139 $\mu$m, which is consistent with expectations from SAD [69].

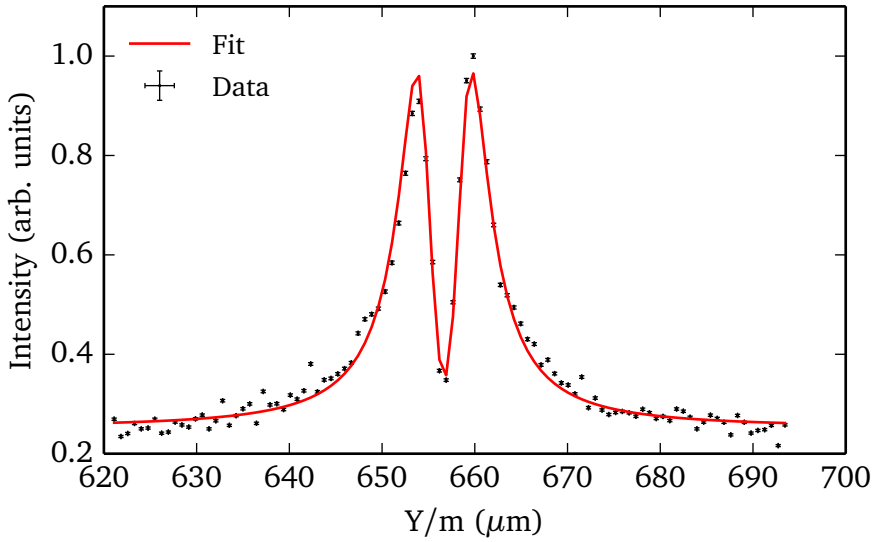


Figure 2.33. An example of the vertical projection of the OTR image along with the associated fit function.

The vertical projection of the OTR image has a two-lobe structure (an example obtained from the integration of the image in Fig. 2.31 within the borders indicated by dashed red lines is shown in Fig. 2.33) and the vertical beam size can not be directly obtained from the fit function applied to it. The idea of the vertical beam size extraction is based on fact that the contrast ratio of the distribution, which is defined as the ratio of the central minimum intensity to the maximum intensity, strongly depends on the real beam size.

In order to analyse the vertical projection the following, empirically found fit function has been proposed:

$$f_1(x) = a_0 + \frac{a_1\left(a_4 + (x - a_3)^2\right)}{1 + \left(a_2\,(x - a_3)\right)^4}, \tag{2.20}$$

where fit parameters are: $a_0$ the vertical offset of the distribution with respect to zero; $a_1$ the amplitude of the distribution; $a_2$ the smoothing parameter; $a_3$ the horizontal offset of the distribution with respect to zero and $a_4$ the distribution width. This fit function is advantageous because the distribution has a simple form allowing the contrast ratio to be calculated analytically. The contrast ratio calculated from the fit function parameters is given by:

$$\frac{I_{min}}{I_{max}} = \frac{2a_2^2 a_4}{a_2^2 a_4 + \sqrt{1 + a_2^4 a_4^2}}. \tag{2.21}$$

In addition, the peak to peak distance can also be calculated analytically as:

$$\text{Peak Distance} = \frac{2\sqrt{-a_2^2 a_4 + \sqrt{1 + a_2^4 a_4^2}}}{a_2}, \tag{2.22}$$

which is important for tuning and alignment of the optical system which strongly affects the resolution of the beam size measurements.

The numerical fit uses the Levenberg-Marquardt method [70] to calculate the best fit parameters which minimise the weighted mean squared error between the data and the fit function. The error propagation has been performed using the standard method as [71]:

$$\Delta f(a_0, ..., a_n) = \sqrt{\sum_{i=0}^{n} \left(\frac{\partial f(a_0, ..., a_n)}{\partial a_i}\right)^2 \Delta a_i^2}. \tag{2.23}$$

Here $\frac{\partial f(a_0, ..., a_n)}{\partial a_i}$ is the partial derivative with respect to each fitting parameters and $\Delta a_i$ is the error in each fitting parameter. In Eq. 2.23 $\Delta f$ can be an uncertainty for $f_1(x)$, $I_{min}/I_{max}$ or Peak Distance.

As it was mentioned before, the OTR PSF contrast ratio predominantly depends on the transverse beam size. In order to convert the contrast ratio to the beam size, a self-calibration procedure has been developed. To perform a calibration procedure a data set with varying vertical beam sizes is required. For each file, the PSF-like fit is used and the contrast ratio is extracted. The file with the smallest contrast ratio is then used for calibration as it is the closest fit to the original PSF generated by a single electron. The fit curve for that file is then regenerated setting $a_0$ to zero removing any offset due to the constant background and $a_4$ to zero in order to eliminate the distribution smoothing. We assume that such distribution represents the OTR PSF for a zero beam size.

Assuming that the beam profile has Gaussian shape, a numerical convolution with the fit function is performed to take into account the effect of the beam size:

$$F(y) = \frac{\sum_{j=1}^{N} f(y_j) \exp\left(-\frac{(y-y_j)^2}{2\sigma^2}\right)}{\sum_{j=1}^{N} \exp\left(-\frac{(y-y_j)^2}{2\sigma^2}\right)} \tag{2.24}$$

The plot in Fig. 2.34 shows the effect of beam size on the PSF-like distribution. Increasing the sigma of the convolution slowly increases the contrast ratio until the minimum disappears. The errors are also propagated through the convolution according to Eq. 2.23. The convolution is repeated $N$ times increasing $\sigma$ with a fine step from zero. For each iteration, the contrast ratio $I_{min}/I_{max}$ is found along with its errors $\Delta_{I_{min}/I_{max}}$ resulting in calibration curve. The convolution is repeated until the maximum contrast ratio of unity is found.

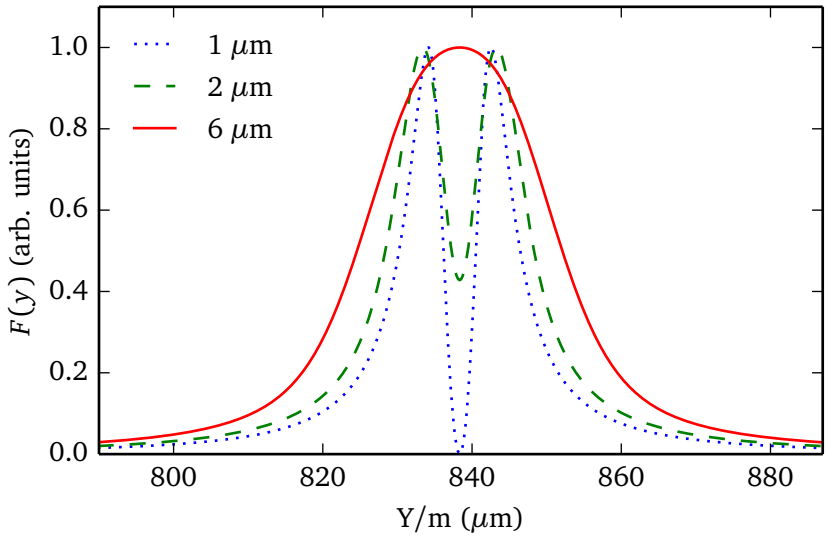


Figure 2.34. The effect of the beam size.

Finally, one need to obtain a calibration curve $\sigma = f(I_{min}/I_{max})$. For that purpose, the following empirically found fit function is used:

$$\sigma(I_{min}/I_{max}) = b_0 + \frac{1}{b_1}\left(-\log\left(1 - \frac{I_{min}/I_{max}}{b_2}\right)\right)^{b_3} + b_4(I_{min}/I_{max})^{12}, \tag{2.25}$$

where $b_0, ...b_4$ are free fit parameters. An example calibration curve presented in Fig. 2.35. The resultant curve exhibits a symmetric nature with larger errors at each end due to the increased gradient in this area. With the calibration curve now determined, it can be used to extract vertical beam size for each image in the data set. Again to calculate the uncertainties Eq. 2.23 was used, including uncertainties of all five fit parameters and $\Delta_{I_{min}/I_{max}}$. Uncertainties $\Delta_{I_{min}/I_{max}}$ appear at the calibration curve as horizontal errors. They can be converted to vertical errors with a good approximation by multiplying them to the slope of the line $\Delta_y/\Delta_x$.

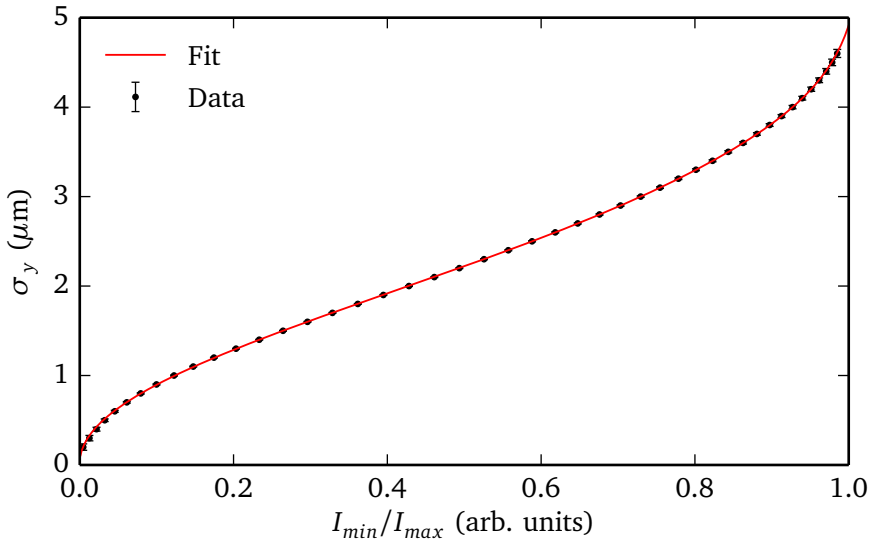


Figure 2.35. An example of the calibration curve.

The choice and position of the integration window affects the contrast ratio and therefore, the beam size. Fig. 2.36 shows how changing the gap size affect the contrast ratio. At small gap sizes, the quality of the fit produces a noisy contrast ratio. At very large gap size, a large amount of extra noise is integrated leading to an artificially high contrast ratio. In order to choose the correct region, the correlation of contrast ratio to the extracted beam size was used. The correlation is shown in Fig. 2.37. Ideally, this correlation must be zero, because the real beam size does not change. However we observe linear correlation which suggests that the pixel-by-pixel noise is accumulated linearly. The correct region for the gap size was chosen to be where the correlation has the densest number of points within 5% of the beam size variation which fits well in the beam size measurements accuracy. In Fig. 2.36, this is shown as the highlighted red region.

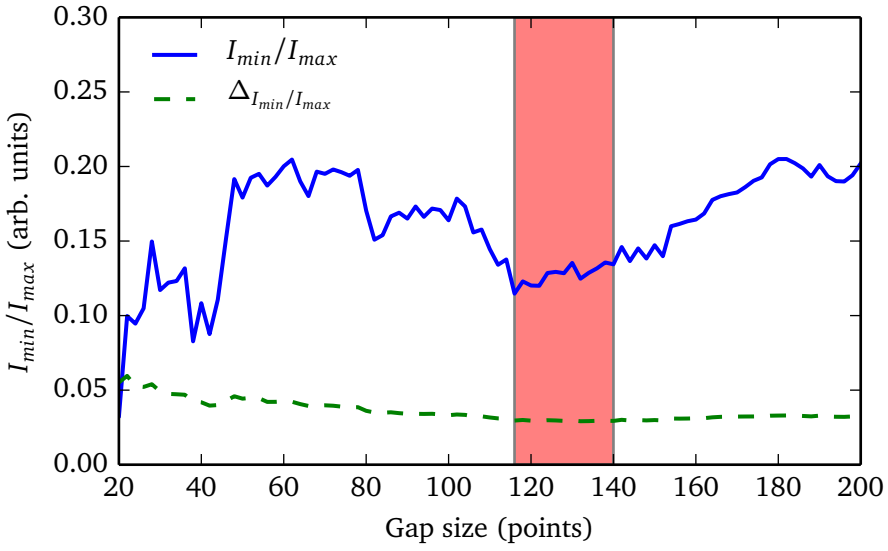


Figure 2.36. The contrast ratio and its error as a function of gap size.

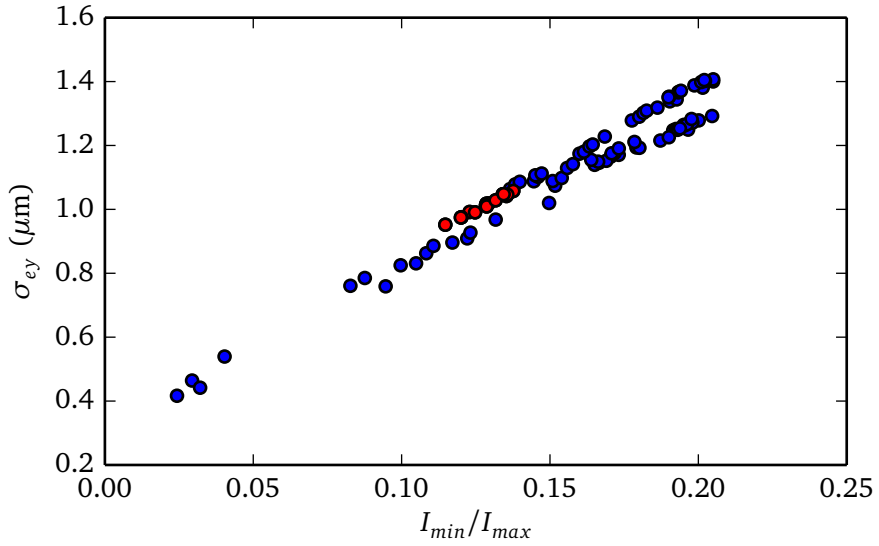


Figure 2.37. The correlation between contrast ratio and calibrated beam size for each gap size. The red dots are represent the densest correlated region. This region is represented on the Fig. 2.36 as the highlighted area.

### 2.3.6 OTR PSF beam size measurements

Initially the accelerator was carefully tuned to minimize the background level and provide a stable working regime during the data taking. The longitudinal position of the focusing lens was adjusted to provide a clear OTR image with a minimum peak to peak distance. After that, the monitor was ready to perform beam size measurements. All measurements were performed in single-bunch mode, with a bunch repetition rate of 3.12 Hz and ∼0.3 nC bunch charge.

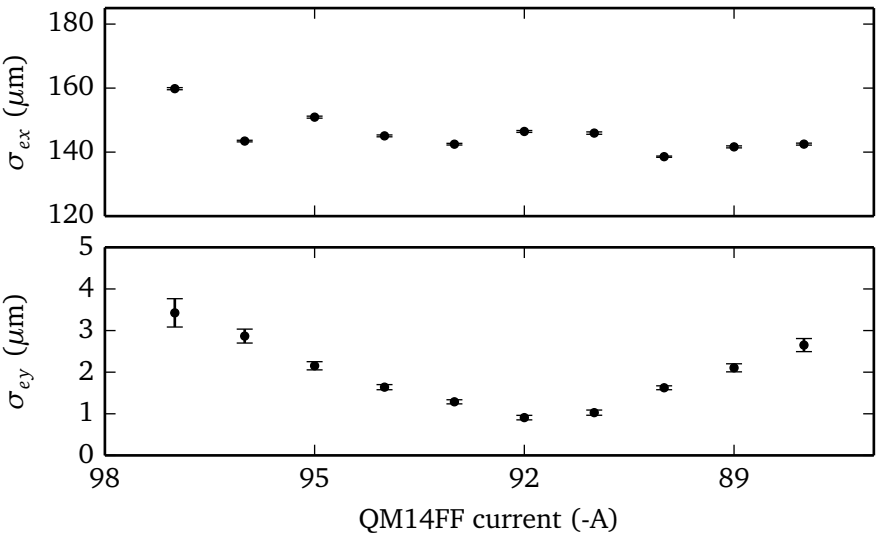


Figure 2.38. The measured horizontal (top) and vertical (bottom) electron beam sizes as measured by the OTR system using QM14FF quadrupole at different currents.

A quadrupole scan was then performed in which the current of the QM14FF quadrupole magnet was changed in a range from -88 A to -97 A in steps of 1 A. For each value of the quadrupole current, three OTR images were taken in order to minimise the statistical errors. Figure 2.38 shows the measured horizontal and vertical beam sizes at each current. It can be seen that the horizontal beam size remains roughly constant at around $\sim$145 $\mu$m as desired while the beam size in the vertical direction shows a hyperbolic dependence with a minimum beam size of 0.754$\pm$0.034 $\mu$m.

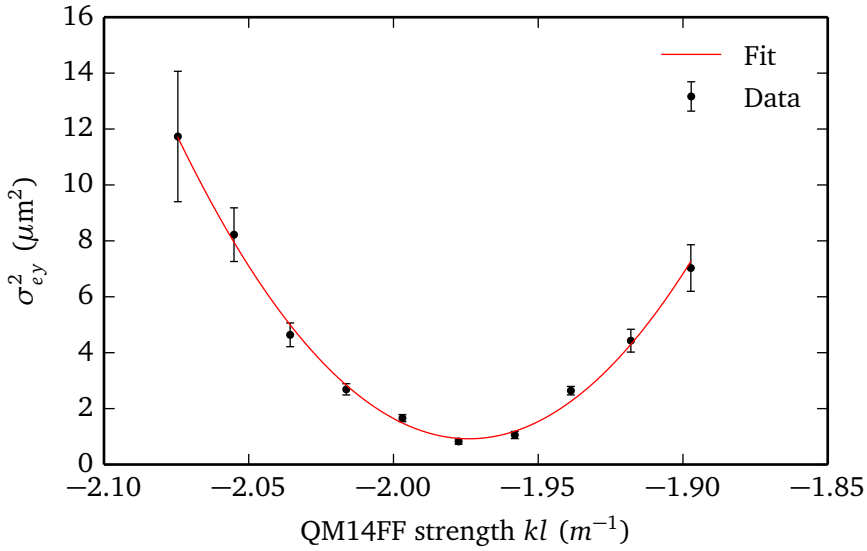


Figure 2.39. The measured vertical beam size squared as a function of effective QM14FF quadrupole strength.

The vertical emittance was extracted using the same method described in section 2.2. From the data and the fit in Fig. 2.39 the emittance was found to be 59.306$\pm$4.153 pm rad which is consistent with the laserwire measurements presented in section 2.2.6. The emittance was measured the following shift using the multiOTR [44] and found to be 23 pm rad however, this was measured after a series of beam tuning routines performed and thus a smaller emittance is expected.

This measured emittance is cross checked with SAD simulations. Using the beam size definition from Eq. 1.16 and assuming at the location of the OTR screen $\varepsilon\beta >> D^2\left(\frac{\Delta p}{p}\right)^2$, the beam size can be approximated by $\sqrt{\beta\varepsilon}$. The beta function is defined by the optics and while the initial Twiss parameters used for the SAD simulation will affect the location of the minimum beta function, the value of the beta function at the minimum should remain constant. Using this minimum value along with the measured emittance, a beam size can be calculated to compare with measurement. With the simulated beta function and the measured emittance, the minimum beam size was expected to be 0.65 $\mu$m which is comparable to the 0.754$\pm$0.034 $\mu$m directly measured using the OTR PSF technique.

### 2.3.7 Comparison between OTR and laserwire

During the laserwire operations, results of the vertical electron beam size measurements were cross-checked using OTR based technique. Vertical electron beam size as a function of the QM14FF quadrupole current was measured first using OTR beam profile monitor and then using laserwire system. Results of the measurement are presented in Fig. 2.40. As one can see, both measurements demonstrate a very good agreement. Bigger errorbars at the tails of the scan for the OTR measurement is due to the vertical beam size extraction method.

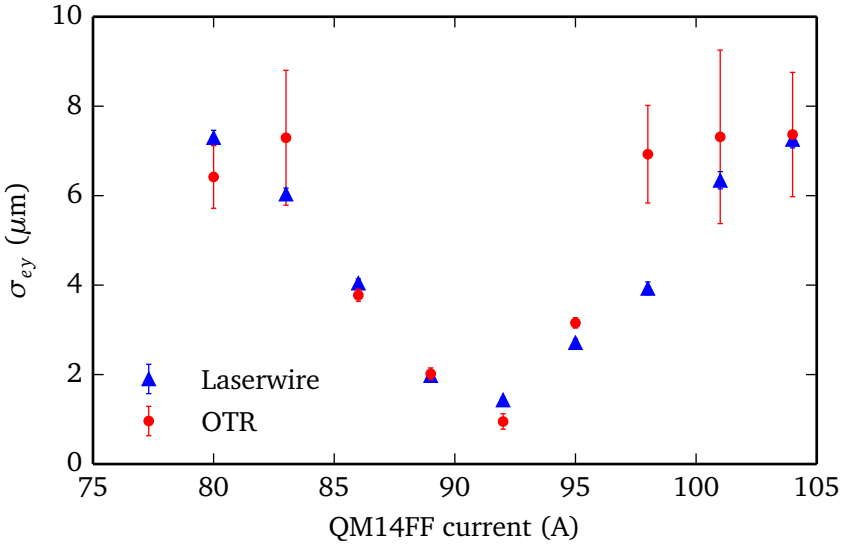


Figure 2.40. Vertical electron beam size as a function of the QM14FF current measured with the laserwire and OTR technique.

### 2.3.8 Aberration effects limiting the OTR monitor resolution

The form of the PSF, and hence the resolution of the OTR monitor, strongly depends on the diffraction and aberration effects of the optical system. These effects lead to broadening of the PSF and, consequently, to a lower resolution. To be able to progress in the research and develop a new optical system with minimized PSF distortion, the aberration contribution needs to be studied and understood.

In order to study such effects a series of measurements with different optical elements were performed. The broadening of the distribution caused by the aberration effects can be easily measured as the distance between peaks in the vertical projection of the OTR image. To study chromatic aberration effects, a several focus-scans (measuring a distance between peaks of the distribution at different longitudinal lens positions) with different optical filters in a wavelength range 480 – 620 nm were performed. The resultant dependencies are presented in Fig. 2.41. These measurements were performed using “Sigma Koki” achromatic doublet lens with a focal length of 120.1 mm and 30 mm diameter. As one can see from the picture, the focus positions are different for different optical filters even for the lens designed to minimize the chromatic aberrations. Therefore for any lens

its position must be carefully adjusted to maximize the resolution of the instrument.

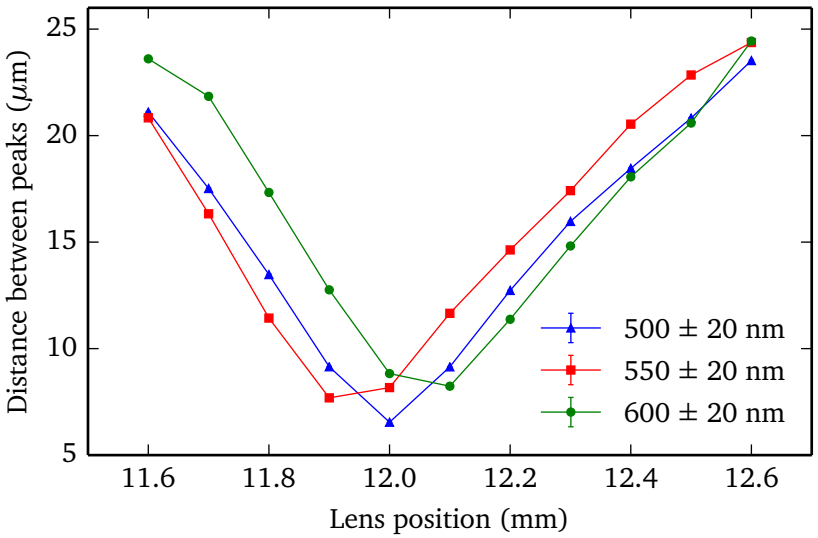


Figure 2.41. Distance between peaks as a function of the lens position for different optical filters. Presented data was taken with the "Sigma Koki" lens ($f$=120 mm).

Another optical effect that degrades the resolution is the diffraction of the OTR tails by the hard aperture of the optical elements. To study this effect, an iris was mounted in front of the lens (see Fig. 2.26). Similar to aberrations, diffraction effect leads to broadening of the distribution hence to worse resolution. In order to estimate the influence of the diffraction on distribution width the distance between peaks as a function of the iris aperture diameter was measured (see Fig. 2.42). It is clear that diffraction effect becomes noticeable at the iris diameter of ∼15 mm. This means that the diameter of the focusing lens can be reduced down to 15 mm, thereby the lens can be manufactured thinner which leads to reduction of the spherical aberrations.

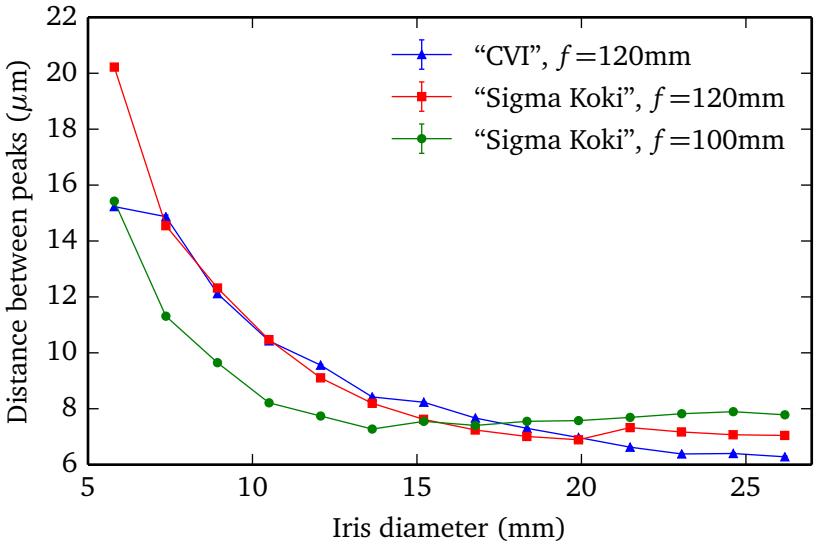


Figure 2.42. Distance between peaks as a function of the iris diameter for different lenses.

Results of the beam size measurements using focusing lenses with different optical properties are presented in Fig. 2.43. As one can see, the measurements performed with the aberration corrected lenses ("CVI" $f$ =120 mm and "Sigma Koki" $f$ = 120 mm) in a good agreement with the simulations while use of simple plano-convex lens ("Sigma Koki" $f$ = 100 mm) results in a bigger measured beam size with bigger errors.

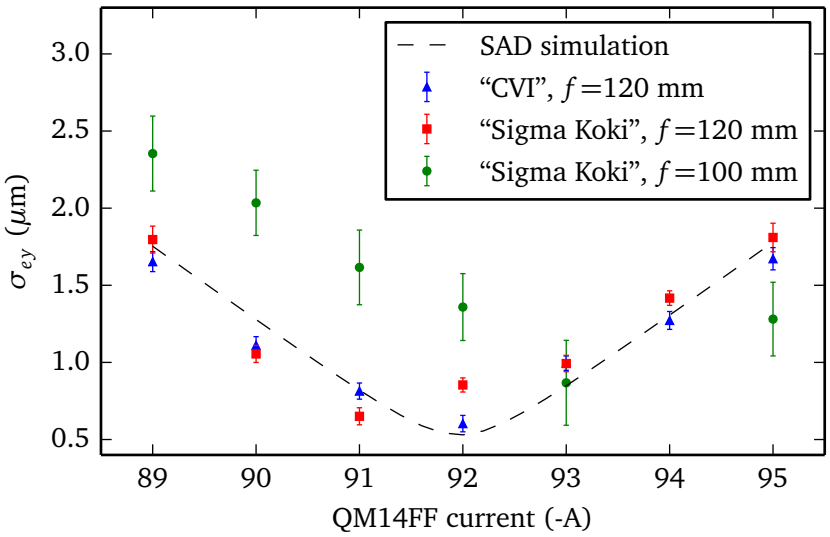


Figure 2.43. Vertical beam size as a function of the QM14FF quadrupole magnet current for different lenses: "CVI Laser Optics" cemented achromat with 120 mm focal length, "Sigma Koki" achromatic doublet with focal length of 100.7 mm, "Sigma Koki" plano-convex lens with 100 mm focal length.

### Test bench to study the chromatic and spherical aberrations

In order to study chromatic and spherical aberration effects more deeply a special test stand was developed. The schematic picture and photograph of the stand are presented in Fig. 2.44, and 2.45 respectively.

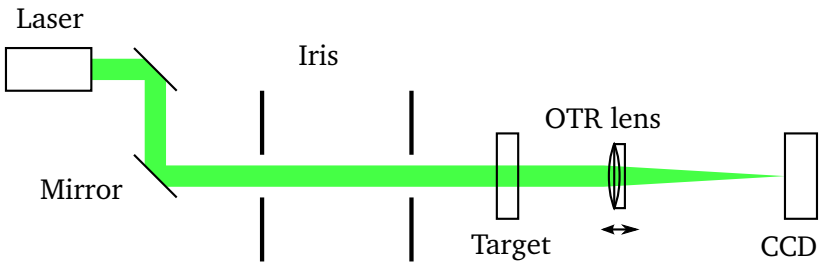


Figure 2.44. Schematic of the test bench.

The whole setup was assembled on an optical table. Three continuous wave (CW) lasers with 532 nm, 400 nm and 632 nm wavelengths were used as sources of light. The lasers were placed on a stage that allows to change the lasers without changing the alignment. Alignment of the laser beam was performed using two aluminum coated mirrors

with diameter of 50 mm and two irises. To imitate the OTR screen a “ThorLabs” R3L3S1P - positive USAF target was used. A lens was mounted on the remotely controlled linear stage. The image of the pattern was detected by the CCD camera and recorded by the camera software. Images were recorded as a function of the lens position. Focusing properties of the lens were measured by analyzing the target images.

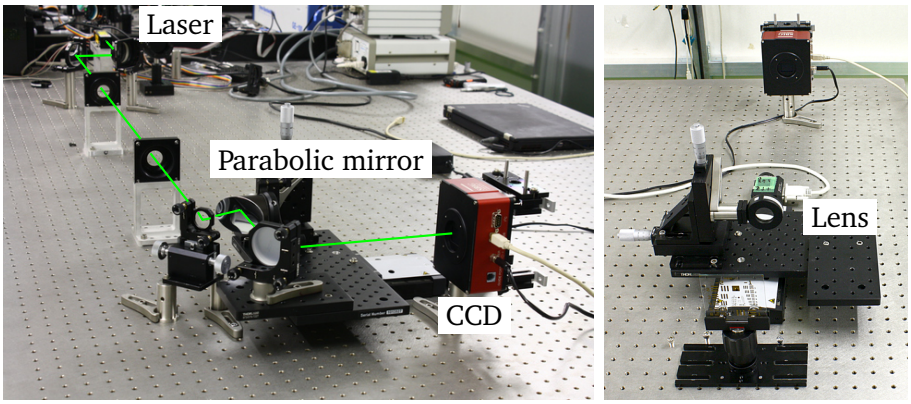


Figure 2.45. Photograph of the test stand setup with parabolic mirror (left) and with lens (right).

One way to reduce chromatic aberrations is to use reflective optics instead of refractive. In order to compare these two approaches the measurements of the focusing properties using both an achromatic lens and an off-axis parabolic mirror have been performed. In Fig. 2.46 and Fig. 2.47, a focused CCD image of the target taken with the parabolic mirror and the lens are presented. Fig. 2.48 represents the vertical projection of the strip edge. As one can see, the image taken with the lens is well focused and has small distortion caused by geometrical aberrations whereas the image taken with the parabolic mirror is focused

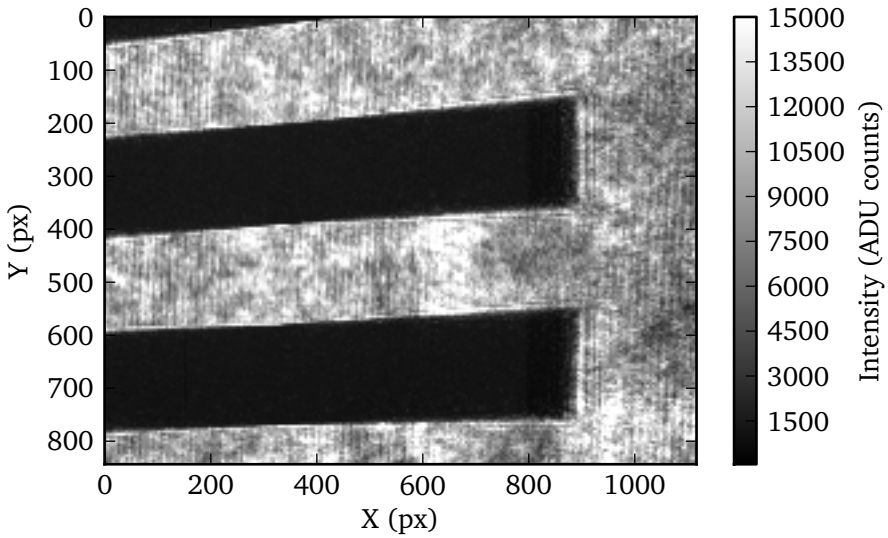


Figure 2.46. CCD image of the target taken with ‘Edmund Optics” 90° off-axis parabolic mirror with parent focal length of 50.8 mm and ø=50.8 mm.

only in a small region and significantly distorted because of the comatic aberration effects. A parabolic mirror has to be perfectly aligned both vertically and horizontally because even small deviations of the beam from the center lead to significant distortion of the image. Moreover, an off-axis parabolic mirror surface does not form an ideal image due to coma-like geometrical aberrations. For that purpose an elliptical mirror might be used. However design and manufacturing of such mirror with an optical quality might be a challenging and expensive task.

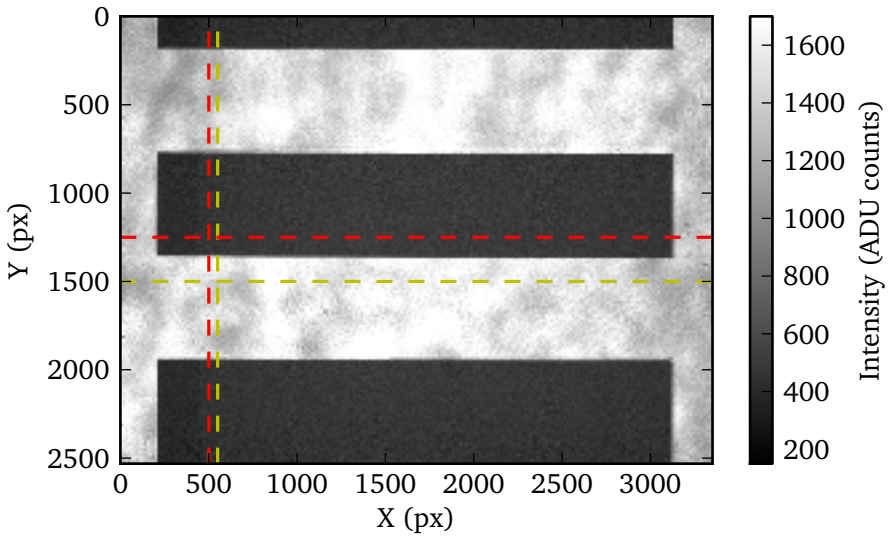


Figure 2.47. CCD image of the target taken with “CVI Laser Optics” lens with focal length of 120 mm.

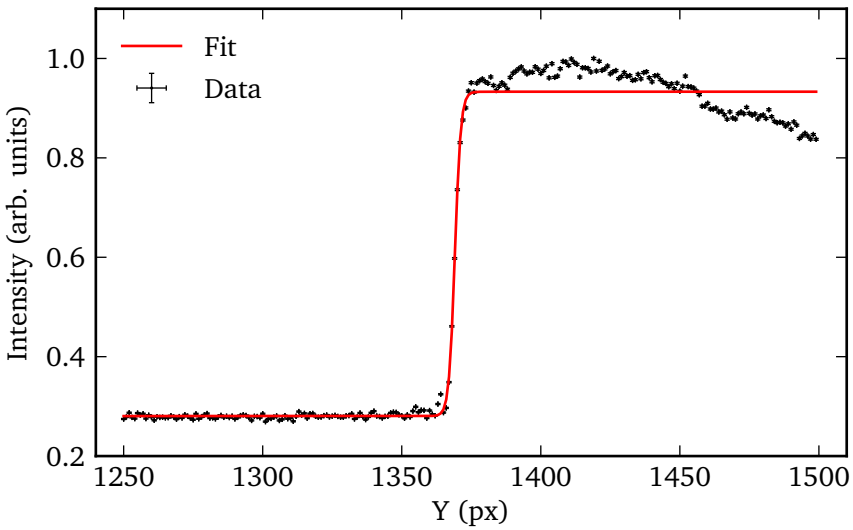


Figure 2.48. Vertical projection of the strip edge along with the fit.

To study the chromatic aberrations of the lenses three lasers with different wavelengths were used. Every lens was gradually moved along the laser beam through the focus. At each lens position the image of the target was recorded by the CCD camera. A part of

the image containing a strip edge was selected (see Fig. 2.47 and 2.48). Then vertical projection of this selected area was fitted using Eq. 2.17. Parameter $a_3$ of the fit function strongly depends on the image contrast and can be used as a measure of the focusing (e.g. if $a_3 = 0$ the image is perfectly focused). The final dependencies of the focusing parameter versus the lens position are presented in Fig. 2.49 – 2.51.

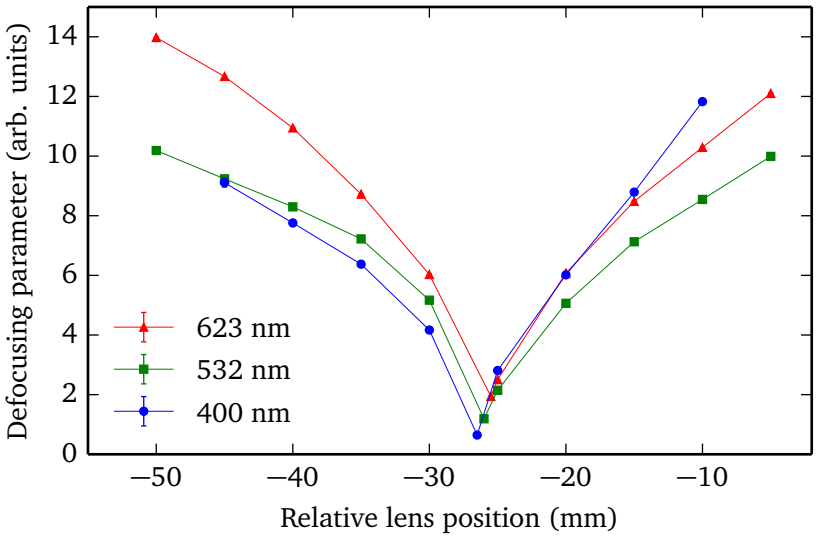


Figure 2.49. Chromatic aberration study for “CVI Laser Optics” cemented achromat with 120 mm focal length.

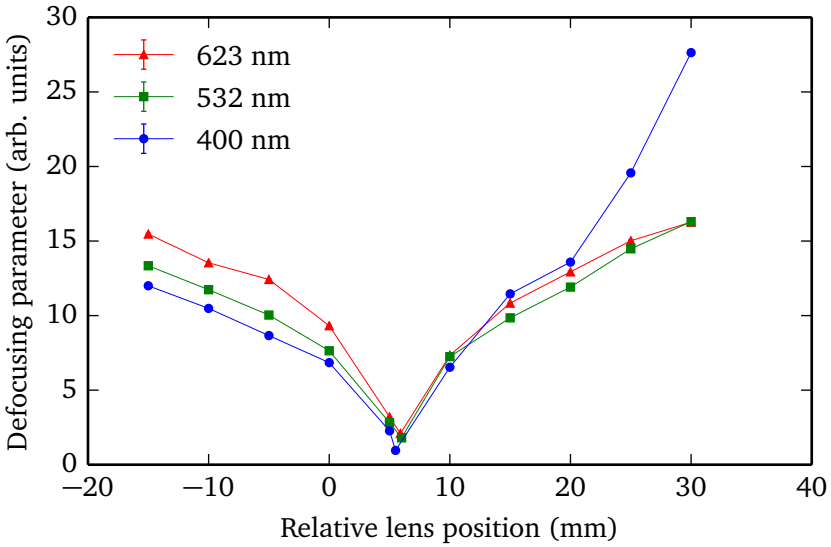


Figure 2.50. Chromatic aberration study for “Sigma Koki” achromatic doublet with focal length of 100.7 mm.

As one can see, achromatic doublets (Fig. 2.49, 2.50) have small chromatic aberrations because the position of the best focus (i.e. the minimal $a_3$ parameter) is nearly the same. While singlet lens shows a strong chromatic aberration (Fig. 2.51) for presented wavelengths. These results demonstrate a good correlation with beam size measurements

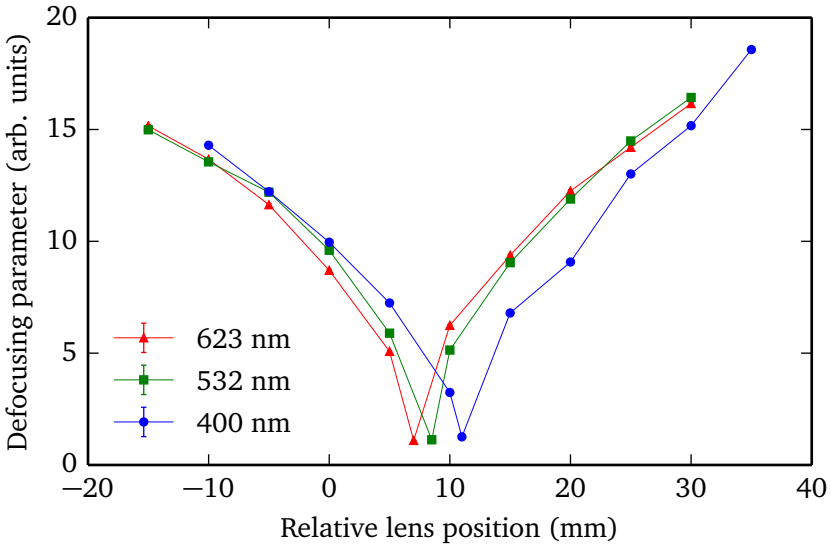


Figure 2.51. Chromatic aberration study for "Sigma Koki" plano-convex lens with 100 mm focal length.

described in the previous section.

## 2.4 Chapter summary

In this chapter the principles of the laserwire technique for transverse diagnostic of the electron beams have been presented. Implementation of these principles has been demonstrated on the example of laserwire beam profile monitor designed for measuring the electron beam size with micrometre resolution at ATF2 in KEK, Japan. Description and principle of operation of the beam profile monitor based on optical transition radiation that was used to cross-check the laserwire results was also presented.

The author has joined the project at its final stage. All the hardware was already created and commissioned.

Author's contribution to the laserwire and OTR project at ATF2 was as following:

- Participating in the operational shifts including ATF2 accelerator tuning, data taking and analysis.
- Tuning the laser system including alignment of the laser beam, systematic $M^2$ and power measurements.
- Improvement of the optical system and experimental setup of both OTR and LW.
- Developing the fit function for vertical projection of the OTR distribution which allowed to reduce the imperfections in the data analysis procedure and prepare a complete set of Python scripts for OTR data analysis.
- Design and commissioning of a special test stand for studying the chromatic aberration effects of the OTR optical system and their effects on the resolution of the

instrument.

- Presentation of the results at International Conferences and Symposia.
- Preparation of graphic material and writing of scientific papers [30, 31, 60] and conference proceedings [55, 56, 59, 72, 73]

The main results of the chapter can be represented as following:

- A high resolution, effectively non-invasive laserwire system capable of measuring high aspect ratio, low emittance electron beams such as that at a future linear electron-positron colliders using visible wavelength laser source has been demonstrated.
- A minimum vertical electron beam size of 1.07 $\pm$ 0.06 (stat.) $\pm$ 0.05 (sys.) $\mu$m was measured with a corresponded horizontal beam size of 119.0 $\pm$ 2.4 (stat.) $\pm$ 0.01 (sys.) $\mu$m using the laserwire.
- A single quadrupole scan was used to measure the vertically projected geometric emittance of 82.56 $\pm$ 3.04 pm rad.
- A high resolution transverse beam profile measurement system based on OTR has been demonstrated.
- A minimum measured vertical electron beam size was found to be 0.754 $\pm$ 0.034 $\mu$m which matches the LW measurements.
- The vertical geometrical emittance extracted from quadrupole scan was found to be 59.306 $\pm$ 4.153 pm rad which is consistent with LW and simulations.
- Vertical electron beam size measurements using two different methods (OTR and laserwire) have demonstrated a very good agreement.

# Chapter 3

# Laserwire for H$^-$ machines

## Principles of the laserwire system for H$^-$ ions

ACCELERATORS for negative hydrogen ions are now widely used mostly as injectors for proton synchrotrons. After preliminary acceleration, H$^-$ ions is converted into protons by stripping off two electrons from the ions. Such injection scheme (also called charge-exchange injection) has a major advantage in comparison with conventional methods. During the injection by charge exchange process the charge is not conserved because of the stripped electrons. Particles produced in this process are not described by Hamiltonian equation and hence there are no restrictions imposed on the storage of protons on orbit by Liouville's theorem [74]. Thereby, protons obtained in the charge exchange process can be injected into the ring repeatedly into the same phase space. Due to a very high power H$^-$ beam, anything installed on the beam might be damaged by it. In order to diagnose the high power beam of H$^-$ particles a non-invasive measurement technique is required. The best candidate for diagnostics system is a laserwire scanner. The basic idea of the laserwire technique for negative hydrogen ions is a similar to the one used for electrons. The difference is in the process of interaction between the laser and the particle beam. In case of electrons it is the Compton scattering and in case of ions it is photo-detachment process. The photo-detachment process can be written as the following reaction:

$$H^- + \gamma \rightarrow e^- + H^0$$

The diagram, showing the basic principle of the laserwire for H$^-$ beam diagnostic is shown in Fig. 3.1. Focused in the interaction region, laser beam collides with the ion beam producing a stream of neutral particles and electrons. Since the binding energy, holding second electron in the H$^-$ ion is very small ($\sim$0.75 eV) even a low energy laser photon can be used for stripping the electron off.

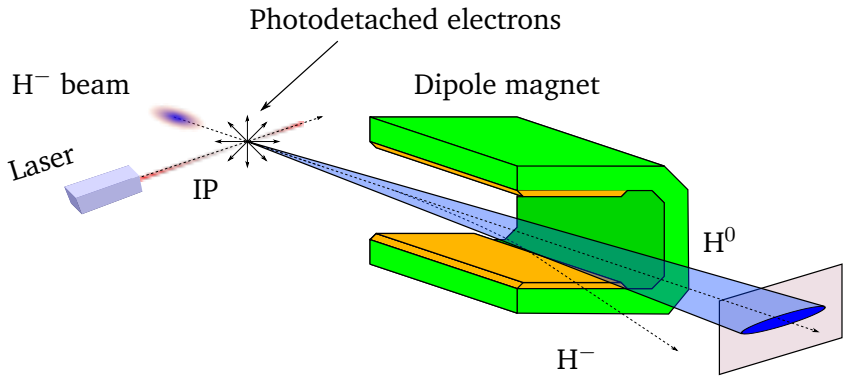


Figure 3.1. Schematic of the laserwire emittance scanner for $H^-$ ions.

The first laserwire diagnostic for measuring the parameters of the $H^-$ beam was built at Los Alamos National Laboratory [75] and then developed and implemented in other facilities such as Spallation Neutron Source (SNS) commissioned at Oak Ridge National Laboratory (ORNL) and Brookhaven National Laboratory for measuring transverse and longitudinal parameters of the $H^-$ beam [76–83]

There are two possibilities of measuring the properties of the ion beam. First is to use photodetached electrons. These electrons can be separated from the main ion beam using a low power dipole magnet and then detected by, for example a Faraday Cup, which measures the amount of charge that has been detached. The number of electrons detached at each position of the laser while it is scanned across the ion beam is proportional to the ion beam density integrated along the path of the laser. This allows an ion beam profile in a plane perpendicular to the direction of laser propagation to be measured. However, since stripped electrons have a very small energy ($\sim$10 eV) it is quite challenging to develop a suitable detection system. Moreover, due to low energy the electron Coulomb repulsion leads to a loss of information about the ion beam angular divergence, and, hence, the beam emittance. Nevertheless, a laserwire utilizing such detection scheme has been developed and successfully demonstrated at SNS [81] to measure the ion beam profile.

Another approach is to detect the neutralized particles. This method allows not only to measure the ion beam profile, but also measure the transverse emittance of the ion beam. At each transverse laser position with respect to the the ion beam the angular distribution of the neutral particle beamlets can be recorded by scanning a detector across the beamlet at a certain distance from the IP while the main beam of negative ions could be deflected using dipole magnet installed upstream the detector. Measuring the profile of the beamlet at each laser position when the laser is scanned across the beam allows to directly measure the transverse phase space distribution and, subsequently, reconstruct the transverse beam emittance as well as profile of the ion beam. Such scheme has been first demonstrated at SNS [82] and recently deployed at LINAC4 in CERN (described in this chapter) and is planned to be used at FETS in Rutherford Appleton Laboratory (see chapter 4).

The number of particles (electrons or neutrals) produced in the laserwire interaction

can be estimated using Eq. 2.1 and Eq. 2.2 by replacing $\sigma_c \rightarrow \Sigma_0$ and $\rho_e(x,y,z,t) \rightarrow \rho_H(x,y,z,t)$, where $\Sigma_0$ is the cross-section of the photodetachment process and $\rho_H(x,y,z,t)$ is the probability distribution function of the H$^-$ ion bunch pulse.

The cross section of the photo-detachment process firstly has been measured in [84] and then calculated and verified by many authors (see for example [85,86]). Total photo-detachment cross-section as a function of wavelength is presented in Fig. 3.2. As one can see the photo-detachment cross-section exceeds $3.5\times10^{-17}$ in wavelengths range of 800–1100 nm. That opens a possibility of use an infra-red laser with a standard wavelength of 1080 nm for the laserwire experiment.

The ion beam size in transverse plane is much smaller than the Rayleigh range of the laser beam. In this case the variation of the laser beam size across the ion beam can be neglected and the vertical or horizontal profile of the ion beam can be deconvolved independently from each other. In this case, assuming that both laser and ion beams have 3D gaussian distribution and the laser pulse is much longer than the ion bunch pulse one can estimate number of photodetached particles using Eq. 2.13.

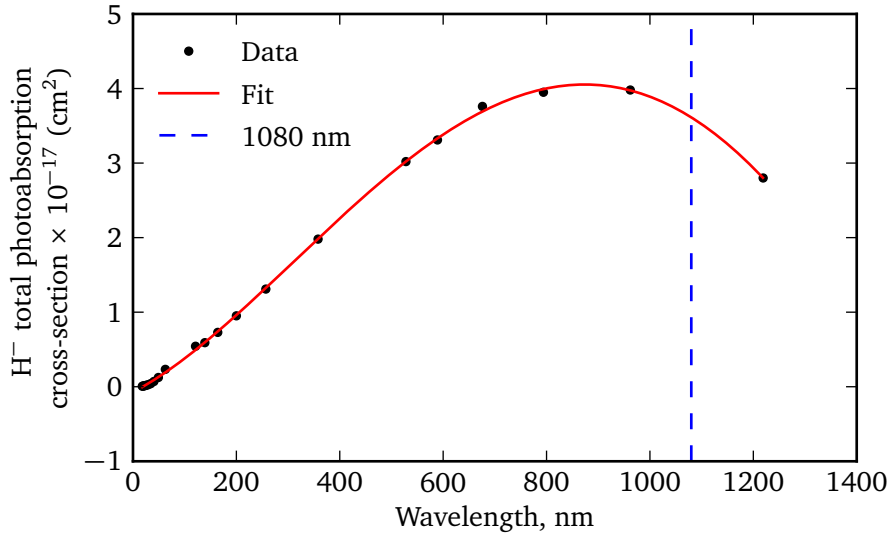


Figure 3.2. Total photo-detachment cross-section (data from Table IV in [85]).

In order to calculate the emittance it is necessary to know a distribution of the neutralized particles at the detector plane. Latest can be calculated by weighting the particles in the initial distribution (which can be obtained from any standard particle tracking code) at the IP with a stripping probability for each particle. The stripping probability or the fraction of the initial H$^-$ ions that are neutralised in the volume where the laser intercepts the ion beam can be derived from the rate of loss of H$^-$ ($n(t)$) due to photo-ionisation which is given by:

$$\frac{\mathrm{d}n}{\mathrm{d}t} = -\Sigma_0(\lambda)\rho\, n, \tag{3.1}$$

here $\Sigma_0(\lambda)$ - photodetachment cross-section, $\rho$ - laser photon flux, $t$ - interaction time of the ion with the laser beam. Integrating the Eq. 3.1 one can obtain the number of H$^-$ ions

$N$ after the interaction with the laser beam over time $t_{int}$ and the photodetachment probability can be calculated as:

$$p_{strip} = \frac{N_0 - N}{N} = 1 - \exp\left(\Sigma_0(E)\rho\, t_{int}\right), \tag{3.2}$$

where $N_0$ is the initial number of ions per pulse.

For the high energy ions there is very considerable relativistic shift of the laser photon energy to higher energies in the frame of reference related to the ion beam. In this case, energy dependent parts in 3.2 must include the photon energy $E_{CM}$ in the ion beam rest frame. The relation between the laser photon energy in the ion beam rest frame and laser photon energy $E_L$ in the lab frame of reference is given by:

$$E_{CM} = \gamma E_L \left(1 - \beta \cos\theta_L\right). \tag{3.3}$$

Here $\theta_L$ is the angle between laser beam and ion beam in the lab frame of reference.

### 3.0.1 Emittance measurement technique for H$^-$ beams

As it was mentioned before, a transverse geometrical emittance of the H$^-$ beam can be measured directly using laserwire. By measuring the profile of the H$^0$ beamlets at the detector one can calculate the divergence of the initial H$^-$ beam at each laser position at the IP. Schematic diagram explaining this method is shown in Fig. 3.3. The divergence of the ion beam $x'$ can be calculated as:

$$x' = \frac{x_1 - x_0}{L}, \tag{3.4}$$

where $x_0$ is the position of the laser with respect to the center of the ion beam, $x_1$ is the position of the detector with respect to center of the ion beam and $L$ is the drift distance between LWIP and the detector.

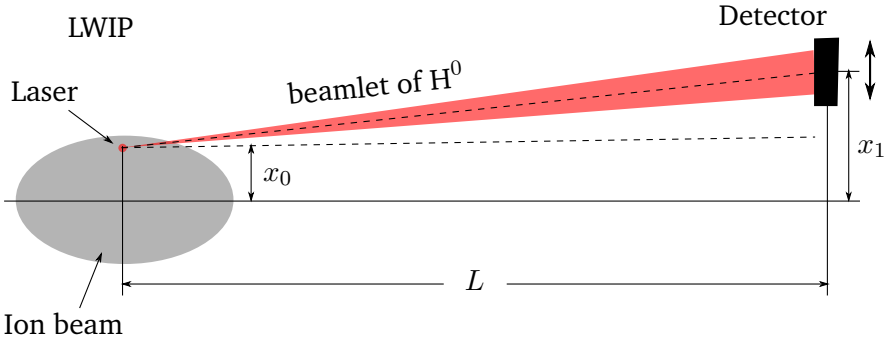


Figure 3.3. Principle of the laserwire emittance measurement. Spatial and angular distribution (phase-space) of the beam can be measured by scanning the laser accros the ion beam and recording the distribution of neutralized particles by scanning the detetor across the beamlet at each laser position. The spatial distribution of the neutralized beamlet measured by the detector can be converted to the angular distribution of the beam (using Eq. 3.4) sampled at a certain laser position.

The transverse geometrical emittance can then be reconstructed using standard approach [10]:

$$\varepsilon_{rms} = \sqrt{< x^2 >< x'^2 > - < xx' >^2}. \tag{3.5}$$

Here $< x^2 >$, $< x'^2 >$ and $< xx' >^2$ are the second moments of the phase space distribution:

$$< x^2 >= \frac{\sum_i \sum_j (x_i - x_c)^2 I(x_i, x'_j)}{I_{total}}, \tag{3.6}$$

$$< x'^2 >= \frac{\sum_i \sum_j \left(x'_j - x'_c\right)^2 I(x_i, x'_j)}{I_{total}}, \tag{3.7}$$

$$< xx' >= \frac{\sum_i \sum_j (x_i - x_c)^2 \left(x'_j - x'_c\right)^2 I(x_i, x'_j)}{I_{total}}. \tag{3.8}$$

Here $I_{total}$ is the total detected signal, $x_c$ and $x'_c$ - centroid of the distribution calculated using the following formulas:

$$I_{total} = \sum_i \sum_j I(x_i, x'_j), \tag{3.9}$$

$$x_c = \frac{\sum_i \sum_j x_i I(x_i, x'_j)}{I_{total}}, \tag{3.10}$$

$$x'_c = \frac{\sum_i \sum_j x'_j I(x_i, x'_j)}{I_{total}}. \tag{3.11}$$

Here $I(x_i, x'_j)$ - integrated and averaged signal from the detector, $x$ corresponds to the laser position and $x'$ corresponds to the divergence.

To propagate errors Eq. 2.23 has been applied to Eq. 3.5.

$$\Delta_{\varepsilon_{rms}} = \frac{1}{2\varepsilon_{rms}} \sqrt{< x'^2 >^2 \Delta^2_{<x^2>} + < x^2 >^2 \Delta^2_{<x'^2>} + 4 < xx' >^2 \Delta^2_{<xx'>}}. \tag{3.12}$$

Uncertainties $\Delta_{<x^2>}$, $\Delta_{<x'^2>}$ and $\Delta_{<xx'>}$ can be calculated by applying Eq. 2.23 to Eqs. 3.6 – 3.11.

## 3.1 Laserwire emittance scanner at CERN LINAC4

The LINAC4 project located at European Organisation for Nuclear Research (CERN) in Geneva, Switzerland was started in 2008 and aims to build a 160 MeV H$^-$ linear accelerator that will replace the existing proton LINAC2 as the injector to the PS-Booster (PSB). Injection of H$^-$ instead of protons into the PSB would reduce the beam losses and

provide more flexible operational conditions. At the end of commissioning the injection beam provided by LINAC4 is expected to double the beam brightness and intensity of the ion beam from the PSB. LINAC4 project is an essential step in the High Luminosity LHC upgrade required to future improvement of the CERN accelerator complex towards higher performance [87–90].

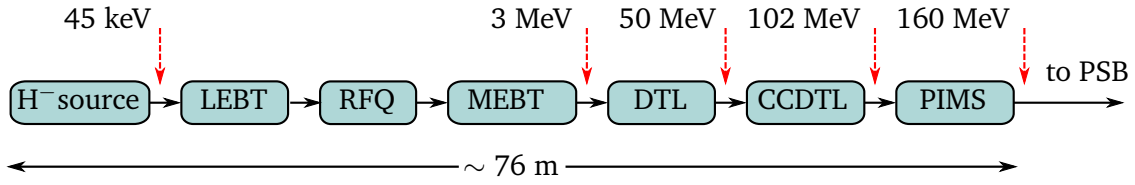


Figure 3.4. LINAC4 block diagram.

The LINAC4 is a normal conducting linac that consists of an ion source [91] that produces 80 mA, 400 $\mu$s beam pulses at the repetition rate of up to 2 Hz, a 352.2 MHz radio frequency quadrupole (RFQ) that accelerates the $H^-$ beam to 3 MeV followed by medium energy beam transport (MEBT), three Alvarez drift tube linac (DTL) tanks accelerating the beam to 50 MeV , a cell-coupled drift tube linac (CCDTL) and finally a Pi-mode structure (PIMS) that accelerate the beam to its final energy of 160 MeV. The LINAC4 basic architecture structure and schematic layout are presented in Fig. 3.4 and Fig. 3.5 respectively. Main parameters of the LINAC4 are presented in table 3.1 (data from [87]).

Table 3.1. General parameters of LINAC4.

| **Parameter** | **Value** | **Units** |
|---|---|---|
| Overall Linac length | 76.33 | m |
| Output energy | 160 | MeV |
| Bunch frequency | 352.2 | MHz |
| Maximum repetition rate | 2 | Hz |
| Beam pulse length | 400 | $\mu$s |
| Max. beam duty cycle | 0.08 | % |
| Average pulse current | 40 | mA |
| Beam transverse emittance | 0.4 | pm mrad |
| Beam power | 5.1 | kW |

To successfully inject the beam from LINAC4 into PSB the transverse emittance at the machine top energy of 160 MeV has to be measured precisely. The conventional slit and grid beam diagnostics is precluded due to the excessive stopping range of a high energy $H^-$ ions at 160 MeV in any possible slit material. Other methods, like the three - profile measurement, can be heavily affected by space charge effects and cannot handle the nominal LINAC4 pulse power. To overcome these problems a non-destructive method

based on laserwire technology has been developed and will be described in the following sections.

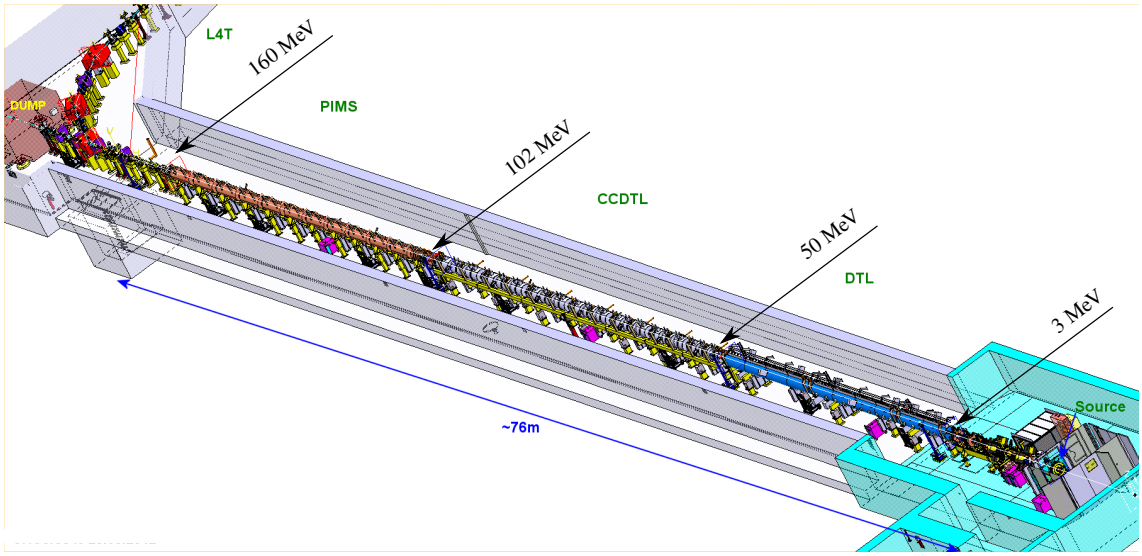


Figure 3.5. Schematic layout of the LINAC4 (picture from [92]).

### 3.1.1 Experimental setup

In order to characterize the H⁻ ion beam at different stages of the LINAC4 commissioning a movable, temporary test bench has been used [93]. After finishing the commissioning of the 3 MeV stage the test bench was placed at the exit of the MEBT section and was used to characterize the ion beam using various diagnostic tools such as beam current transformers, wire scanners, beam position monitors, bunch shape and halo monitors, a slit and grid emittance meter and a spectrometer line [94]. Schematic of the 3 MeV test bench with the main components is shown in Fig. 3.6.

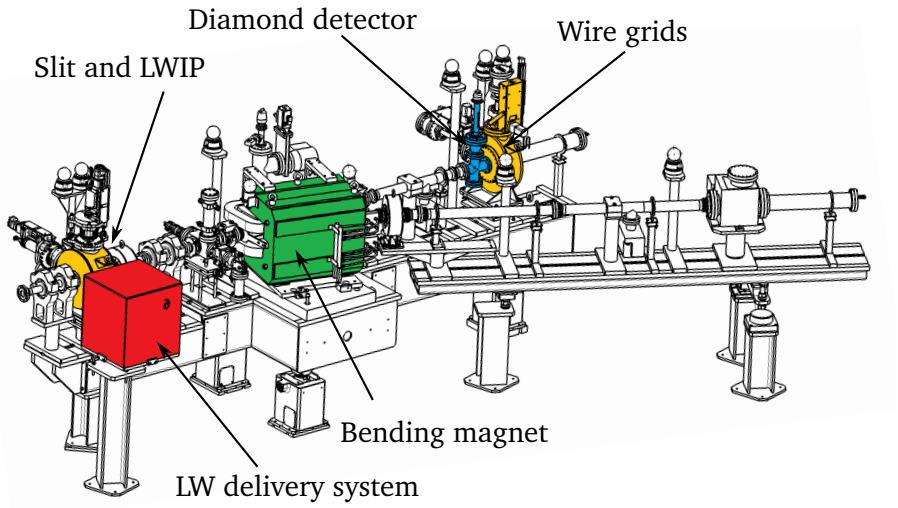


Figure 3.6. Schematic of the CERN LINAC4 3 MeV test bench showing the layout of the main components.

The laserwire interaction is taking place inside the vacuum chamber that was initially designed to accommodate the movable graphite slit which is a part of the slit and grid emittance scanner [95, 96]. The slit is used to select a narrow portion of the initial $H^-$ beam at a certain position. The angular distribution of the selected beamlet is sampled using two wire grids installed downstream the IP, thus the transverse phase space can be measured (see section 3.0.1). The laser entering the vacuum chamber through the vacuum window, specially coated to reduce back reflections in the infra-red range of wavelengths. After the interaction the laser beam is dumped into one of the slit blades. To avoid the damaging of the material, a series of tests has been performed proving that the focused on a graphite plate full power laser beam does not cause any damage and can be operated safely. Such location of the laserwire proved to be very useful because it allows to perform measurements using two different methods and cross-check the results.

A laserwire experiment consists of a remotely controlled pulsed laser mounted in a rack in the accelerator tunnel connected via an optical fibre to a laser delivery system which controls the size and position of the laser beam delivered to the IP. A detection system, installed downstream of a dipole magnet, to record the angular distribution of the neutralized particles from the $H^-$ beam. A photograph showing the laserwire experimental setup is presented in Fig. 3.7.

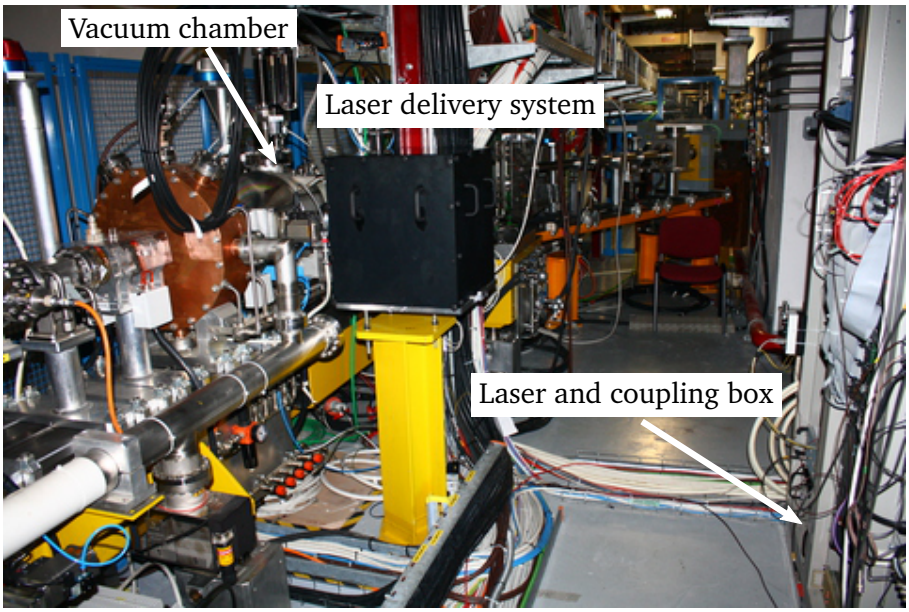


Figure 3.7. Photograph of the experimental setup at 3 MeV.

The laser is a Q-switched, diode pumped, Yb doped fibre Master Oscillator Power Amplifier (MOPA) manufactured by "Manlight S.A.S" (Lannion, France), model: ML-30-PL-R-TKS. The oscillator generates $\sim$ 100 ns pulses (FWHM) at the repetition rate selectable between 30 and 100 kHz, at wavelength of 1080 nm with a pulse peak power of 8.5 kW and maximum output power of 28 W in CW mode. The master oscillator itself operates in free mode and is not capable of being synchronized to an external source. The fibre amplifier is pumped by a diode that can run in CW mode or can be modulated by an external

TTL signal with a repetition rate of up to 5 kHz, enabling the train of amplified pulses to be synchronised to an external source. The schematic and the Interior view of the laser with the arrangement of its main components is presented in Fig. 3.8 and 3.9 respectively.

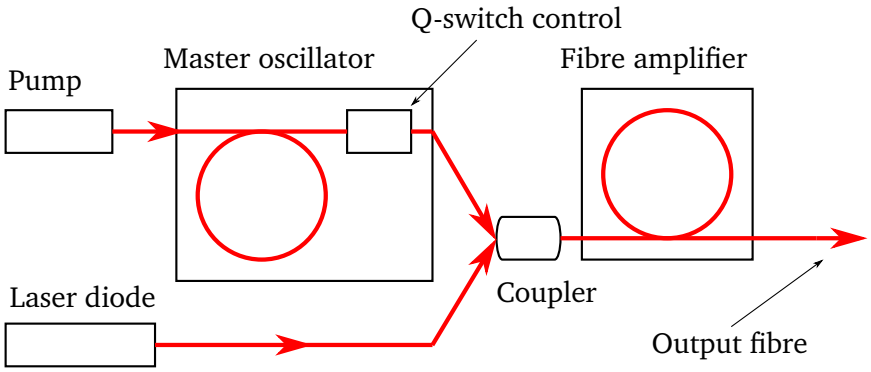


Figure 3.8. Schematic of the laser.

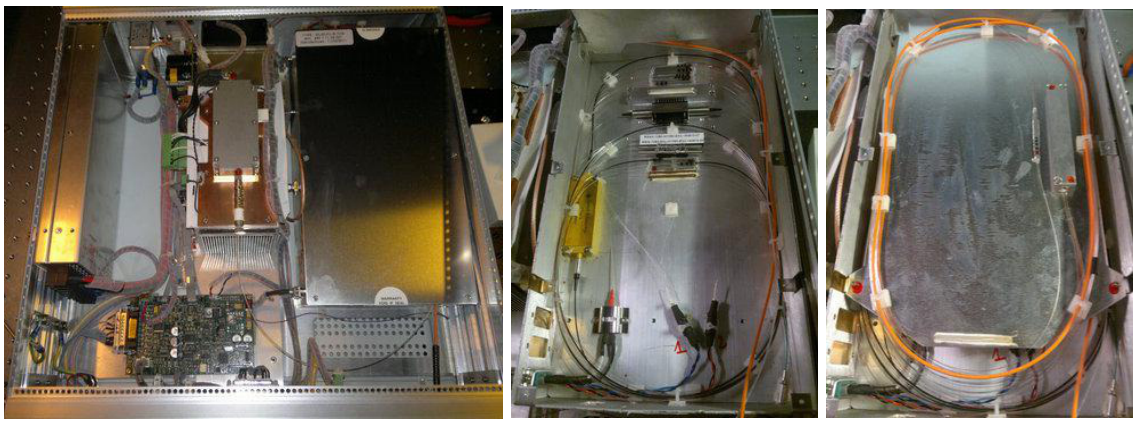

a) b) c)

Figure 3.9. Interior view of the laser: a) - pump diode fibre-coupled to the MOPA system (silver box on the right), b)- master oscillator, c) - power amplifier.

Summary of the laser parameters is presented in Table 3.2 (data according to the laser specification [97]).

To deliver the laser beam to the interaction point a special delivery system has been designed. The schematic and photograph of the system is presented in Fig. 3.11 and Fig. 3.10 respectively. The collimated output from the fibre-laser passes through a safety shutter and collimation lens (L1) and monitored by a photodiode (PD1) and then coupled into a 5 m long optical fibre that transport light to the beam delivery system. A lens with a focal length of 6.25 mm is set to collimate the beam to a waist of 0.5 mm. To optimize the coupling efficiency the input end of the fibre is mounted on a 3D translation stage (S1). From the output of the fibre light passes through a beam expander (BE), that has a range of magnification from 1 to 8X and focusing lens (L2) all mounted on a pair of translation stages (S2) that control the vertical and longitudinal position of the laser beam focus with the micron resolution. A lens with a focal length of 500 mm focuses the laser radius to $\sim$

Table 3.2. Main parameters of the laser system.

| **Parameter** | **Value** | **Units** |
|---|---|---|
| Operation mode | CW or pulsed | – |
| Wavelength | 1080 | nm |
| Pulse repetition rate (external trigger) | 30 - 100 | kHz |
| Average output power (CW pump) | 30 | W |
| Pulse duration | 150 | ns |
| Output power stability | $< 2$ | % |
| External TTL modulation frequency | up to 5 | kHz |

75 $\mu$m at the interaction region, such that only a small slice of $\sim$1 mm ion beam can be neutralized.

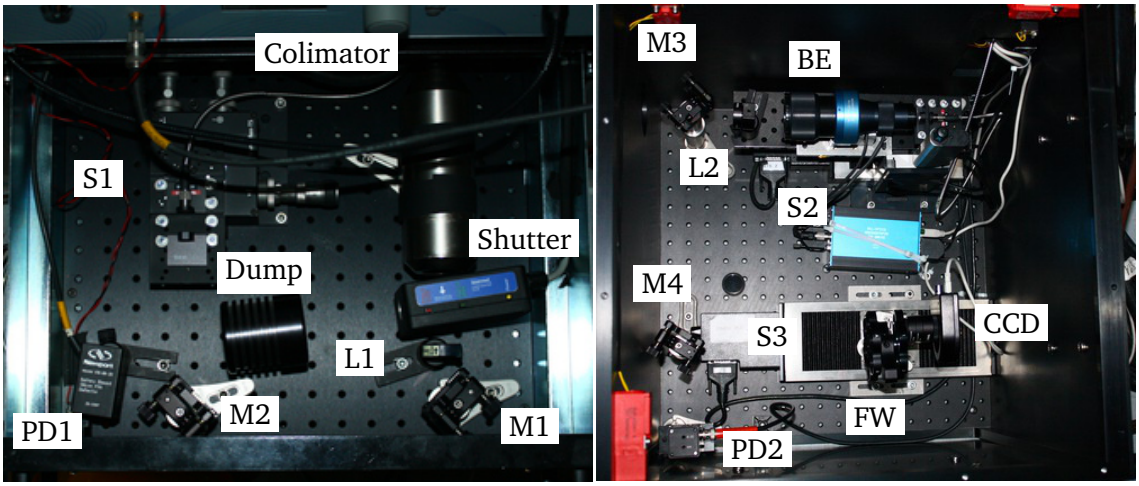


Figure 3.10. Photograph of the laser beam delivery system: coupling box (left) and delivery box (right).

By lowering the vertical stage the laser beam can be delivered via fold back mirrors to the second photodiode (PD2) and a CCD camera. In order to avoid the CCD camera saturation a filter wheel (FW) with a set of attenuators is placed in front of the camera. Both, the camera and the filter wheel can be translated along the laser beam axis using a linear translation stage (S3). This option is useful for measuring of the laser transverse profile at and around the focal length corresponding to the particle interaction region. Both the laser coupling and delivery optics are placed in the interlocked light-tight enclosures for safety reason.

After the interaction with the laser beam, a beamlet of neutral $H^0$ particles passes through the specrometer magnet and then intercepted by the diamond detector that installed approximately 3 m downstream the LWIP. The detector is mounted on a vertical translation stage which allows to move it across the beamline so the spatial profile of the

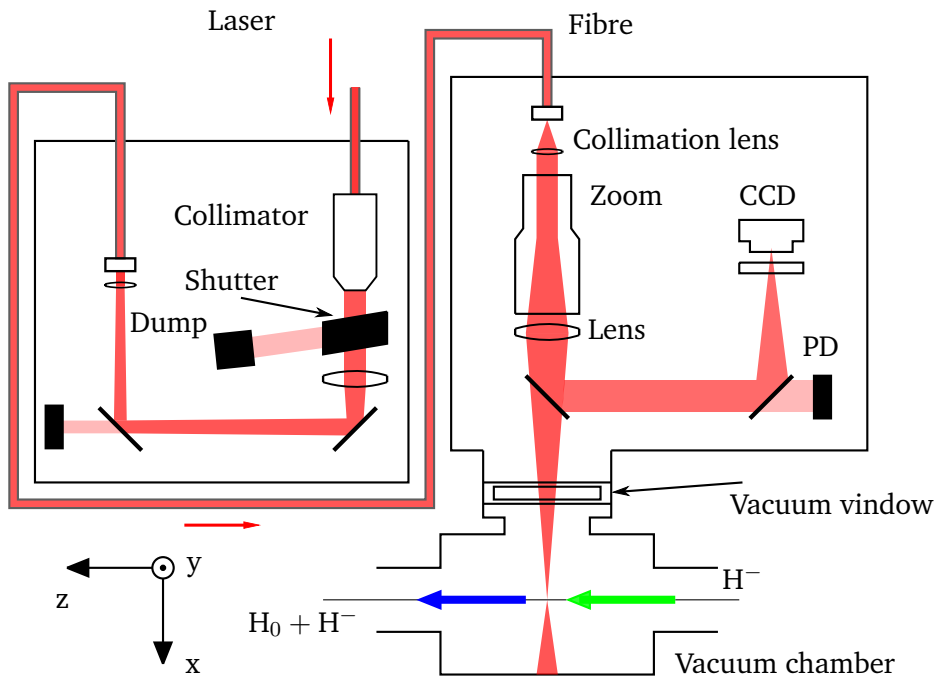


Figure 3.11. Layout of the fibre-laser beam delivery optics.

neutralized beamlet can be determined.

The detector is composed by a polycrystalline diamond bulk produced with chemical vapour deposition (CVD) process and metal electrodes on top and the bottom. The bulk material acts as a solid state ionisation chamber. When the charged or neutral particle passes through the diamond it creates electron-hole pairs along its way. By applying the voltage to the electrodes the electrons and holes move inside the detector creating a signal in the external circuit.

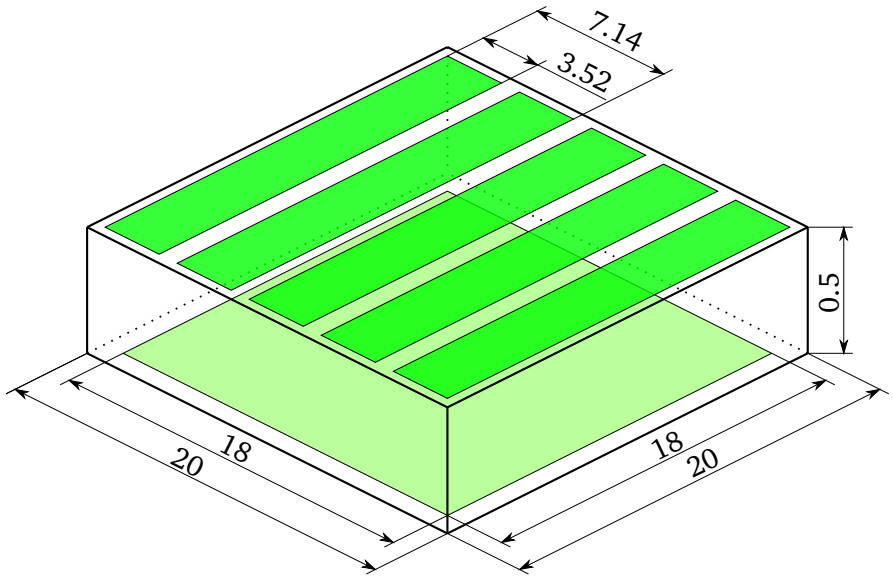


Figure 3.12. Schematic of the diamond detector showing the layout the top and bottom electrodes. All dimensions are presented in millimetres.

The diamond detector has been chosen because of the following advantages in comparison with other detectors [98]:

- good sensitivity (internal gain of the diamond detector is about $10^4$ electrons per $H^0$ )
- response time in the nanosecond range
- radiation hardness ($> 10^{15}$ particles $cm^{-2}$ [99] ).

Table 3.3. Specification of the main components of the laser delivery system.

| **Component** | **Properties** |
|---|---|
| $S_1$ | "Thorlabs" 3-Axis NanoMax Flexure Stage |
| | model MAX 313 D/M |
| $S_2$ | 2D mover, consisting of |
| | "Newport" [100] UTS 50 CC, M-UMR 8.5 |
| | translation stages and LTA - HS actuator |
| $S_3$ | "Newport" UTS 50 CC translation stage |
| BE | Beam expander: "Sill Optics" [101] S6EZM2075/126 |
| $PD_1$, $PD_2$ | Photodiode: "Newport" model 818-BB-20 |
| Dump | Laser beam dump:"Laser 2000" [102] 119-0775 |
| Shutter | "Lasermet" [103] LS - 20 |
| $M_1$, $M_2$, $M_3$ | Mirrors: "Thorlabs" BB1 - EO3P |
| $M_4$ | Window: "Thorlabs" WG 11050 |
| $L_1$ | Lens: "Thorlabs" LA 1172 - C |
| | $f$=400 mm, $\emptyset$ = 25.4 mm |
| $L_2$ | Lens: "Thorlabs" LA 1908 - C |
| | $f$=500 mm, $\emptyset$ = 25.4 mm |
| FW | Filter wheel: "Thorlabs" FW 2A |
| CCD | CCD camera: "Gentec" [104] Beamage |

In the experiment a $20\times20\times0.5$ $mm^3$ "CIVIDEC Instrumentation" [105] polycrystalline diamond detector with five aluminium strips has been used. A schematic and a photograph of the diamond detector is presented in Fig. 3.12 and Fig. 3.13 respectively.

Initially, readout channels of the detector were supplied with charge sensitive amplifiers. However, they were completely saturated because they are made for single-particle detection. After that, linear amplifiers has been installed which were found to give the most reliable signal.

All components of the experimental setup were remotely controlled via NI-PXI with LabView software. The software allows to control the laser system, position of the laser

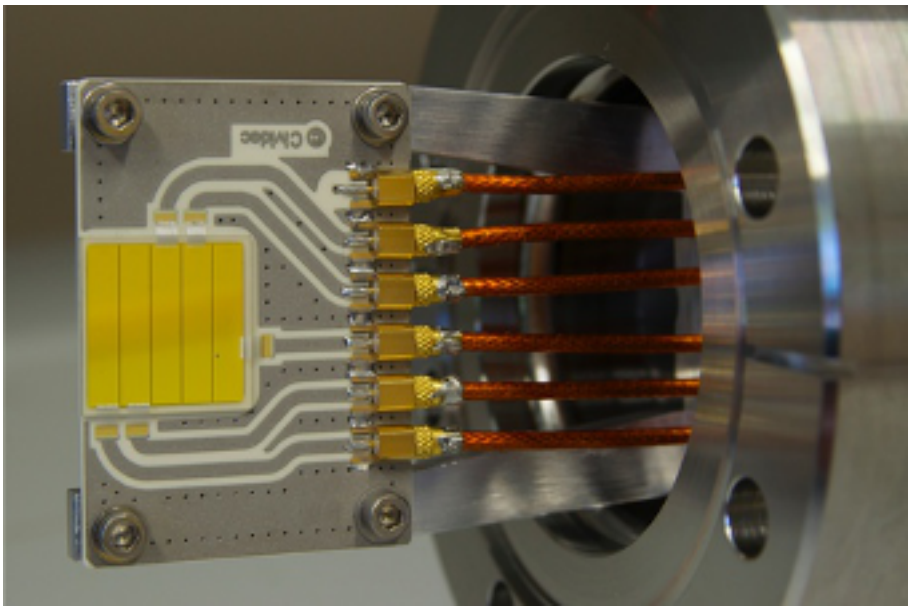

Figure 3.13. Photograph of the diamond detector.

focus and diamond detector. It automates the scans for laserwire position for different detector positions and automates the data acquisition and saves it to the hard drive. Experimental data containing the information about the laser and detector positions, signal from the detector channels and signal from the photodiode was stored in a special LabView format called TDMS. Such type of the files has been chosen because it allows to organize data in a hierarchy of objects, thereby, a big amount of data can be stored inside a single file and then easily accessed for the further analysis.

In order to overlap the laser pulse with LINAC4 macropulse the timing scheme shown in Fig. 3.14 has been used. The source can generate a pulse that anticipates the LINAC4 macropulse. The delay between this pulse and LINAC4 macropulse can be controlled and was set to 500 $\mu$s. The rising edge of the source pulse triggers the 1 ms long laser amplifier pulse which is generated by "Tektronix" AFG3000 function generator independently from the control system. A 500 $\mu$s delay ensures that the LINAC4 macropulse is overlapped with the second half of the laser amplifier pulse where each of the laser pulses already reached the maximum amplification level. Once triggered, the control system generates pulses that are used in combination with the laser output pulses to trigger the data acquisition. Data acquisition trigger window was synchronized to the LINAC4 repetition rate at 0.85 Hz. Data from the diamond detector and photodiodes were acquired using an oscilloscope at 1 GHz rate in short 1 $\mu$s acquisition segments that were synchronized with the 60 kHz pulses generated by the laser. LINAC4 operates at a bunch frequency of 352.2 MHz with a bunch spacing of 2.8 ns which implies each 77 ns laser pulse interacts with approximately 28 ion bunches.

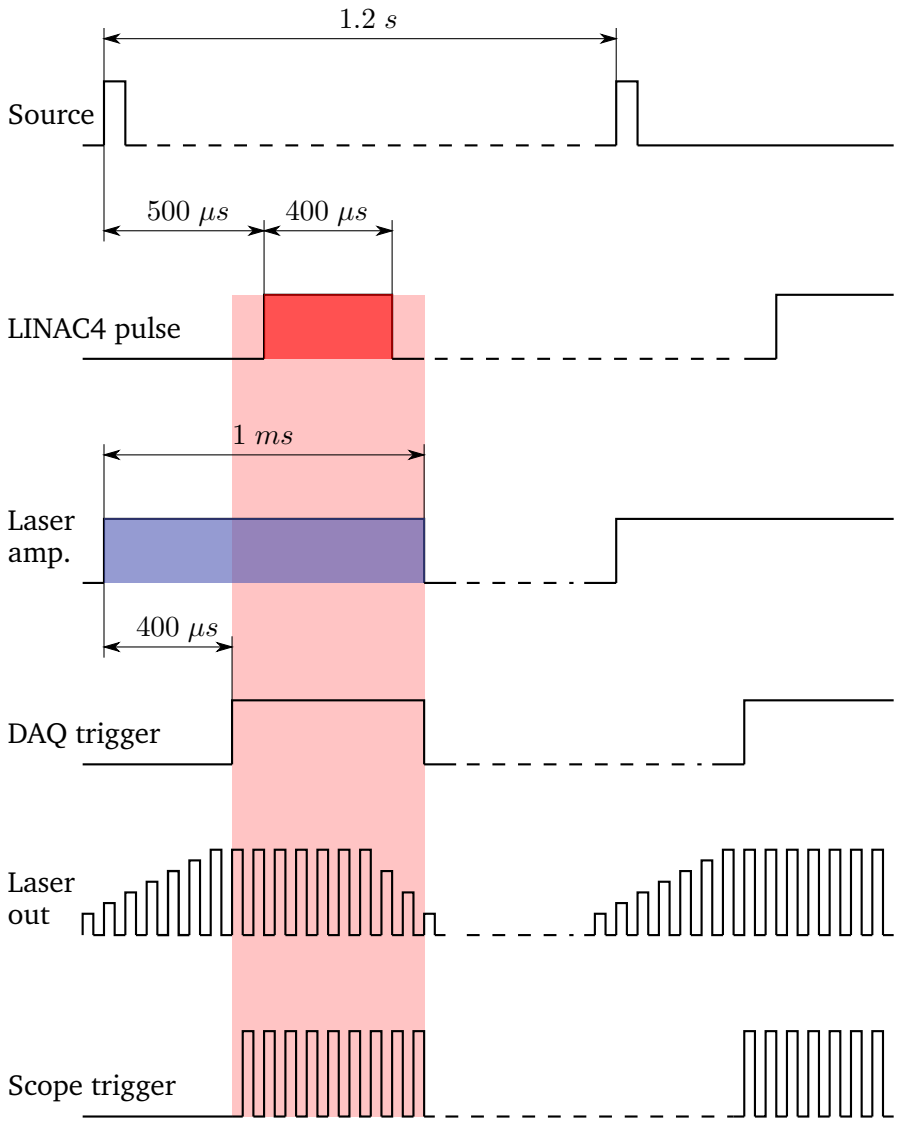


Figure 3.14. The timing diagram for the LINAC4 laserwire operation.

### 3.1.2 Background estimation

Since the laserwire experiment at LINAC4 utilizes the technique in which parameters of the $H^-$ ion beam are measured by measuring parameters of the $H^0$ beamlets produced in the laserwire interaction, every $H^0$ particle arriving to the detector that are not produced by neutralization of the $H^-$ ion by the laser beam is regarded as a potential background of the measurement. According to [106] there are three main sources of the background particles associated with $H^-$ beams. First it is so-called Lorentz stripping in which an extra electron from $H^-$ ion in a relativistic $H^-$ beam can be stripped by the Lorentz transformed magnetic or electric field of a typical beamline magnet. Theory and the estimation of the $H^-$ loss rate of the magnetic field stripping can be found in [107]. Second it is the black body radiation stripping. The beam pipe of an accelerator heated to the room temperature $T = 300$ K can emit approximately $5.47 \times 10^{14}$ thermal photons [106] per cubic meter. In

some cases, the energy of such thermal photon is sufficient to neutralize the H$^-$ particle. The third process contributing to the background production is the H$^-$ stripping by inelastic collisions with residual gas atoms. While the first two effects are negligible in case of LINAC4 beam, the latter is a major source of the background.

The H$^-$ loss rate in case of residual gas stripping is giving by:

$$\frac{\mathrm{d}N}{\mathrm{d}z} = -\sigma_{\text{strip}}\,\rho_{RG}\,N, \tag{3.13}$$

where $N$ is the number of H$^-$ ions, $z$ is the distance along the beamline, $\sigma_{\text{strip}}$ is the cross-section of the residual gas stripping and $\rho_{RG}$ is the density of the residual gas particles.

Integrating equation 3.13, the probability of the striping $p_{\text{strip}}$ by collisions with residual gas can be calculated as:

$$p_{\text{strip}} = 1 - \exp\left(-\sigma_{\text{strip}}\frac{PM}{RT}l\right). \tag{3.14}$$

Here $P$ is the residual gas pressure, $M$ is the ideal gas constant, $T$ is the residual gas temperature and $l$ is the length of the beam pipe. As one can see, the stripping probability primarily depends on the residual gas pressure which mainly consists of hydrogen. Due to this fact, the background level decreases as the distance from the ion source increases.

In order to estimate the background distribution at the detector plane, gas pressures and ion beam dynamics data from the source to the bending magnet were used. Cross-section data from [108, 109] were used to calculate the stripping probability in 2 cm intervals along the beam line and stripped portion was propagated to the detector. The distribution of the integrated background created all along the beamline at the detector for 3 Mev H$^-$ beam is shown in Fig. 3.15.

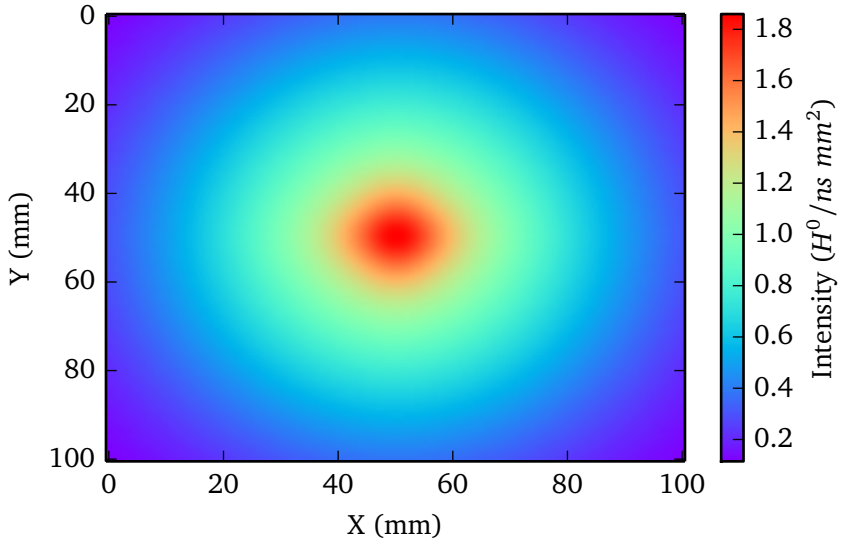


Figure 3.15. Simulation of the background arriving at the detector caused by residual gas stripping.

The simulations of diamond detector signal combined with the background estimations

for the LINAC4 3 MeV setup predict that the signal coming from the laserwire interaction should be approximately 15 times larger than the background level [110] which was confirmed in the experiment.

### 3.1.3 Commissioning of the laserwire system

#### Laser characterization

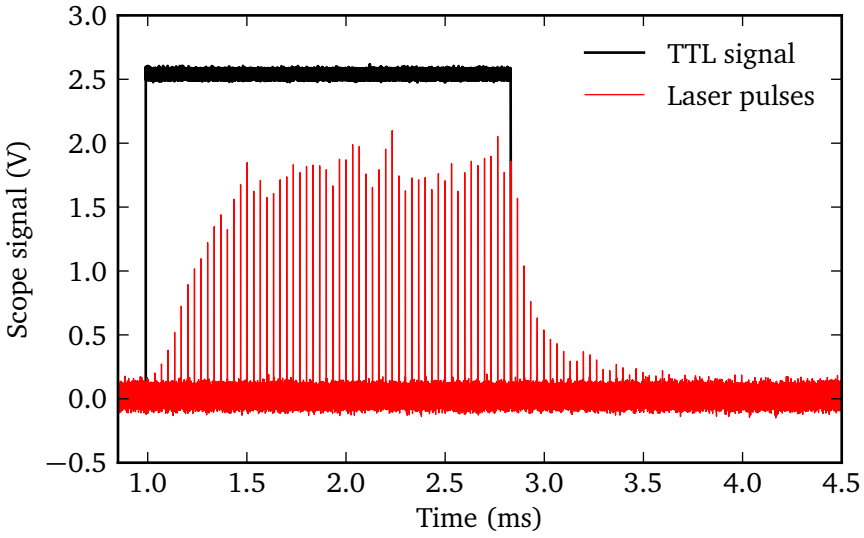


Figure 3.16. The train of the amplified laser pulses.

To characterize the laser beam behaviour a series of measurements have been performed. It includes measurements of the laser power, fibre efficiency and transverse mode quality.

The amplified laser pulses were detected by a fast photodiode with 12.5 Ghz bandwidth, 35 ps raise time and recorded by a 10 Ghz bandwidth oscilloscope at 4 GSample/s rate. The scope trace of the amplified laser pulses and a longitudinal profile of the pulse in a single shot are shown in Fig. 3.16 and 3.17 respectively.

The FWHM of the single pulse was measured as $\sim$ 77 ns (see Fig. 3.17) which approximately 50% shorter than the specified pulse duration of 150 ns. As one can see from Fig. 3.16 the amplification steady state is reached after approximately 200 $\mu$s with the modulation time of 1.5 ms. This figure also shows a visible transient time of about 20% of the pulse duration.

Because the only way to control the output power of the laser is via changing the current passing through the laser diode pump, it is very important to know how the output power changes with changing the laser diode pump current. For that reason, the average power of the laser pulses at 30 kHz for different diode amplification regimes in CW mode (100% duty cycle) has been measured. The resultant curve presented in Fig. 3.18. As one can see, the output power of the laser increases slightly non-linearly with increasing the current flowing through the laser diode pump. Such behaviour is acceptable and demon-

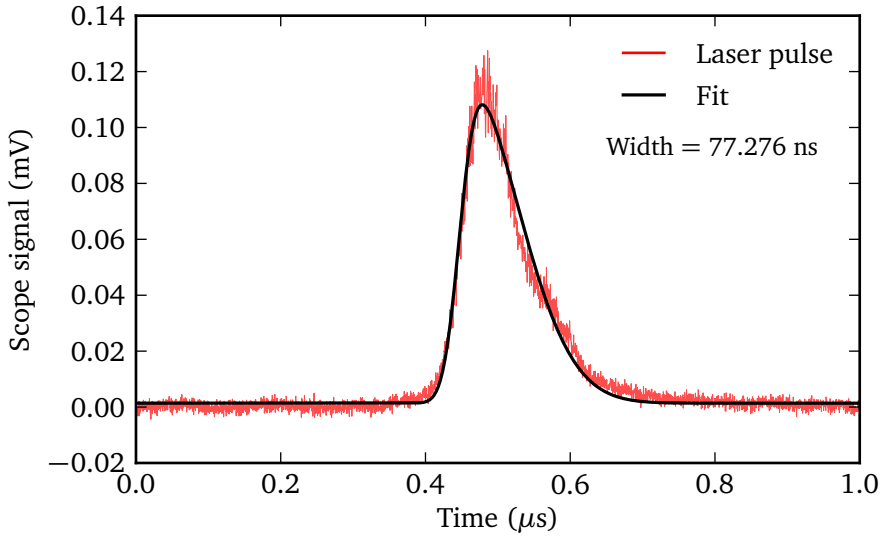


Figure 3.17. Single Laser pulse.

strates normal performance of the laser diode. The maximum average power recorded was ∼ 25 W which is only 10% lower than the nominal maximum average power of 28 W.

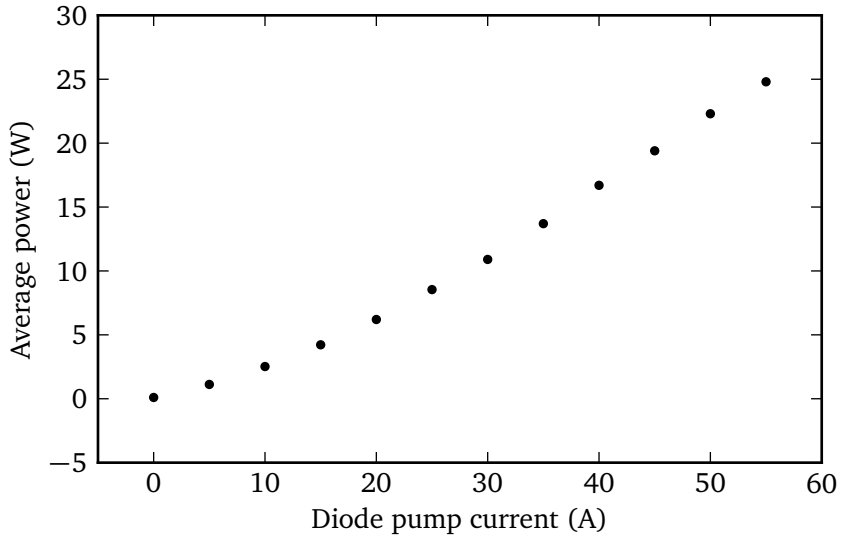


Figure 3.18. Average power as a function of the diode pump current measured at 30 kHz in a CW mode.

The output power can also be controlled by changing the percentage of one period in which a signal, provided by an external trigger, is active (duty cycle). The average power as a function of the duty cycle presented in Fig. 3.19.

From these measurements one can clearly see that the output power changes linearly with variation of the duty cycle of the external trigger. These graphs were used as a calibration curves to choose a correct laser diode pump current and duty cycle of the external trigger in order to send a correct amount of energy to the delivery system and avoid its damage.

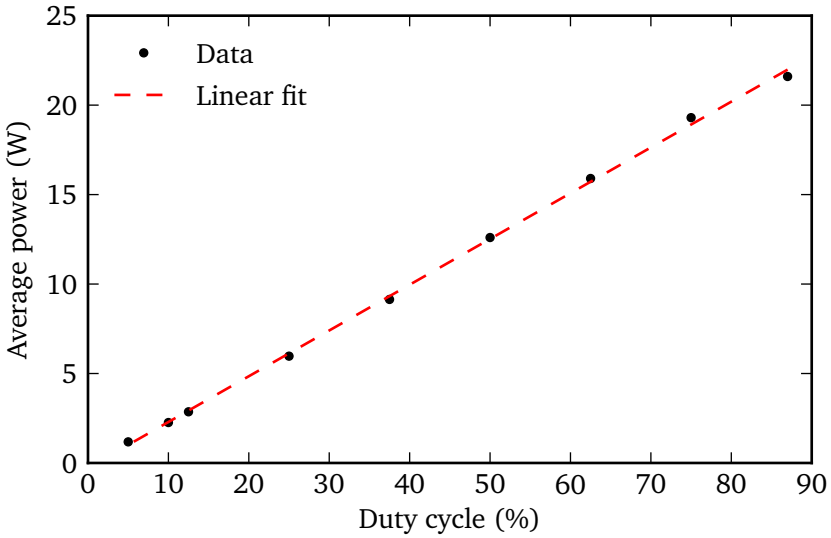


Figure 3.19. Average power as a function of the duty cycle measured at 30 kHz with 55 A amplification.

To deliver the laser beam to the LWIP a 5 m long, large mode area (LMA) double clad optical fibre manufactured by "Nufern" was used. This fibre is based on 20 $\mu$m diameter core and 130 $\mu$m diameter clad size with a low numerical aperture NA=0.08 (equivalent $M^2 = 2.35$). The light from the output end of the main laser fibre was coupled into the delivery fibre using "Thorlabs" fibre coupling system which allows to manipulate position of the fibre end with nanometre resolution. In order to achieve a high coupling efficiency and avoid damaging both facets of the fibre has been manually polished with a high quality. A photograph of the polished fibre end is presented in Fig. 3.20.

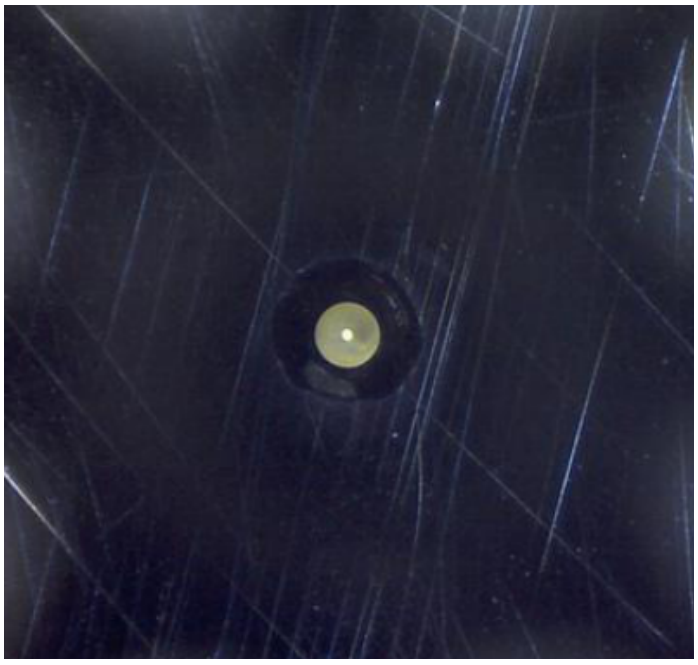

Figure 3.20. photograph of the fibre end

Two main measurements have been performed on the laser beam at the output of the delivery fibre: coupling efficiency (the efficiency of optical power transfer between two fibres) and transverse mode quality. The coupling efficiency has been calculated as the ratio between average power at the output and input ends of the fibre . The coupling efficiency as a function of the laser diode current at 1% duty cycle and 30 kHz repetition rate is presented in Fig. 3.21. As one can see from the graph, the fibre efficiency slightly decreasing from $\sim$ 70% to $\sim$ 65% with increasing the laser diode pump current from 0 A to 55 A. This can be explained by imperfections of the fibre end polishing and by the fact that the fibre efficiency depends on the laser intensity profile. The latter slightly changes with variation of the laser energy.

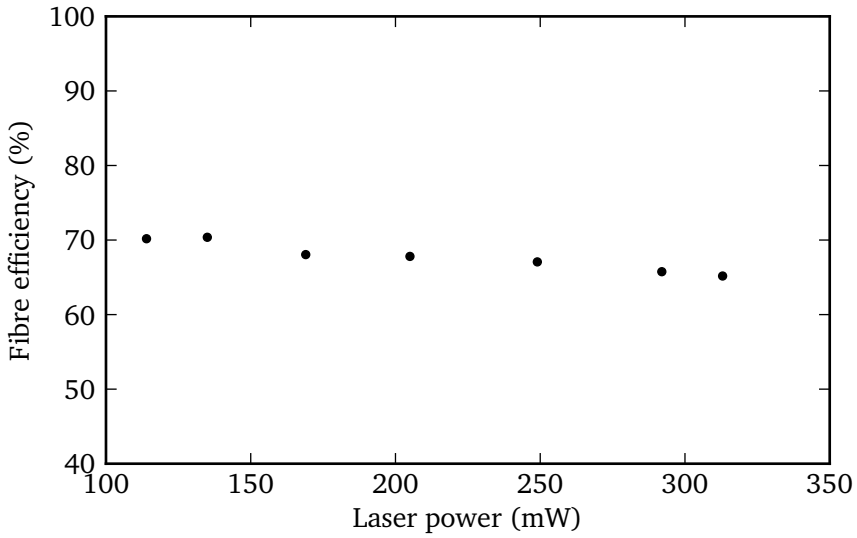


Figure 3.21. Measured fibre efficiency as a function of the average laser power.

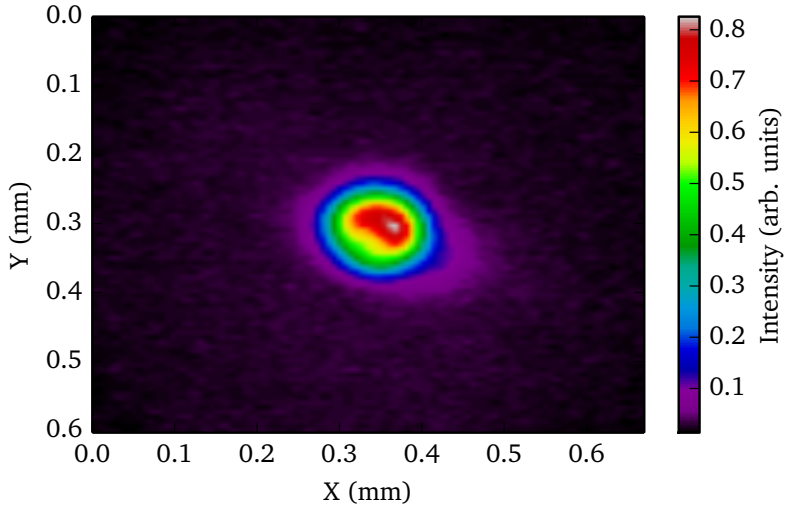


Figure 3.22. Picture of the focused laser spot.

To measure the transverse mode quality, the same technique as described in section 2.2.6 was used. The laser beam from the output end of the delivery fibre was focused

by a plano-convex lens with a focal length of 500 mm. Transverse profiles at intervals of 1 mm in longitudinal position of the laser beam were recorded dy “Gentec Beamage” CCD camera. An example of a transverse intensity profile of the laser beam at the focal plane of the lens is presented in Fig. 3.22. As one can see, the shape of the laser intensity profile has a form very close to a Gaussian profile. A vertical and horizontal laser beam sizes were extracted from the intensity profiles using software provided with the CCD camera. The laser beam sizes as a function of the CCD camera position were fitted with Eq. 2.11 and the $M^2$ parameter was extracted from the fit. The $4\sigma$ laser beam sizes as a function of CCD position is presented in Fig. 3.23. The measured value of the laser mode quality factor was found to be $2.272 \pm 0.013$ in the horizontal direction and $2.002 \pm 0.02$ in vertical direction.

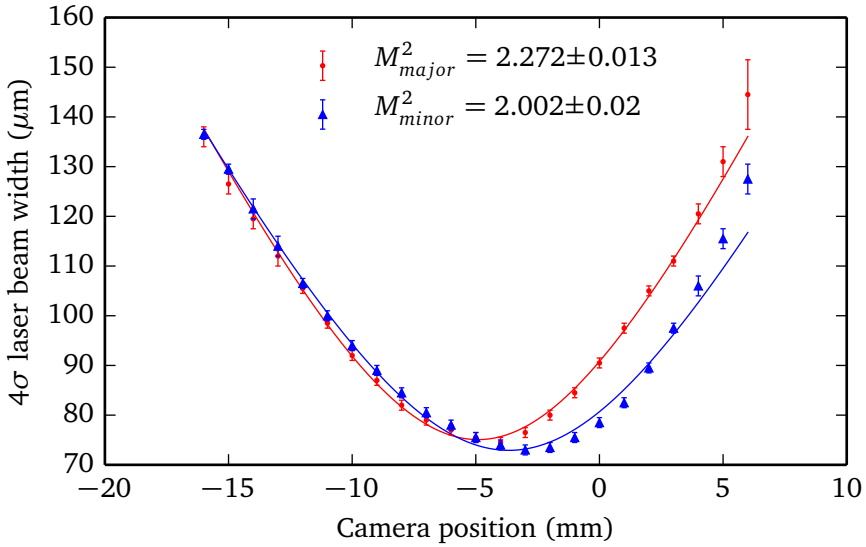


Figure 3.23. Laser propagation measured in both axes.

**Detector response**

In order to understand the diamond detector response several measurements with the diamond detector has been performed. The diamond detector was moved to the center of the vacuum pipe and the laser focus position has been set to the center of the ion beam at LWIP in order to produce the maximum number of neutralized particles.

First, the diamond detector signal as a function of the applied to the detector electrodes voltage has been measured. The voltage was varied from 50 V to 600 V with a step of 50 V and the signal from the diamond detector for each voltage has been recorded. Result of the measurement is presented in Fig. 3.24 . As one can see, the detector response to the variation of the applied voltage has a so-called sigmoid shape which is usual for such type of the detector. During the operation, the best signal was found when the diamond detector was biased at 500 V.

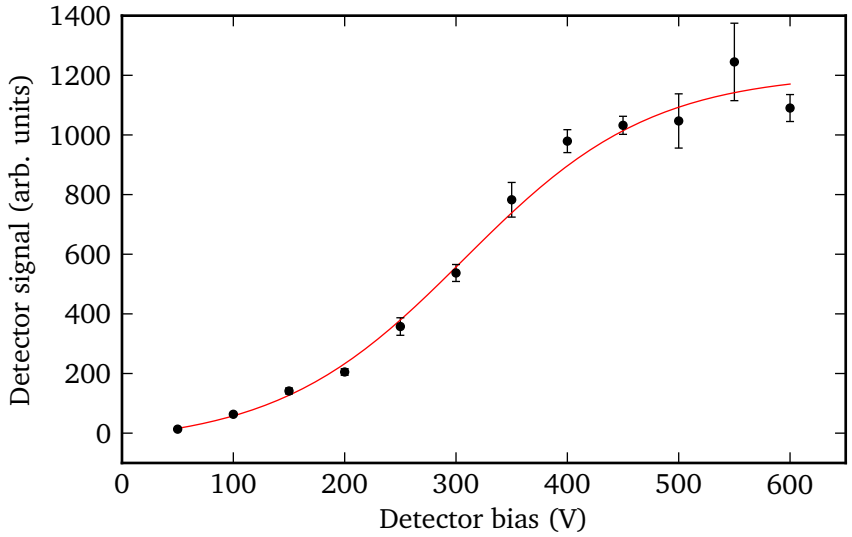


Figure 3.24. Response of the diamond detector at different biases.

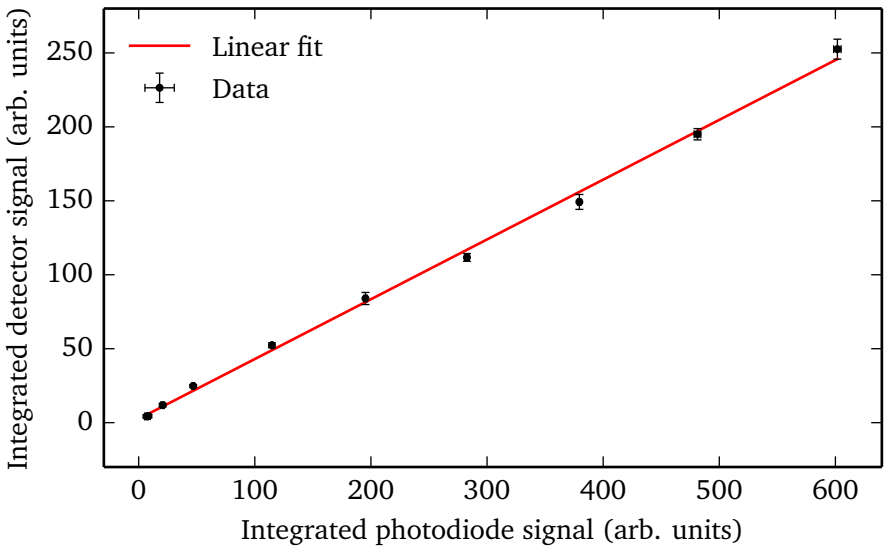


Figure 3.25. Variation of the diamond detector signal with laser energy.

Second measurement was performed in order to understand the linearity of the diamond detector signal with variation of the laser beam energy. With the diamond detector and laser focus centred with respect to the ion beam, the signal from the detector was recorded when the energy of the laser beam was varied. Laser beam energy was varied by changing the current applied to the laser diode pump (see section 3.1.1) from 0.5 A to 35 A with a variable step. Result of the measurement is presented in Fig. 3.25. As one can see the data show very good linear dependence for smaller laser diode currents and slightly greater degree of variation for higher current. During the laserwire measurements laser diode current has been set to low value where diamond detector is linear over the small variation of the laser beam energy.

### 3.1.4 Results of the beam profile and emittance measurements at 3 MeV

After establishing a detectable collision between the laser beam and the ion beam the laserwire station was ready to perform measurements. During the operation at the 3 MeV stage of the LINAC4 two parameters of the ion beam were measured – beam vertical profile and vertical transversal phase-space distribution [111].

To measure the vertical profile, the diamond detector was moved vertically in such a way that the center of the detector coincided with the center of the ion beam. Initially, in order to define scan borders a rough vertical laserwire scan with a big scan step size was performed. After that, a vertical laserwire scan with the fine scan step of 0.25 mm was performed. At each laser focus position the measurements were repeated three times to reduce the statistical error. An example of the diamond detector signal acquired in 30 oscilloscope segments during one LINAC4 macropulse is shown in Fig. 3.26. Figure 3.27 shows the train of 60 kHz laser pulses, recorded by the photodiode before the fibre coupling. Corresponding peaks in the diamond detector signal present only when the laser is powered. The height of the peaks is modulated by the ion beam current which varies along the macropulse. Different pedestal level for each peak in the detector signal is due to neutral particles coming from the upstream residual gas background interactions. In order to retrieve and analyse the acquired data a special Python based software has been developed. To retrieve the profile of the ion beam from the laserwire scan, the diamond detector signal was integrated only over the segments containing peaks from laserwire interaction.

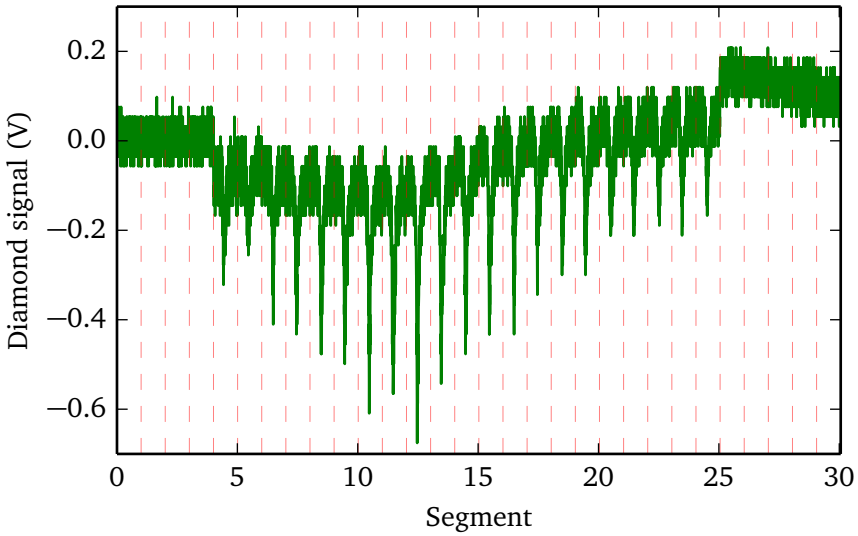


Figure 3.26. Example of the diamond detector signal (red dashed lines represent borders of the acquisition segments).

A zoomed region for one segment around the diamond signal and corresponding laser pulse is shown in Fig. 3.29 and Fig. 3.28 respectively. For each chosen segment a following integration procedure has been performed. First, in order to remove a high frequency noise a smoothing window filter has been applied to the diamond signal. The filter pro-

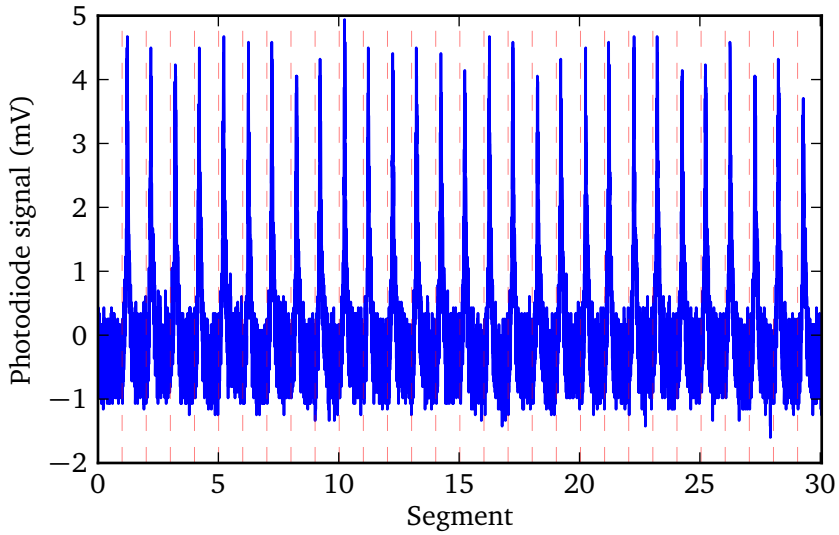


Figure 3.27. Example of the laser signal recorded with PD1 photodiode.

duces a discrete linear convolution of the signal with the array of ones with the length equals to the filter width (in presented case width = 10 samples). The discrete convolution operation for any arbitrary discrete functions $f$ and $g$ is defined as [112]:

$$(f \circ g)[n] = \sum_m f[m]g[n-m]. \tag{3.15}$$

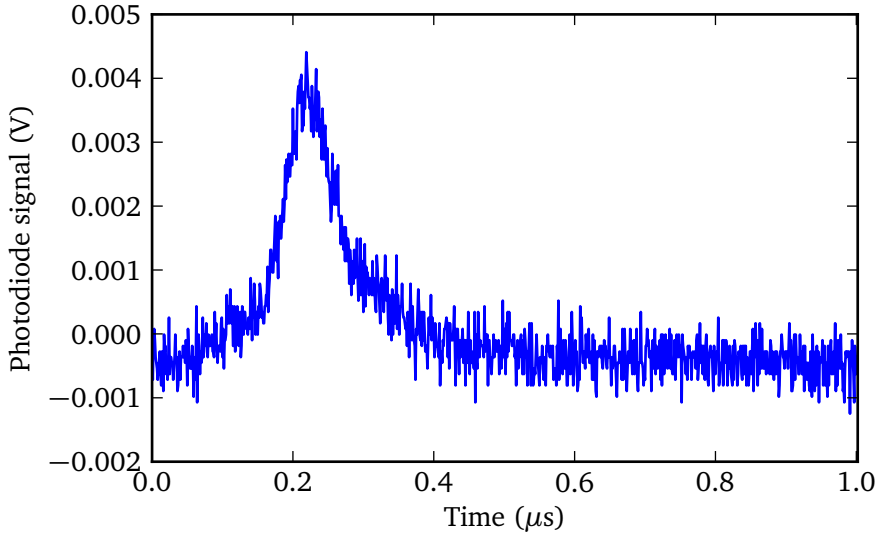


Figure 3.28. A zoomed region from Fig. 3.27.

After that, a linear fit to the residual gas background pedestal (red line in Fig. 3.29) was performed for each segment, and subtracted from the diamond signal. To perform the fit data points from the tails of the signal have been used (first and last 200 points). Then, the signal was integrated over the window containing the peak. Such analysis was performed for every laser position with respect to the ion beam centre.

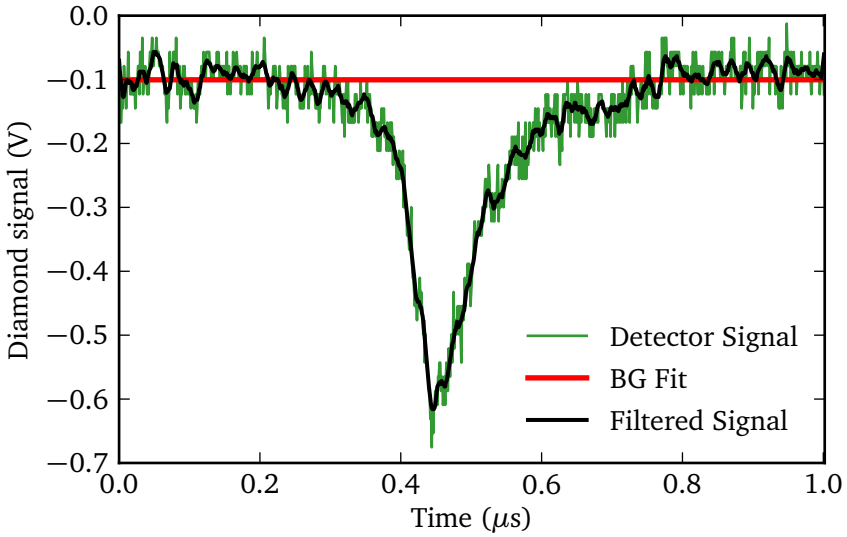


Figure 3.29. A zoomed region from Fig. 3.26.

The vertical laserwire scan that was analysed using described above method is presented in Fig. 3.30. As one can see, obtained distribution has a shape similar to a Gaussian but with broader tails. The measured data were fitted using Gaussian and Cauchy-Lorentz [113] models and the width of the distribution was found to be around 1 mm.

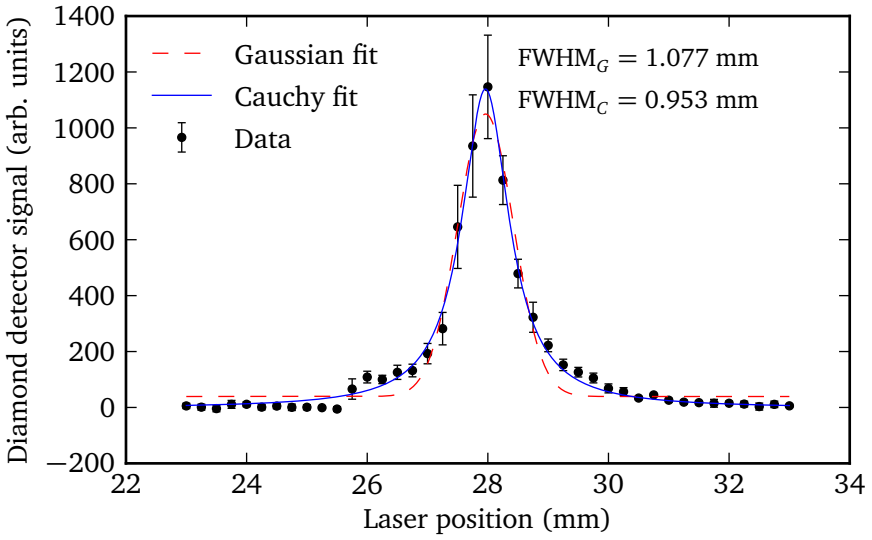


Figure 3.30. An example of the vertical laserwire scan.

In order to measure vertical transverse emittance the following technique has been used. The laser was scanned vertically across the ion beam with variable step size (0.5 mm in the tails and 0.25 mm around the peak) in order to accurately sample the shape of the distribution. At each laser position, the diamond detector was scanned across the beamlet of neutral particles with step of 1.81 mm. Each detector scan corresponding to a certain laser position (with the profile shape similar to Fig. 3.30) was stored in separate data file. Such technique allows to directly sample the phase space as described in section 3. The

data from these files then were analysed using the same analysis method as described above. The integrated and averaged signal then was used to plot the phase space distribution. Measured phase-space distribution for 3 MeV setup is presented in Fig. 3.31.

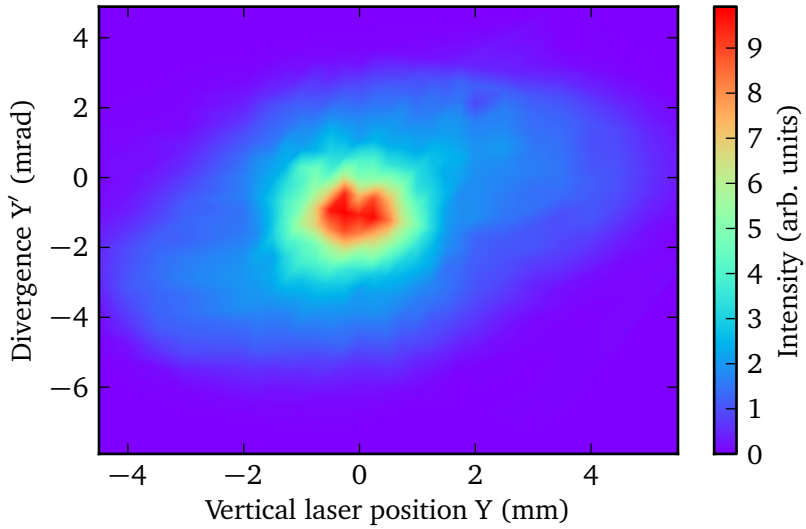


Figure 3.31. Vertical transverse phase space of the 3 MeV H⁻ beam measured by the laserwire technique.

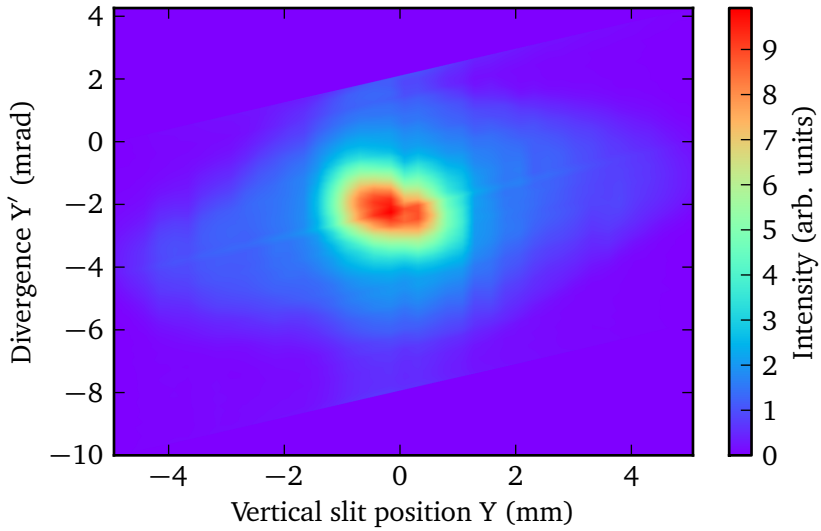


Figure 3.32. Vertical transverse phase space of the 3 MeV H⁻ beam measured by the conventional slit and grid method.

The laserwire results were verified with the independent measurements from conventional slit and grid emittance meter. The slit, installed at the same point as the LWIP was scanned across the ion beam in vertical direction. At each vertical position, well defined with respect to the ion beam center, the slit selects a narrow slice of the ion beam. The distribution of the particles transmitted through the slit was measured after approximately 3 m drift space by two wire grids [96]. Same as in case of laserwire, by scanning the

slit vertically across the ion beam and measuring the profiles of particle beamlets passed through the slit the whole phase space was reconstructed. The phase-space distribution measured by slit and grid is presented in Fig. 3.32.

As one can see from the pictures, despite the lower spatial resolution of the laserwire data in this first test, the phase-space shape and orientation in both pictures are in a good agreement. Vertical position of the centroids on both pictures are slightly different. It can be explained by the fact that the exact position of the laser and the detector center were not perfectly aligned with respect to the center of the ion beam.

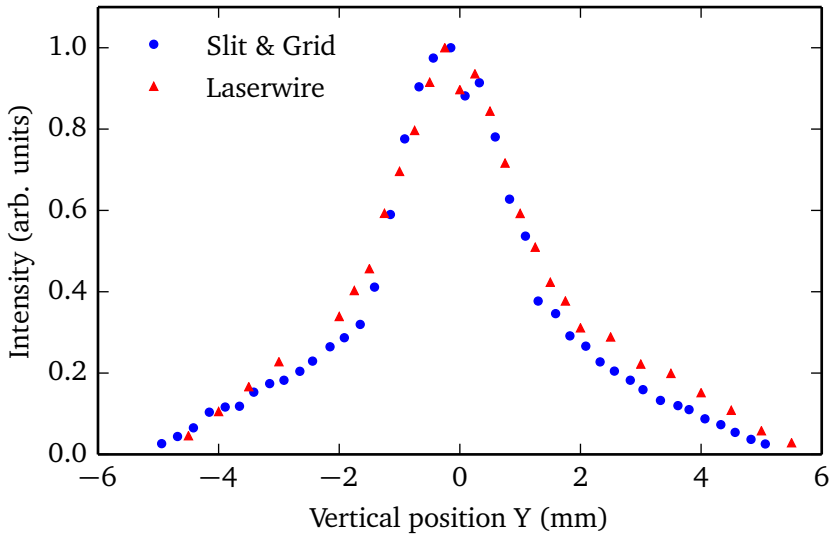


Figure 3.33. Vertical profile of the 3 MeV H⁻ beam measured by laserwire and SEM-grid.

In order to compare these measurements, the vertical profiles of the ion beam were calculated using phase-space distribution. The vertical profile of the ion beam obtained as a horizontal projection of the phase-space distribution for both laserwire and slit and grid measurements is presented in Fig. 3.33. As one can see the beam core is in a very good agreement. Values at the tails are slightly different. Also, it should be noted that the beam profiles obtained with two different methods have a non-Gaussian shape similar to the one presented in Fig. 3.30. The fact that the vertical profile of the ion beam has a non-Gaussian shape regardless of the measurement methods indicates that such shape of the beam is caused by the processes of the beam generation and transportation, but not by the measurement system itself.

The phase space data presented in Fig. 3.31 and Fig. 3.32 were used to calculate the geometrical RMS emittance. The method for the emittance calculation is described in section 3.0.1. The vertical emittance measured with laserwire technique was found to be 2.905 $\pm$ 0.027 mm mrad. Emittance measured with slit and grid technique was 3.492 $\pm$ 0.026 mm mrad. For both the slit-grid and laserwire systems, the result of calculation depends on the data thresholding which is used in order to filter out the noise from the RMS calculation. The basic idea of thresholding is to exclude all wire and diamond detector signals with an amplitude below a percentage of the maximum amplitude mea-

sured during the whole scan. Both laserwire and slit-grid systems had shown very good agreement [114].

## 3.2 Chapter summary

Principles and implementation of the laserwire for measuring the beam profile and emittance of negative hydrogen ions have been presented in this chapter. Implementation of the laserwire technique was demonstrated by the profile and emittance measurements of the $H^-$ beam performed at CERN LINAC4 accelerator. Author's contribution to the laserwire project at CERN LINAC4 was as following:

- Commissioning and integration of the laser system to the LINAC4 setup at 3 MeV stage.
- Tuning the laserwire system including measurements and analysis of the laser beam parameters.
- Participating in the operational shifts for data taking.
- Development an analysis algorithm and Python based software to reconstruct the vertical profile and transverse vertical RMS emittance from the data measured by the laserwire system.
- Presentation of the results at International Conferences and Symposia.
- Preparation of graphic material and writing of conference proceedings [110, 111, 114]

Achievements reached during the laserwire operation at CERN LINAC4 can be summarised as following:

- The milestone of proving the feasibility of laser-stripping $H^-$ profile and emittance measurement with a relatively low power laser source was for the first time successfully achieved during the CERN LINAC4 commissioning at 3 MeV.
- The measured signal and background levels compare very well with the expected ones from simulations.
- The experimental setup allowed a set of complete emittance scans to be performed, which then was cross-checked with the operational slit and grid system. The emittance measured with laserwire system was found to be $2.905 \pm 0.027$ mm mrad. Emittance measured with slit and grid technique was $3.492 \pm 0.026$ mm mrad.
- These encouraging results, to be complemented by more tests at 12 MeV commissioning stage of the LINAC4, represent the first step towards the design of one or more laserwire systems for the LINAC4 at the top energy of 160 MeV.

# Chapter 4

# Future plans and prospects

*The afternoon knows what the morning never suspected.*

– Robert Frost

## 4.1 Micron scale laserwire for future linear colliders

DESPITE the successful demonstration of the laserwire at ATF2 it is clear that several improvements could be made to reduce the measurements uncertainty for the laserwire system required for future linear colliders. These improvements include the following [31]:

- New design of the vacuum chamber optimized for cost and ease of operation can be implemented for future laserwire station. This vacuum chamber can be manufactured smaller in size and put on the light weight mover system. The small laserwire vacuum chamber would be surrounded by a small optical system to move the laser beam onto the final focus lens and safely deal with the outgoing laser beam.

- The spatial quality of the laser source could be improved. The laser source that was used in the experiment at ATF2 was astigmatic and had a non-Gaussian profile. In particular, the non-Gaussian nature makes the $M^2$ model an approximation of the size of the laser beam and not the true intensity distribution. A laser with a better spatial profile would adhere much more closely to the $M^2$ model and reduce the systematic uncertainty of the measured electron beam sizes. Fibre lasers are a promising technology that could provide high spatial quality pulses at a much higher repetition rate with high overall efficiency. Fibre lasers are not able to provide the gigawatt peak powers used for this laserwire system, but in a well characterized environment with a higher bunch charge electron beam such as a future linear collider, the peak power requirements would be considerably lower. On the other hand a second stage amplification can be foreseen.

- In an ideal laserwire diagnostic station there would be two laser beam lines orthogonal to each other; one for the vertical and one for the horizontal beam size measurement. In the case of an electron beam with a high aspect ratio, the major axis of the elliptical beam could be measured using a simple deconvolution requiring no knowledge of the minor axis size. This measurement of the major axis could then be used to deconvolve the laserwire scans of the smaller minor axis that may exhibit Rayleigh range effects.

- Maximizing the signal-to-noise ratio of the Compton scattering rate measurement is key to improving the precision of the laserwire measurement and therefore minimizing the error in the emittance measurement. Although the electron beam optics developed for laserwire operations reduced the background significantly, the background signal level was still significant and limits the precision of the measurement. The effect of pointing jitter on the Compton-scattered photons as well as background conditions should be simulated.

- For a more complete system, the beam charge and laser pulse energy need to be measured with uncertainties significantly less than the Compton or background signal variation. This is possible with high resolution direct current transformers for the particle beam, but the laser energy measurement systems would need more careful and systematic verification of performance before use with a laserwire system.

The laserwire project at the ATF2 is now complete and desired resolution is achieved. Now a technical design report is being prepared to be included into the CLIC Technical Design Report.

## 4.2 OTR/ODR programe at ATF2

Currently, laserwire beam profile scanners are the main candidates for non-invasive high resolution measurements for future linear colliders and represent the state-of-the-art in the area of transverse beam size and emittance diagnostics. Recently a micron scale resolution was successfully demonstrated at the ATF2 beam line at KEK (see Chapter 2). However, over a distance of more than 40 km many laserwire monitors would be required. Both the complexity and the cost of a laserwire system reveals a need to develop a simple in use, robust, and relatively inexpensive alternative device with comparable accuracy and resolution.

Recent experiments on beam profile measurements using Optical Transition Radiation (see section 2.3 of Chapter 2) and Optical Diffraction Radiation [115] show that such monitors are capable of measuring the size of the electron beam with micron resolution. Following the success of these experiments it has been proposed to develop, install and test a combined OTR/ODR emittance station at ATF2 with an opportunity to measure Ultra Violet/soft X-ray radiation to minimize the diffraction limit effects [116]. The proposal

includes design and manufacture a new vacuum system, targets and their manipulation system, optical photon transport and the data acquisition.

The main goal of this programme is to achieve the resolution for the measurement with OTR/ODR smaller than 1 $\mu$m with room for improvement on that limit down to a few tens of nanometers. One possibility to improve the resolution is to go down a wavelength of 70 nm. This would improve the measurements both for OTR and ODR to a great extent, however it would mean that the entire optical system needs to be located inside the vacuum chamber. Also, the choice of camera which takes images of the angular distribution can be challenging in this case. It might be possible possible to use a CCD or an intensifier such as an extreme UV photocathode. Since the optical resolution is a key element in the measurement, the magnification of the optical system will be an issue. Therefore, a two-lens system i.e. a telescope will be designed. An extensive simulations have to be made in order to decide on appropriate OTR/ODR target parameters and improve the resolution of the optical system.

## 4.3 Design of the laserwire station for 160 MeV at CERN LINAC4

To fully characterize the ion beam at the final 160 MeV section of the LINAC4, it is proposed to use two laserwire stations. The proposed layout of the system is shown in Fig. 4.1. Both stations will be able to measure the ion beam emittance and profile in horizontal and vertical planes. Due to the close proximity to the beam dump and high energy of the ion beam the radiation level must be taken into account. This fact mostly affects two main systems of the laserwire meter: the laser system and detection system.

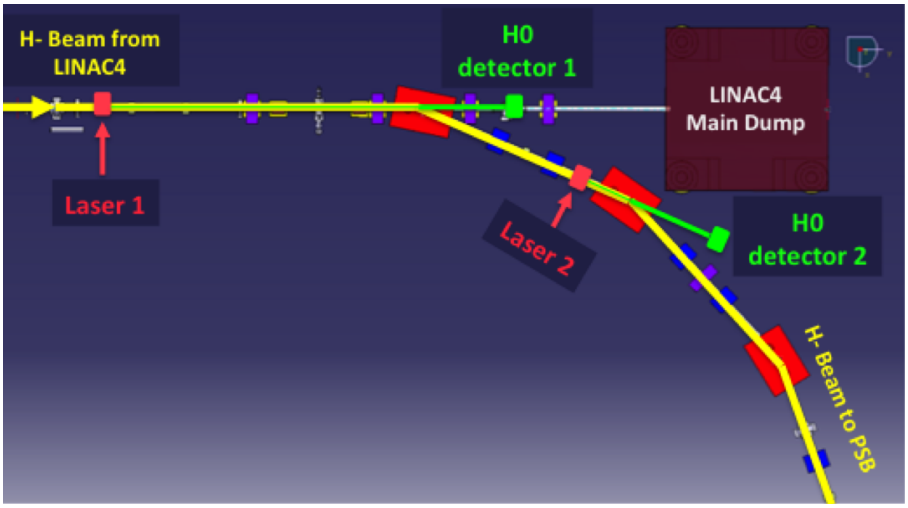


Figure 4.1. Layout of the two laserwire stations at the transfer line of the 160 MeV section of the LINAC4 (picture from [110]).

To avoid the damage of the laser system due to the high radiation level it will be located in the special hutch on the surface above the accelerator enclosure. The laser optical system will be the same as it was designed for 3 MeV stage. The laser beam from

the source will be delivered to the IP using optical fibre of approximately 20 m in length.

Another main concern is to choose the detection system for the final laserwire design. The first candidate for measuring the profile of $H^0$ particles at 160 MeV is the diamond detector successfully tested at 3 MeV. For the final design, the number of read-out channels of the detector can be increased by changing the design of the front electrodes. Instead of five electrodes with 3.5 mm width that was used at 3 MeV measurement, it is possible to use metallization pattern with up to 35 strips and width of 500 $\mu$m per channel. Even though the diamond detector has a very high radiation hardness (e.g. in comparison to the silicon detectors), it has been demonstrated that the detector already showed a degradation after the measurements at 3 MeV $H^-$ beam. As an alternative, a Gas Electron Multiplier (GEM) [117] can be used as a detector for final system, however this possibility is still under investigation.

As an addition to the diamond detector a detection system for the stripped electrons can be used to measure the ion beam profiles at 160 MeV. Such detection scheme can be implemented by installing a weak bending magnet immediately after the LWIP that will steer photodetached electrons to the detector. As a detector, a Faraday cup can be used to collect these electrons. In order to achieve sufficient time resolution, the Faraday cup as well as its read-out electronics will have to be designed to resolve laser pulses of 80 ns in length.

For 160 MeV ion beam, stripped electrons will have the kinetic energy of 87 keV. Thereby, a magnetic field of less than 0.02 T along the 8 cm gap is sufficient to turn such electrons to 90 degrees. Initial beam of $H^-$ particles passing through such magnet will be deflected less than 1 mrad and can be returned to its original trajectory by installing corrector magnet with opposite polarity [110].

## 4.4 Laserwire emittance meter at the Front End Test Stand

The Front End Test Stand project at Rutherford Appleton Laboratory (RAL) built in collaboration between ISIS, ASTeC, Imperial College London, University of Warwick, Uni-

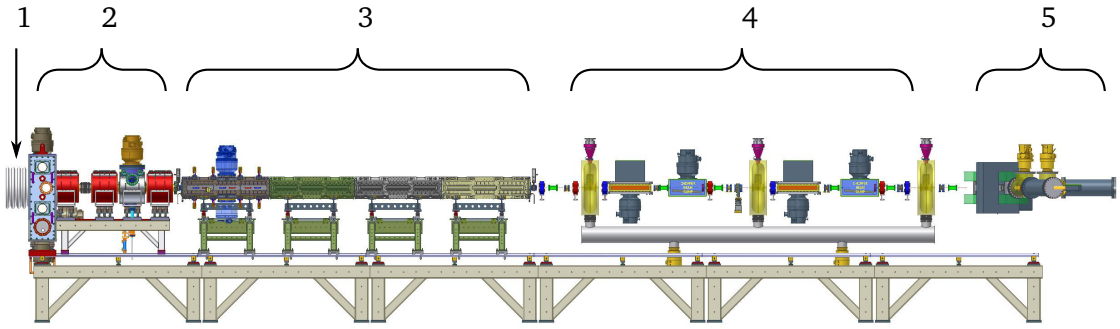


Figure 4.2. Schematic layout of the FETS. 1 - ion source, 2 - LEBT, 3 - RFQ, 4 - MEBT, 5 - Laser diagnostics (picture from [118]).

versity College London and John Adams Institute at Royal Holloway, University of London is designed to create a high quality, low emittance, high current, high duty factor $H^-$ beam required for wide variety of future proton-accelerator projects. These applications include future upgrades of the ISIS neutron source, future Spallation Neutron Sources, a Neutrino Factory, Muon Collider, Accelerator Driven Sub-critical Systems and Waste Transmuters [119, 120]

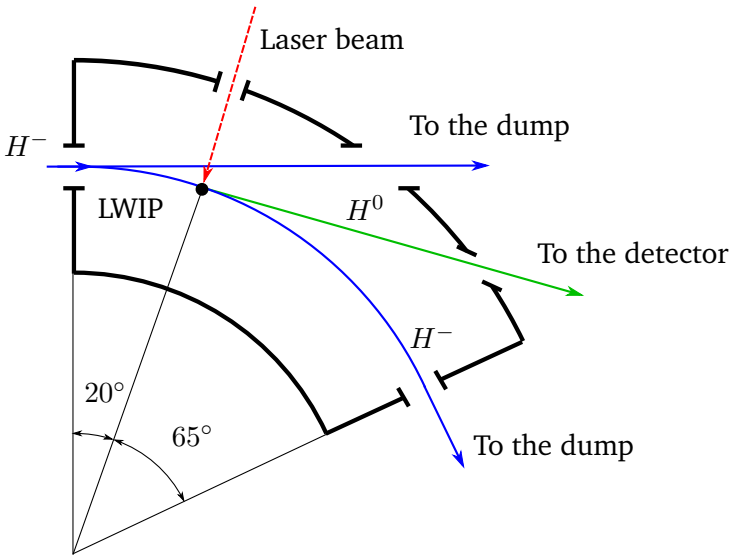


Figure 4.3. Schematic of the interaction point.

The schematic layout of the FETS main elements presented in Fig. 4.2. The FETS consists of a caesium-enhanced penning surface plasma $H^-$ ion source [121], a three-solenoid magnetic low energy beam transport (LEBT) [122], a 324 MHz, 4 metre radio frequency quadrupole (RFQ) [123], an electromagnetic quadrupole and rebunching cavity medium energy beam transport (MEBT) [124] and laser diagnostics section (LD). The main parameters of the FETS ion beam presented in table 4.1

Table 4.1. General parameters of the FETS.

| **Parameter** | **Value** | **Value** |
|---|---|---|
| Ion beam energy | 3 | MeV |
| Ion beam current | 60 | mA |
| Ion beam micropulse width | ∼3 | ns |
| Ion beam macropulse width | 2 | ms |
| Ion beam repetition rate | 50 | Hz |
| Ion beam waist (from simulations): | | |
| $\sigma_x$ | 3.87 | mm |
| $\sigma_y$ | 4.38 | mm |

A detailed layout of the FETS laser diagnostics section is shown in Fig. 4.4. Laser diagnostic section is designed to measure the emittance of a high power $H^-$ beam and consists of a main beam dump in straight forward direction (1), a quadrupole doublet to diffuse the beam after the LD dipole (2), a laser delivery system (3), a quadrupole doublet at the entrance to the LD dipole (4), a LD dipole (5), a quadrupole doublet in front of the secondary beam dump (6), a secondary beam dump (7) and detector (8) [125].

In order to reduce the background of the neutral particles, mostly generated by stripping $H^-$ ions in interactions with the residual gas, the LW interaction point is designed to be located inside the dipole magnet. To implement such scheme special vacuum chamber for the dipole magnet has been designed. Schematic of the vacuum chamber showing the laserwire interaction is presented in Fig. 4.3. The beam of $H^-$ enters the vacuum chamber through the round port in the front face. When the magnet is off the ion beam is passing straight through the vacuum chamber to the beam dump. When the dipole magnet is powered on the main beam is deflected to 65° and coming out from the vacuum vessel to the second beam dump. The background of neutral particles is coming straight through the vacuum chamber to the first beam dump. The laser beam enters the vacuum chamber through the port which is located at 20° from the front face of the vacuum chamber. After the laserwire interaction, the beam of neutrals continues its propagation on tangent trajectory. After exiting the vacuum chamber the beam of $H^0$ particles is intercepted by the detector. Such geometry allows to separate neutrals coming from laser stripping and from the background.

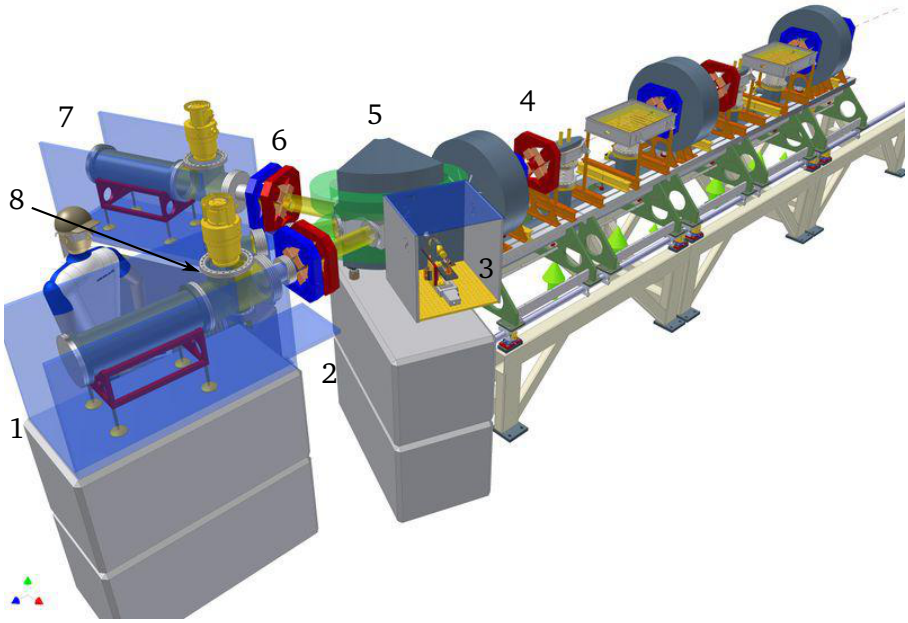


Figure 4.4. Schematic layout of the laser diagnostics setup (picture from [118]).

To detect the angular distribution of the neutralized particles a crystal or organic scintillator screen placed downstream of the vacuum chamber is planned to be used. The

light, produced in interaction of the $H^0$ with the scintillator material, then will be guided to the CCD camera. The CCD camera will be placed out of the beamline plane in order to avoid radiation damage of the camera sensor [126]. In order to choose correct size and material of the scintillator and to design an optical system, a simulation of the laserwire interaction is required.

### 4.4.1 Simulation of the laserwire interaction

In order to design an effective detection system it is necessary to estimate the yield and the spatial distribution of the neutralized particles arriving at the detector [127].

To estimate the number of neutralized particles and hence the yield one can use Eq. 2.1 and Eq. 2.2. Parameters for the FETS ion beam are presented in Table 4.1. Parameters for the laser system are the same as described in Chapter 3. Substituting these parameters into Eqs 2.1–2.2 and assuming that both the ion beam and laser beam have Gaussian distribution, one can obtain approximately $1.83\times10^5$ neutral particles produced in one interaction. Assuming that each laser macropulse consists of approximately 60 micropulses (at 30 kHz) and each laser micropulse interacts with approximately 30 ion bunches, the total number of $H^0$ particles arriving at the detector per laser pulse per ion beam macropulse can be estimated as $\sim 1.8 \times 10^8$.

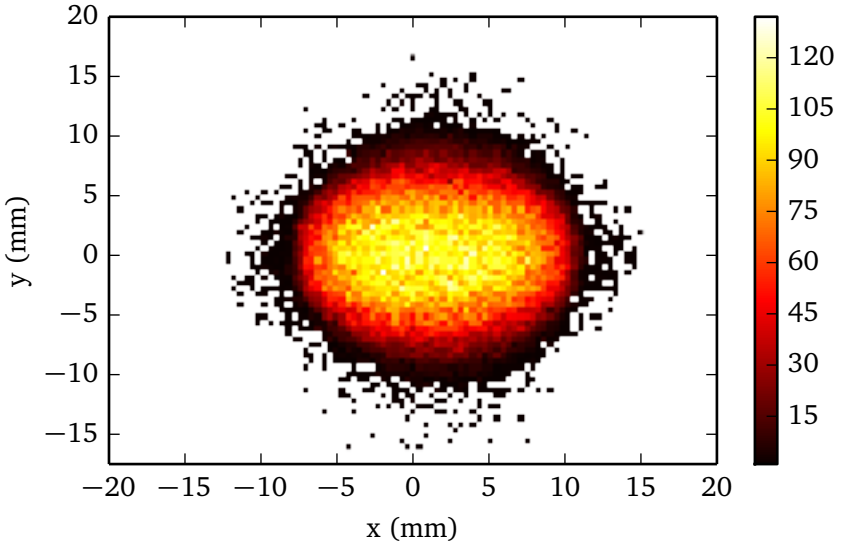


Figure 4.5. Distribution of the $H^-$ ions at the LWIP.

In order to simulate the spatial distribution of the $H^0$ particles arriving at the detector one can use the procedure described in section 3 of Chapter 3. To simulate the laserwire interaction, each particle in the initial distribution was weighted with photodepachment probability calculated using Eq. 3.2. As one can see from Eq. 3.2 the stripping probability depends on three parameters: the cross-section of the process – which is constant for certain wavelength of the laser, time of the interaction – which, in the presented case, is laser micropulse length and the laser photons flux. The flux of the laser photons can be

calculated as following:

$$\rho(x,y) = \frac{I(x,y)}{\hbar\omega}, \tag{4.1}$$

where $\hbar\omega$ is the energy of the single photon and $I(x,y)$ is the intensity profile of the laser. The intensity profile can be calculated using the common formula [23]:

$$I(x,y) = \frac{2P}{\pi w(x)^2} \exp\left(\frac{-2y^2}{w(x)^2}\right). \tag{4.2}$$

Here $P$ is the laser peak power, $w(x)$ is the laser beam radius at distance $x$ from the waist (see Chapter 2 section 2.1 for details) and $y$ is the radial distance from the center axis of the laser beam.

The distribution of the $H^-$ ions at the laserwire interaction point was obtained using a General Particle Tracer [128] code, that simulates the propagation of the ions trough the lattice with real parameters. The particle distribution at the LWIP simulated for the nominal lattice parameters is shown in Fig. 4.5.

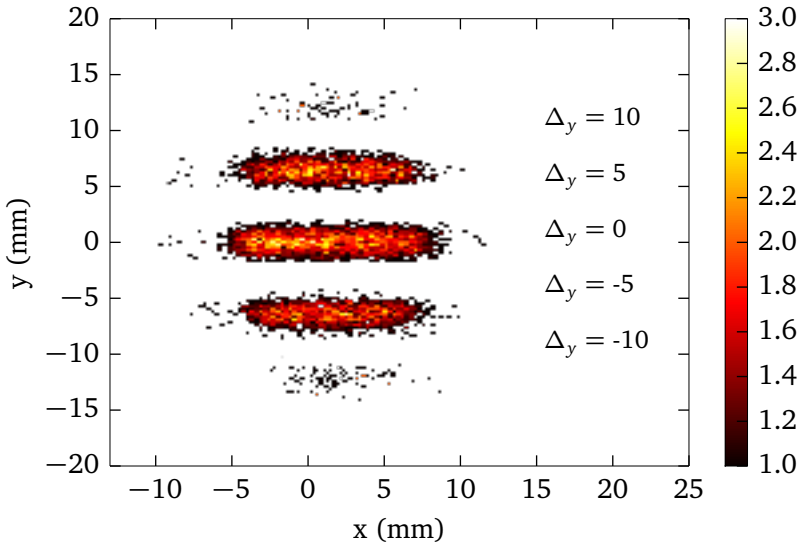


Figure 4.6. Distribution of the neutral particles at the detector plane (∼0.5 m downstream the IP) for different vertical laser focus positions.

Each particle of the initial distribution was weighted with its stripping probability. After a drift of about 0.5 m from the LWIP towards the detector the weighted particles were integrated. An example of the resultant distribution of the neutralized particles at the detector for different vertical laser focus positions in range from -10 mm to 10 mm with step of 5 mm is presented in Fig. 4.6. As one can see from the picture, with nominal lattice settings the scintillator screen size has to be no less than 40 mm in vertical and 30 mm in horizontal direction.

The simulated vertical laserwire scan along with the vertical ion beam profile, obtained from initial distribution, is shown in Fig. 4.7. As one can see from the graph the simulated profile overlaps the original profile very well.

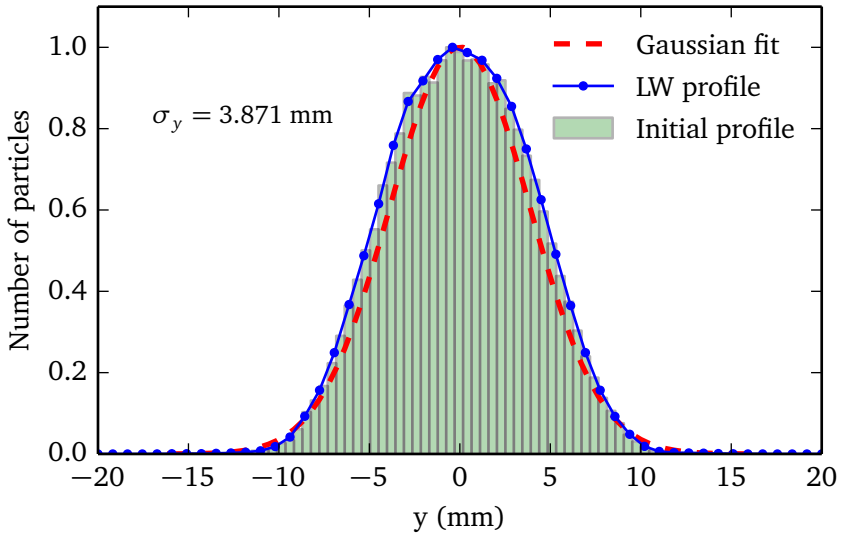


Figure 4.7. Number of neutralized particles as a function of the vertical laser focus displacement.

## 4.5 Chapter summary

This chapter has described the future plans of three experiments: sub-micrometre electron beam profile measurements at the ATF2 using optical transition and diffraction radiation, future development of the laserwire emittance scanner for CERN LINAC4 and development of the laserwire emittance meter for measuring the $H^-$ ion beam at FETS.

The contribution of the author to the laserwire project at FETS was the following:

- Development of a Python based code to simulate the laserwire interaction for the FETS $H^-$ beam. The code utilizes the measured laser propagation and simulated ion beam distribution at the IP as input parameters. As a result, it calculates the total yield of neutral particles produced in laserwire interaction and also calculates the spatial distribution of neutrals at the detector. The code has been tested with ion beam distribution simulated for nominal lattice settings. Once the design of the machine will be finalized this software can be used to design an effective detection system and optimize its parameters.
- Presentation of the results at International Conferences and Symposia.
- Preparation of graphic material and writing of conference proceedings [127]

# Chapter 5

# Conclusions and outlook

*A conclusion is the place where you got tired of thinking.*

– Arthur Bloch

THIS thesis has provided a comprehensive and detailed overview of the implementation of laserwire technology for measuring the parameters (transverse beam profile and emittance) of the particle beam of electrons and negative hydrogen ions. The study of the laserwire transverse beam diagnostic including description of the basic principles of operation and detailed technical implementation has been demonstrated with the example of two diverse experiments. First experiment aims to demonstrate a sub-micrometer resolution laserwire measurement of the electron beam at ATF2 in KEK, Japan. The second one is dedicated to the development of the laserwire emittance meter for measuring the $H^-$ beam at LINAC4 in CERN, Switzerland.

The laserwire system at ATF2 has demonstrated a high resolution and relatively non-invasive method of measuring the transverse profile of a high charge density, low emittance electron beam that is required for future linear electron positron-positron colliders such as CLIC or ILC. A minimum vertical electron beam size of 1.07 $\pm$ 0.06 (stat.) $\pm$ 0.05 (sys.) $\mu$m has been measured with a corresponding horizontal beam size of 119 $\pm$ 2.4 (stat.) $\pm$ 0.01 (sys.) $\mu$m. Vertical geometric emittance of 82.56 $\pm$ 3.04 pm rad was measured using quadrupole scan technique.

The main challenge of measuring the small electron beams (where the Rayleigh range of the laser is much less than the size of the electron beam) is correctly deconvolve the beam size from the laserwire scan. Simultaneous fitting of the data from the horizontal and vertical laserwire scans using the overlap integral model was demonstrated in the presence of Rayleigh range effects and was shown to provide an accurate measurement of both the horizontal and the vertical electron beam sizes. This has demonstrated that Rayleigh range effects do not preclude the use of a laserwire to measure a high aspect ratio beam. Furthermore, an alignment method capable of finding collisions between the laser and electron beam in under 20 min was developed.

In addition to the laserwire system at ATF2 the OTR experiment has been also de-

scribed. Initially, the OTR beam profile monitor has been designed as an auxiliary device for the laserwire monitor and then has turned into a separate R & D program. The same location of the laserwire and OTR interaction point allowed to cross-check the results of both techniques. Study of the aberration effects and improving the optical system of the OTR monitor lead to possibility of measuring the transverse beam size with sub-micrometre resolution. The minimum measured vertical electron beam size was found to be $0.754 \pm 0.034$ $\mu$m. Vertical geometric emittance measured in a single quadrupole scan was found to be $59.306 \pm 4.153$ pm rad which is very consistent with the laserwire measurements.

The design and initial results from the commissioning and testing of the laserwire system installed at 3 Mev LINAC4 in CERN have demonstrated the ability of measuring the transverse profile and emittance of the $H^-$ beam. The novelty of this system is the use of the low power infrared laser and delivery of the laser pulse to the interaction point via flexible optical fibre. Results of the laserwire emittance measurements collected during the measurements campaign at 3 Mev commissioning stage and cross-checked with the results obtained with conventional slit and grid technique showed a very good agreement with the expected ones from simulations. The current design of the laserwire meter has proved its feasibility and can be used for the final system at the top LINAC4 energy of 160 MeV. Simulation results of the laserwire system for the FETS project (still under construction at RAL in the UK) designed in a close collaboration with LINAC4 laserwire project have also been presented.

Over more than twenty years of development, the laserwire technology has become the state-of-the-art method in particle beam diagnostics. Despite some imperfections in technical realisation of the method, the interest of the international community in the laserwire will encourage the further development of this elegant technique.

# Bibliography

[1] Lyndon Evans and Philip Bryant. LHC machine. *Journal of Instrumentation*, 3(8):S08001, 2008.

[2] D. Iwanenko and I. Pomeranchuk. On the maximal energy attainable in a betatron. *Phys. Rev.*, 65:343–343, Jun 1944.

[3] F. R. Elder, A. M. Gurewitsch, R. V. Langmuir, and H. C. Pollock. Radiation from electrons in a synchrotron. *Phys. Rev.*, 71:829–830, 1947.

[4] International Linear Collider: Technical design report, 2013.

[5] A multi-TeV linear collider based on CLIC technology: CLIC conceptual design report, edited by M. Aicheler, P. Burrows, M. Draper, T. Garvey, P. Lebrun, K. Peach, N. Phinney, H. Schmickler, D. Schulte and N. Toge, cern-2012-007, 2012.

[6] J.D. Jackson. *Classical electrodynamics*. John Wiley & Sons, 1998.

[7] E.J.N Wilson. *An Introduction to particle accelerators*. OXFORD University Press, 2001.

[8] M.S. Livingston and J.P. Blewett. *Particle accelerators*. New York: McGraw-Hill Book Company, 1962.

[9] H. Wiedemann. *Particle Accelerator Physics*, volume 1 and 2. Springer, 2003.

[10] S.Y. Lee. *Accelerator Physics*. World Scientific, Singapore, 2d edition, 2004.

[11] M.C. Ross, J.T. Seeman, R.K. Jobe, J.C. Sheppard, and R.F. Stiening. High resolution beam profile monitors in the SLC. *Nuclear Science, IEEE Transactions on*, 32(5):2003–2005, 1985.

[12] R. Fulton, J. Haggerty, R. Jared, et al. A high resolution wire scanner for micron-size profile measurements at the slc. *Nuclear Instruments and Methods in Physics Research Section A: Accelerators, Spectrometers, Detectors and Associated Equipment*, 274(1–2):37 – 44, 1989.

[13] H. Hayano. Wire scanners for small emittance beam measurement in ATF. In *Proceedings of XX International Linac Conference*, pages 146–148, Monterey, USA, 2000.

[14] P. Karataev, A. Aryshev, S. Boogert, et al. First observation of the point spread function of optical transition radiation. *Physical Review Letters*, 107:174801, 2011.

[15] M. Castellano. A new non-intercepting beam size diagnostics using diffraction radiation from a slit. *Nuclear Instruments and Methods in Physics Research Section A: Accelerators, Spectrometers, Detectors and Associated Equipment*, 394(3):275 – 280, 1997.

[16] Pavel Karataev, Sakae Araki, Ryosuke Hamatsu, et al. Beam-size measurement with optical diffraction radiation at KEK Accelerator Test Facility. *Phys. Rev. Lett.*, 93:244802, 2004.

[17] Tsumoru Shintake. Proposal of a nanometer beam size monitor for $e^+e^-$ linear colliders. *Nuclear Instruments and Methods in Physics Research Section A: Accelerators, Spectrometers, Detectors and Associated Equipment*, 311(3):453 – 464, 1992.

[18] K.T. McDonald and D.P. Russell. Methods of emittance measurement. In *Frontiers of Particle Beams; Observation, Diagnosis and Correction*, volume 343 of *Lecture Notes in Physics*, pages 122–132. Springer Berlin Heidelberg, 1989.

[19] M.G. Minty and F. Zimmermann. *Measurement and control of charged particle beams*. Springer-Verlag Berlin Heidelberg, 2003.

[20] I. Agapov, G.A. Blair, and M. Woodley. Beam emittance measurement with laser wire scanners in the International Linear Collider beam delivery system. *Physical Review Special Topics - Accelerators and Beams*, 10:112801, 2007.

[21] P. Tenenbaum and T. Shintake. Measurement of small electron-beam spots. *Annual review of nuclear and particle science*, 49:125, 1999.

[22] M.E. Peskin and D.V. Schroeder. *An Introduction To Quantum Field Theory*. Westview Press, 1995.

[23] A.E. Siegman. *Lasers*. University Science Books, 1986.

[24] T.F. Johnston. Beam propagation ($M^2$) measurement made as easy as it gets: the four-cuts method. *Applied optics*, 37(21):4840–4850, 1998.

[25] ATF2 group, ATF2 proposal, KEK report no. 2005-2, 2005.

[26] G. R. White, R. Ainsworth, T. Akagi, et al. Experimental validation of a novel compact focusing scheme for future energy-frontier linear lepton colliders. *Physical Review Letters*, 112(3):034802, 2014.

[27] Y. Honda, K. Kubo, S. Anderson, et al. Achievement of ultralow emittance beam in the accelerator test facility damping ring. *Physical Review Letters*, 92(5):054802, 2004.

[28] Accelerator test facility project, http://www.atf.kek.jp.

[29] S.T.Boogert, G.A. Blair, G. Boorman, et al. Micron-scale laser-wire scanner for the KEK Accelerator Test Facility extraction line. *Physical Review Special Topics - Accelerators and Beams*, 13(12):122801, 2010.

[30] L. Corner, A. Aryshev, G.A. Blair, et al. Laserwire: A high resolution non-invasive beam profiling diagnostic. *Nuclear Instruments and Methods in Physics Research Section A: Accelerators, Spectrometers, Detectors and Associated Equipment*, 740:226 – 228, 2014.

[31] L. J. Nevay, S. T. Boogert, P. Karataev, et al. Laserwire at the Accelerator Test Facility 2 with submicrometer resolution. *Physical Review Special Topics - Accelerators and Beams*, 17:072802, 2014.

[32] Y. I. Kim, R. Ainsworth, A. Aryshev, et al. Cavity beam position monitor system for the Accelerator Test Facility 2. *Physical Review Special Topics - Accelerators and Beams*, 15:042801, 2012.

[33] Glen White, Stephen Molloy, Andrei Seryi, et al. A flight simulator for ATF2 - a mechanism for international collaboration in the writing and deployment of online beam dynamics algorithms. In *Proceedings of EPAC08*, pages 1562–1564, Genoa, Italy, 2008.

[34] Hamamatsu photonics k.k. http://www.hamamatsu.com.

[35] Experimental physics and industrial control system, http://www.aps.anl.gov/epics/.

[36] Python software foundation. python language reference, version 2.7. available at http://www.python.org.

[37] J.D. Hunter. Matplotlib: A 2d graphics environment. *Computing In Science & Engineering*, 9(3):90–95, 2007.

[38] C. Elliott, V. Vijayakumar, W. Zink, and R. Hansen. National instruments labview: A programming environment for laboratory automation and measurement. *Journal of Laboratory Automation*, 12:17–24, 2007.

[39] Laurence James Nevay. *Results from the laser-wire at ATF2 and development of a fibre laser for its upgrade*. PhD thesis, Wolfson College, Oxford, 2011.

[40] Cvi laser optics http://www.cvilaseroptics.com.

[41] Dataray inc. http://www.dataray.com.

[42] F. James and M. Roos. Minuit - a system for function minimization and analysis of the parameter errors and correlations. *Computer Physics Communications*, 10(6):343–367, 1975.

[43] Marc Ross, Scott Anderson, Josef Frisch, et al. Very high resolution optical transition radiation beam profile monitor. *AIP Conference Proceedings*, 648(1):237–247, 2002.

[44] J. Alabau-Gonzalvo, C. Blanch Gutierrez, A. Faus-Golfe, et al. Optical transition radiation system for ATF2. In *Proceedings of IPAC2011*, pages 1317–1319, San-Sebastian, Spain, 2011.

[45] V.L. Ginzburg and I.M. Frank. On the transition radiation theory. *Sov. Phys. JETP*, 16:15, 1946.

[46] P. Goldsmith and J. V. Jelley. Optical transition radiation from protons entering metal surfaces. *Philosophical Magazine*, 4(43):836–844, 1959.

[47] V. L. Ginzburg and V.N. Tsytovich. *Transition Radiation and Transition Scattering*. Series on Plasma Physics. CRC Press, 1990.

[48] M.L. Ter-Mikaelian. *High-energy Electromagnetic Processes in Condensed Media*. Tracts on Physics & Astronomical. John Wiley & Sons Inc, 1972.

[49] A. P. Potylitsyn. *Electromagnetic Radiation of Electrons in Periodic Structures*. Springer Berlin Heidelberg, 2011.

[50] A. Aryshev, S. T. Boogert, D. Howell, et al. A novel method for sub-micrometer transverse electron beam size measurements using optical transition radiation. *Journal of Physics: Conference Series*, 236:012008, 2010.

[51] M. Castellano and V. A. Verzilov. Spatial resolution in optical transition radiation beam diagnostics. *Physical Review Special Topics - Accelerators and Beams*, 1:062801, 1998.

[52] V.A. Verzilov. Transition radiation in the pre-wave zone. *Physics Letters A*, 273:135–140, 2000.

[53] M. Castellano, A. Cianchi, G. Orlandi, and V.A. Verzilov. Effects of diffraction and target finite size on coherent transition radiation spectra in bunch length measurements. *Nuclear Instruments and Methods in Physics Research Section A: Accelerators, Spectrometers, Detectors and Associated Equipment*, 435:297–307, 1999.

[54] Zemax - optical and illumination design software, http://www.zemax.com.

[55] B. Bolzon, T. Lefevre, S. Mazzoni, et al. Results of the high resolution OTR measurements at KEK and comparison with simulations. In *Proceedings of IBIC2013*, pages 204–207, Oxford, UK, 2013.

[56] B. Bolzon, T. Lefevre, S. Mazzoni, et al. Improvement of beam imaging system through optics propagation simulations. In *Proceedings of IPAC2014*, pages 3709–3711, Dresden, Germany, 2014.

[57] T. Aumeyr, M.G. Billing, L.M. Bobb, et. al. Advanced simulations of optical transition and diffraction radiation. *Physical Review Special Topics - Accelerators and Beams*, 18:042801, 2015.

[58] A. Aryshev, N. Terunuma, J. Urakawa, et al. Sub-micrometer resolution transverse electron beam size measurement system based on optical transition radiation. In *Proceedings of IPAC'10*, pages 193–195, Kyoto, Japan, 2010.

[59] K. Kruchinin, S. T. Boogert, P. Karataev, et al. Extremely low emittance beam size diagnostics with sub-micrometer resolution using optical transition radiation. In *Proceedings of IBIC2013*, pages 615–618, Oxford, UK, 2013.

[60] K. Kruchinin, A. Aryshev, P. Karataev, et al. Sub-micrometer transverse beam size diagnostics using optical transition radiation. *Journal of Physics: Conference Series*, 517:012011, 2014.

[61] Thorlabs inc. http://www.thorlabs.de.

[62] Physik instrumente (pi) gmbh & co. kg http://www.physikinstrumente.com.

[63] Sigmakoki http://www.sigma-koki.com.

[64] Suruga seiki co., ltd. http://www.eng.surugaseiki.com.

[65] Standa ltd http://www.standa.lt.

[66] Sbig astronomical instruments http://www.sbig.com.

[67] A. Bovic. *The Essential Guide to Image Processing*. Elsevier, 2009.

[68] S.B. Howell. *Handbook of CCD astronomy*. Cambridge University Press, 2000.

[69] Sad, strategic accelerator design, http://www.acc-physics.kek.jp/sad.

[70] K. Levenberg. A method for the solution of certain non-linear problems in least squares. *The Quarterly of Applied Mathematics*, 2:164–168, 1944.

[71] H.H. Ku. Notes on the use of propagation of error formulas. *Journal of Research of the National Bureau of Standards - C. Engineering and Instrumentation*, 70C(4):263–273, 1966.

[72] L.J. Nevay, G.A. Blair, S.T. Boogert, et al. Sub-micrometre resolution laserwire transverse beam size measurement system. In *Proceedings of IPAC2013*, pages 795 – 797, Shanghai, China, 2013.

[73] J. Urakawa and N. Terumuma. Sub-micrometre resolution laserwire transverse beam size measurement system. In *Proceedings of IBIC2014*, pages 244 – 247, Oxford, UK, 2014.

[74] G. I. Dimov. Use of hydrogen negative ions in particle accelerators. *Review of Scientific Instruments*, 67(10):3393, 1996.

[75] W.B. Cottingame, G.P. Boicourt, J.H. Cortez, et al. Noninterceptive techniques for the measurement of longitudinal parameters for thr intense $H^-$ beams. *IEEE Transactions on Nuclear Science*, NS-32(5):1871–1873, 1985.

[76] R C Connolly, K F Johnson, D P Sandoval, and V Yuan. A transverse phase-space measurement technique for high-brightness, $H^-$ beams. *Nuclear Instruments and Methods in Physics Research Section A: Accelerators, Spectrometers, Detectors and Associated Equipment*, 312(3):415–419, 1992.

[77] V W Yuan, R C Connolly, R C Garcia, et al. Measurement of longitudinal phase space in an accelerated $H^-$ beam using a laser-induced neutralization method. *Nuclear Instruments and Methods in Physics Research Section A: Accelerators, Spectrometers, Detectors and Associated Equipment*, 329:381–392, 1993.

[78] R. Connolly, P. Cameron, J. Cupolo, et al. Laser beam profile monitor development at BNL for SNS. In *AIP Conference Proceedings*, volume 648, page 150, 2002.

[79] R. E. Shafer. Laser diagnostic for high current $H^-$ beams. In *Proceedings of LINAC98*, pages 535–537, 1998.

[80] Saeed Assadi. SNS transverse and longitudinal laser profile monitors design, implementation and results. In *Proceedings of EPAC 2006*, pages 3161–3163, Edinburg, Scotland, 2006.

[81] Y. Liu, A. Aleksandrov, S. Assadi, et al. Laser wire beam profile monitor in the spallation neutron source (SNS) superconducting linac. *Nuclear Instruments and Methods in Physics Research, Section A: Accelerators, Spectrometers, Detectors, and Associated Equipment*, 612:241–253, 2010.

[82] Y. Liu, A. Aleksandrov, C. Long, et al. Nonintrusive emittance measurement of 1 GeV $H^-$ beam. *Nuclear Instruments and Methods in Physics Research Section A: Accelerators, Spectrometers, Detectors and Associated Equipment*, 675:97–102, 2012.

[83] R Connolly, C Degen, L DeSanto, and D Raparia. A detector to measure transverse profiles and energy of an $H^-$ beam using gas stripping and laser photo neutralization. *Journal of Instrumentation*, 7(2):P02001, 2012.

[84] S.J. Smith and D.S Burch. Photodetachment cross section of the negative hydrogen ion. *Physical Review Letters*, 2(4):165–166, 1959.

[85] J.T. Broad W.P. Reinhardt. One- and two-electron photoejection from $H^-$: A multichannel j-matrix calculation. *Physical Review A*, 14(6):2159–2173, 1976.

[86] W.H. Kuan, T.F. Jiang, and K.T. Chung. Photodetachment of $H^-$. *Physical Review A*, 60(1):364–369, 1999.

[87] L. Arnaudon, P. Baudrenghien, M. Baylac, et al. Linac4 technical design report. Technical Report CERN–AB–2006–084 ABP/RF, European Organization For Nuclear Research CERN - AB Department, 2006.

[88] M. Vretenar, R. Garoby, K. Hanke, et al. Design of Linac4, a new injector for the cern booster. In *Proceedings of International Linear Accelerator Conference*, Lübek, Germany, 2004.

[89] M. Vretenar, L. Arnaudon, P. Baudrenghien, et al. Progress in the construction of Linac4 at CERN. In *Proceedings of LINAC2012*, pages 864–866, Tel-Aviv, Israel, 2012.

[90] M. Vretenar. Status and plans for Linac4 installation and commissioning. In *Proceedings of IPAC2014*, pages 3332–3334, Dresden, Germany, 2014.

[91] J. Lettry, D. Aguglia, P. Andersson, et al. Status and operation of the Linac4 ion source prototypesa). *Review of Scientific Instruments*, 85(2):02B122, 2014.

[92] Linac4 project, https://project-linac4.web.cern.ch/project-linac4.

[93] G. Bellodi. User specifications for Linac4 test bench diagnostics. Technical Report L4-B-EP-0002, CERN, Geneva, Switzerland, 2009.

[94] F Roncarolo, G Bellodi, E Bravin, et al. Overview of the cern Linac4 beam instrumentation. In *Proceedings of LINAC2010*, pages 770 —- 772, Tsukuba, Japan, 2010.

[95] F. Zocca, E. Bravin, M. Duraffourg, et al. Profile and emittance measurements at the CERN Linac4 3 MeV test stand. In *Proceedings of IBIC2013*, pages 826–829, Oxford, UK, 2013.

[96] F. Zocca, J.C. Allica Santamaria, M Duraffourg, et al. Beam diagnostics measurements at 3 MeV of the Linac4 $H^-$ beam at cern. In *Proceedings of IPAC2014*, pages 3694–3696, Dresden, Germany, 2014.

[97] Manlight S.A.S, Lannion, France. *Pulsed Yb dopped Fiber Laser User's Manual*, 2 edition, 2010.

[98] T. Hofmann, E. Bravin, U. Raich, F. Roncarolo, and B. Cheymol. Laser based stripping system for measurement of the transverse emittance of $H^-$ beams at the cern Linac4. In *Proceedings of IPAC2013*, pages 652–654, Shanghai, China, 2013.

[99] Wim de Boer, Johannes Bol, Alex Furgeri, et al. Radiation hardness of diamond and silicon sensors compared. *physica status solidi (a)*, 204(9):3004–3010, 2007.

[100] Newport corporation http://www.newport.com.

[101] Sill optics gmbh & co. kg http://www.silloptics.de.

[102] Laser 2000 (uk) ltd http://www.laser2000.co.uk.

[103] Lasermet ltd http://www.lasermet.com.

[104] Gentec electro-optics https://www.gentec-eo.com.

[105] Cividec instrumentation gmbh http://www.cividec.at.

[106] J. P. Carneiro, B. Mustapha, and P. Ostroumov. Numerical simulations of stripping effects in high-intensity hydrogen ion linacs. *Physical Review Special Topics - Accelerators and Beams*, 12(4):040102, 2009.

[107] A. J. Jason, D. W. Hudgings, and O. B. Dyck. Neutralization of $H^-$ beams by magnetic stripping. *IEEE Transactions on Nuclear Science*, NS-28(3):2704–2706, 1981.

[108] George H. Gillespie. Double closure calculation of the electron-loss cross section for $H^-$ in high-energy collisions with h and he. *Phys. Rev. A*, 15:563–573, 1977.

[109] J. Heinemeier, P. Hvelplund, and F. R. Simpson. Collisional detachment cross sections for $H^-$ and $He^-$ at high energies. *Journal of Physics B: Atomic and Molecular Physics*, 9(15):2669, 1976.

[110] T. Hofmann, E. Bravin, U. Raich, et al. Status and future plans of the cern Linac4 emittance meter based on laser electron-detachment and a diamond strip-detector. In *Proceedings of IBIC2014*, Monterey, USA, 2014.

[111] S.M. Gibson, G. Boorman, A. Bosco, et al. A fibre coupled, low power laselaser emittance scanner at CERN Linac4. In *Proceedings of IPAC2014*, pages 3725–3728, Dresden, Germany, 2014.

[112] S. Damelin and W. Miller. *The Mathematics of Signal Processing*. Cambridge University Press, 2011.

[113] N.L. Johnson. *Continuous Univariate Distributions*, volume 1 of *Wiley Series in Probability and Statistics*. Wiley-Blackwell, 1994.

[114] E Bravin, T Hofmann, Uli Raich, et al. Transverse profile and emittance measurements with a laser stripping system during the CERN Linac4 commissioning at 3 and 12 MeV. In *Proceedings of LINAC2014*, Geneva, Switzerland, 2014.

[115] L.M. Bobb, E. Bravin, T. Lefèvre, et al. Diffraction radiation test at CesrTA for non-intercepting micron-scale beam size measurement. In *Proceedings of IBIC2013*, pages 619–622, Oxford, UK, 2013.

[116] R. Ainsworth, A. Aryshev, T. Aumeyr, et al. Development of a combined OTR/ODR emittance station for future linear colliders such as CLIC or ILC at ATF2. Proposal presented at 17th ATF2 Project Meeting, KEK, Japan, 2014.

[117] Duarte Pinto S, Jones R, Ropelewski L, Spanggaard J, and Tranquille G. Gem-based beam profile monitors for the antiproton decelerator. *Journal of Instrumentation*, 7(03):C03001, 2012.

[118] The front end test stand twiki page, http://www.fets.isis.rl.ac.uk/images.

[119] D.J.S. Findlay. The RAL Front End Test Stand. In *Proceedings of NuFact04*, Osaka University, Japan, 2004.

[120] A. Letchford, M. Clarke-Gayther, D. Faircloth, et al. Status of the RAL Front End Test Stand. In *Proceedings of IPAC2013*, Shanghai, China, 2013.

[121] D. C. Faircloth, S. Lawrie, A. P. Letchford, et al. The Front End Test Stand high performance $H^-$ ion source at Rutherford Appleton Laboratorya. *Review of Scientific Instruments*, 81:02A721, 2010.

[122] J. Back, J. Pozimski, P. Savage, et al. Commissioning of the low energy beam transport of the Front End Test Stand. In *Proceedings of IPAC'10*, Kyoto, Japan, 2010.

[123] P. Savage, M. Aslaninejad, J. Pozimski andA. Garbayo, et al. Production of the FETS RFQ. In *Proceedings of IPAC2013*, Shanghai, China, 2013.

[124] J. M. Aslaninejad, J. Pozimski, and P. Savage. MEBT design for the Front End Test Stand project at RAL. In *Proceedings of IPAC2013*, Shanghai, China, 2013.

[125] J. Pozimski and S. Gibson. Particle tracking for the FETS laser wire emittance scanner. In *Proceedings of IBIC2013*, Oxford, UK, 2013.

[126] C. Gabor, A. Jakob, O. Meusel, et al. Design of nondestructive emittance measurement device for $H^-$ beams. *Review of Scientific Instruments*, 73(2):998–1000, 2002.

[127] K.O. Kruchinin, A. Bosco, S.M. Gibson, et al. Simulation results of the FETS laser-wire emittance scanner. In *Proceedings of IPAC2014*, pages 3729–3731, Dresden, Germany, 2014.

[128] General particle tracer: http://www.pulsar.nl/gpt.